Synthesis of anisotropic plate-like nanostructures using gibbsite nanoplates as the template

D i s s e r t a t i o n

zur Erlangung des akademischen Grades

d o c t o r r e r u m n a t u r a l i u m

(Dr. rer. nat.)

im Fach Chemie

eingereicht an der

Mathematisch-Naturwissenschaftlichen Fakultät

der Humboldt-Universität zu Berlin

von

M. Sc. Jie Cao

Präsident der Humboldt-Universität zu Berlin

Prof. Dr.-Ing. Dr. Sabine Kunst

Dekan: der Mathematisch-Naturwissenschftlichen Fakultät

Prof. Dr. Elmar Kulke

Gutachter: 1. Prof. Dr. Matthias Ballauff

2. Prof. Dr. Nicola Pinna

Tag der mündlichen Prüfung: 31.03.2017

Energy and persistence conquer all things.

Benjamin Franklin

To My Family & Friends

Abstract

In the present thesis, efficient and simple modification approaches have been developed to coat gibbsite platelets with a controllable thickness of functional polymer shell, which preserves the plate-like morphology after the polymer coating.

In the first part, a facile approach has been presented for the synthesis of anisotropic plate-like gibbsite-polydopamine (G-PDA) particles. Au NPs with tunable size have been formed on the G-PDA particle surface, which show efficient catalytic activity for the reduction of 4-nitrophenol and Rodamine B (RhB) in the presence of borohydride. Such nanocatalysts can be easily deposited on silicon substrate by spin coating due to the large contact area of the plate-like G-PDA particles and the strong adhesive behavior of the PDA layer. The substrate-deposited nanocatalyst can be easily recycled, which shows excellent reusability.

Secondly, anisotropic hybrid core-shell microgels with well-defined structures have been synthesized using gibbsite nanoplate as core and crosslinked thermosensitive poly(N-isopropylacrylamide) as shell. The analysis by depolarized dynamic light scattering shows that the hybrid microgels have an anisotropic shape in the collapsed state, caused by the anisotropy of the plate-like core.

In the third part, highly dispersible mesoporous nitrogen-doped hollow carbon nanoplates have been synthesized as a new carbon nanostructure via silica nanocasting technique using dopamine as carbon precursor and hexagonal-shaped gibbsite as template. Such hollow carbon nanoplates show excellent colloidal stability in aqueous media and can be directly applied as electrode materials in supercapacitors, which offer high capacitance and excellent electrochemical stability when using poly(ionic liquid) nanoparticles as binder.

Keyword: gibbsite platelets, polydopamine, catalysts, hybrid microgels, hollow carbon nanoplates, supercapacitors.

Zusammenfassung

In der vorgelegten Arbeit werden sowohl effiziente als auch einfache Modifikationsansätze zur funktionalen Polymerumhüllung von Gibbsit-Plättchen präsentiert. Die plättchen-förmige Morphologie bleibt dabei nach der Polymerumhüllung erhalten.

Im ersten Teil wird ein einfacher Ansatz zur Synthese von anisotropen, plättchen-förmigen Gibbsit-Polydopamin (G-PDA) Partikeln vorgestellt. Au NPs von kontrollierbarer Größe wurden auf der G-PDA Partikeloberfläche gebildet. Diese zeigten katalytische Aktivität zur Reduktion von 4-Nitrophenol und Rhodamin B (RhB) mittels Borhydrid. Die Partikel können durch ihre große, plättchen-förmige Kontaktfläche und der stark adhäsiven Eigenschaften der PDA Hülle einfach mittels Spin-Coating auf Siliziumsubstrate aufgebracht werden. Der so präparierte Nanokatalysator kann nun einfach wiederaufbereitet werden und zeigt hervorragende Wiederverwendbarkeit.

Im zweiten Teil wurden anisotrope, hybride Kern-Schale Mikrogele mit wohldefinierter Struktur synthetisiert. Dabei bilden die Gibbsit Nanoplättchen den Kern und vernetztes, thermosensitives Poly(N-isopropylacylamid) die Hülle. Depolarisierte dynamische Lichtstreuung zeigte, dass die hybriden Mikrogele im kollabierten Zustand durch die plättchen-förmigen Kerne eine anisotrope Form annehmen.

Der dritte Teil der Arbeit befasst sich mit der Herstellung von hochdispergierbaren, mesoporösen und stickstoffhaltighohle Kohlenstoff-Nanoplättchen. Diese neuartige Kohlenstoff-Nanostruktur wurde mittels sogenannter Silika-Nanocasting Technik unter Veswendung von hexagonalen Gibbsit-Templat und Dopamin als Kohlenstoffquelle synthetisiert. Solche hohlen Kohlenstoff-Nanostrukturen weisen exzellente, kolloidale Stabilität in wässrigen Medien vor und können direkt als Elektrodenmaterial für Superkondensatoren verwendet werden. Außerdem können sie in polyionischen Flüssigkeiten hohe Kapazitäten erzielen, wobei gleichzeitig eine hervorragende elektrochemische Stabilität gewährleistet wird.

Schlagwörter: Gibbsit-Plättchen, Polydopamin, Katalysator, hybrides Mikrogel, hohle Kohlenstoff Nanoplättchen, Superkondensator.

Table of Content

Abstract ..... **I**

Zusammenfassung ..... **III**

1. Introduction **1**

1.1 Anisotropic nanoparticles 1

1.2 Surface modification of plate-like particles 3

1.2.1 Polydopamine coating 5

1.2.2 PNIPAm coating 8

2. Objectives of this thesis **11**

3. Theory **13**

3.1 Gibbsite platelets: structure and chemistry 13

3.2 Surface modification of gibbsite platelet 15

3.2.1 Silica coating 16

3.2.2 PNIPAm 16

3.2.3 Polydopamine 17

3.3 Catalytic reduction of 4-nitrophenol by Au nanoparticles 20

3.4 Energy storage in electrical double layer capacitors (EDLC) 23

3.4.1 Energy storage mechanism 23

3.4.2 Electrode materials 26

3.4.3 Aqueous electrolyte 27

4. In-situ generation of catalytically active Au nanoparticles onto gibbsite-polydopamine (G-PDA) core-shell nanoplates **29**

4.1 G-PDA core-shell nanoplates 30

4.1.1 Gibbsite platelets 30

4.1.2 PDA coating 31

4.2 In-situ synthesis of G-PDA-Au nanocomposites 35

4.2.1 Influence of the $HAuCl_4$ concentration on the morphology of Au nanoparticles 36

4.2.2 Influence of the reaction time on the morphology of Au nanoparticles 37

4.3 Catalytic application of G-PDA-Au nanocomposites 39

4.3.1 Reduction of 4-nitrophenol 39

4.3.2 Catalytic activity evaluation for the reduction of Rodamine B 44

4.3.3 Fabrication of the substrate-deposited nanocatalysts and recyclability test 46

5. Thermo-responsive core-shell hybrid microgels based on anisotropic plate-like nanoparticles 49
5.1 Synthesis and functionalization of silica coated gibbsite platelets 50
5.2 Synthesis and characterization of GS-MPS-PNIPAm microgels 55
6. Synthesis of dispersible, monodisperse and mesoporous hollow carbon nanoplates with uniform hexagonal morphologies for supercapacitors 65
6.1 Synthesis of hollow silica nanoplates with a polydopamine shell 66
6.1.1 Synthesis of silica coated gibbsite 67
6.1.2 Etching gibbsite cores 69
6.1.3 Deposition of PDA 70
6.2 Synthesis and characterization of hollow carbon nanoplates 71
6.3 Electrochemical properties of the hollow carbon nanoplates 79
6.3.1 Electrochemical properties of hollow carbon nanoplates by using PIL as binder 79
6.3.2 Electrochemical properties of hollow carbon nanoplates by using PVDF as binder 82
7. Summary and outlook 87
8. Experimental 89
8.1 Chemicals 89
8.2 Synthesis 89
8.2.1 G-PDA-Au nanocomposites 89
8.2.2 Synthesis of GS-MPS-PNIPAm core-shell particles 92
8.2.3 Hollow Carbon nanoplates 93
8.3 Characterization 95
8.3.1 Imaging techniques 95
8.3.2 Spectroscopic characterizations 97
8.3.3 Light scattering and Zeta-potential measurements 98
8.3.4 X-ray powder diffraction (XRD) 100
8.3.5 Thermogravimetric analysis (TGA) 100
8.3.6 Nitrogen sorption 100
8.3.7 Elemental analysis 101
Bibliography 103
List of Figures 125
List of Tables 135

List of Publications **137**
Presentations at Conferences and Meetings **139**
Abbreviations **141**
Acknowledgement **147**
Selbstständigkeitserklärung **149**

1. Introduction

1.1 Anisotropic nanoparticles

Nanomaterials are defined as materials with at least one external dimension in the size range from approximately 1-100 nanometers. One of the first scientific reports on nanomaterials is the colloidal gold nanoparticles synthesized by Faraday.[1] Since the initial discovery of (nano) size-related properties, the correlation between particle size and the physical/chemical properties has been systematically revealed for over a century.[2] Two principal factors cause the properties of nanomaterials to be special: increased relative surface area and quantum effects.[3] These factors can alter or improve properties of materials such as reactivity, strength/elasticity, thermal conductivity, absorbency, and electrical characteristics.[4–6] Because of these special properties, nanomaterials have been applied in many fields such as electronics, photochemistry, biomedicine and chemistry.[7–9]

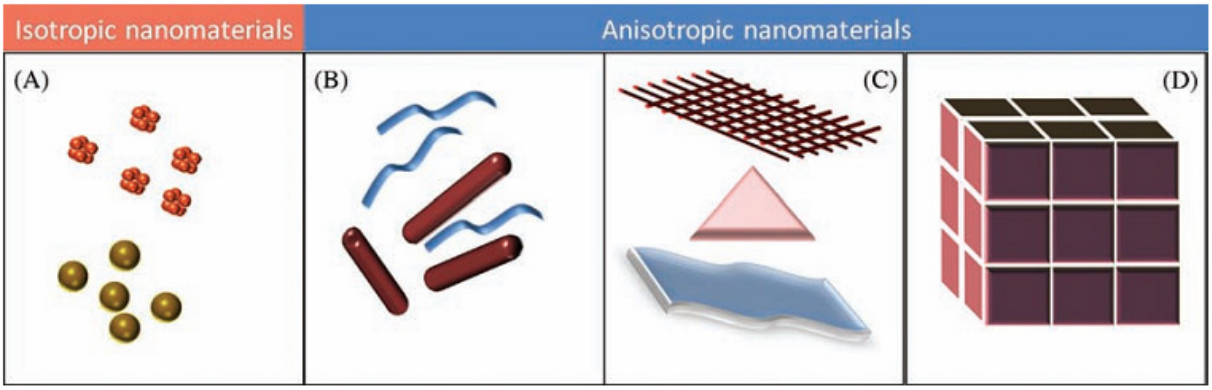

Figure 1.1.1 Various kinds of nanomaterials. (A) 0D spheres and clusters. (B) 1D nanofibers, wires, and rods. (C) 2D films, plates, and networks. (D) 3D nanomaterials. Reprinted with permission from ref.[10] Copyright 2011 *Nano Reviews*.

New research directions have been followed by finding and understanding new effects that are strongly affected by other parameters except the "size effect". Among these parameters, shape (or the degree of anisotropy) has been considered as a critical factor for engineering the properties of nanomaterials. Thus, numerous researches have been devoted to control the shape of nanomaterials.[11,12] In most cases it has a much more profound effect than that of size on materials properties. Over the past decades, there has been great progress in shape-dependent anisotropic nanomaterials.[13–15] A pictorial representation of anisotropic nanomaterials, which are classified as 1D, 2D, 3D nanostructures according to Siegel, is

shown in Figure 1.1.1. Their size and shape dependent physical and chemical properties make them ideal candidates for devising new applications in biosensor, catalysis, photothermal therapy and data storage.[10]

Among these anisotropic nanomaterials, 2D plate-like nanostructures have attracted increasing interest due to their shape-dependent properties such as large surface areas, high aspect ratio, and finite lateral sizes.[16,17] Colloidal platelets are abundant in nature (*e.g.*, clay minerals or red blood cells) and can be readily synthesized in the laboratory in the form of mixed metal hydroxides. Gibbsite (γ-$Al(OH)_3$), the most common oxide of aluminum mineral present in soils, is of particular interest because of its multiply applicability as flame retardant, adsorbent, paper additive, and polishing agent in toothpaste. It has been also marked as model system for the study of liquid crystal dynamics in the case of colloidal gibbsite nanoplates.[18–22] Gibbsite was first discovered in 1820 by Dewey, and subsequently named as Gibbsite in 1822 by Torrey in honor of George Gibbs, a noted mineralogist. In 1933, the structure of natural gibbsite was first studied and then later reinvestigated in 1973.[23] It adopts a layered structure as shown in Figure 1.1.2a. Each of the $Al(OH)_3$ layers consists of nearly close packed OH^- ions, in which the Al^{3+} ions occupy two-thirds of the octahedral holes between alternate layers. Consequently, the structure of gibbsites has pseudohexagonal symmetry, but small distortions of the OH^- ions result in a small shift of the adjacent layers and a lowering of the crystal symmetry to monoclinic.[24]

Industrially, gibbsite is extracted and purified via the Bayer process invented in 1887, a large-scale technique for producing aluminum and alumina.[25] However, the resulting gibbsite particles adopt irregular shape with dimensions varying from a few micrometers to hundreds of micrometers, which restrict their applicability.[26,27] Several methods have been reported to synthesize nano-sized gibbsite particles in the laboratory.[28–33] Only few can achieve regularly shaped pure gibbsite nanoparticle.[31–33] In 1998, fairly monodisperse gibbsite platelets (Figure 1.1.2b) with an average diameter of 160 nm and an average thickness of 13 nm were synthesized from a solution of aluminium alkoxide precursors by Philipse et al.[31] The size of the particles can be varied slightly by varying the reaction conditions. Subsequently, Wijnhoven from the same group prepared gibbsite platelets with diameter of 570 nm and a thickness of 47 nm by using nanosized hexagonal gibbsite as seeds, which are grown from a mixture of dissolved alumina alkoxides at 85 ºC.[32]

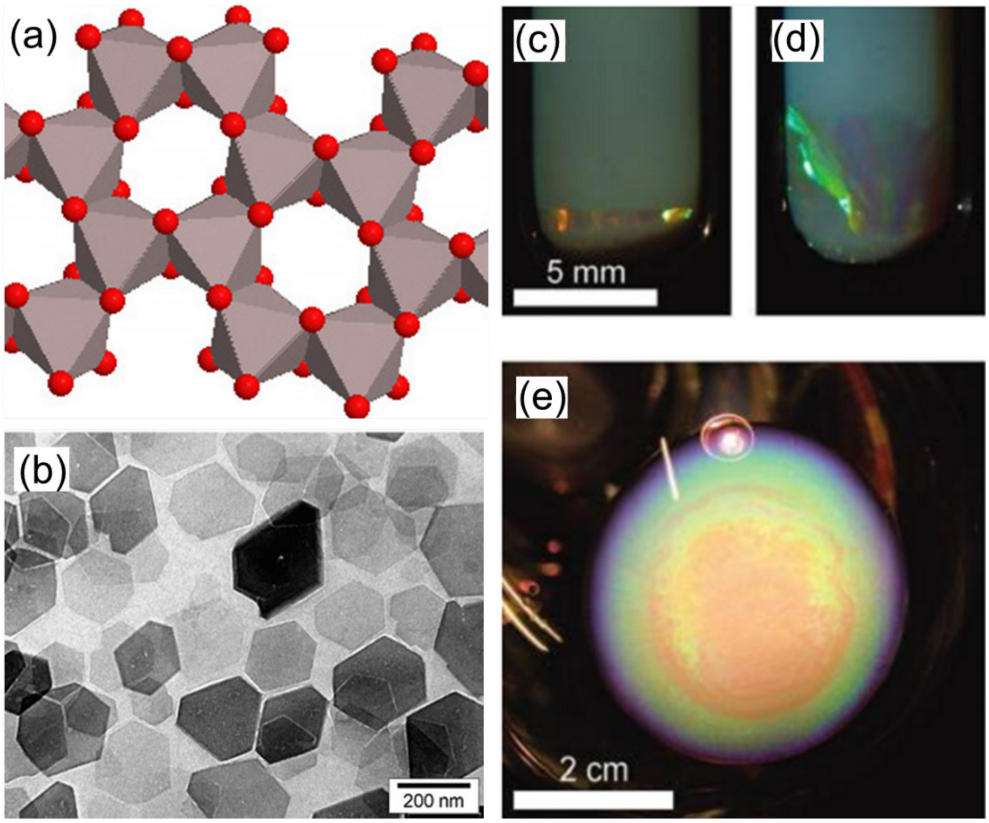

Figure 1.1.2 (a) Structure of gibbsite (γ-$Al(OH)_3$). (b) TEM micrograph of gibbsite particles. (c, d) Iridescent columnar phase grown in a gravitational field. Sample that has been standing for 2 and 4 years, respectively. (e) Iridescent columnar phase grown at 900 g using a centrifuge. Reprinted with permission from ref.[24,34] Copyright 1997 and 2007 *American Chemical Society*.

Since then, gibbsite particles prepared by the aforementioned method have been used as an experimental counterpart for the disks or cut-spheres in theory and simulation, as well as an experimental system for suspensions of clays.[31,35] Its formation of liquid crystal has been also investigated extensively by Lekkerkerker *et al.*[36–38] Colloidal gibbsite platelets can easily form an opal-like columnar crystal with striking iridescent Bragg reflections either under normal gravity (Figure 1.1.2c and d) or by modest centrifugation (Figure 1.1.2e).[34] To overcome gelation and make gibbsite particles more stable, surface modification of gibbsite platelets by surfactants (*e.g.*, alumina chlorohydrate or polyisobutene) is normally required before dynamics and phase behaviors investigation.

1.2 Surface modification of plate-like particles

Surface modification allows control of the surface properties and confers new functionalities to them, a feature that is especially important in some critical fields.[39,40] Polymer coated

plate-like nanomaterials dispersed in aqueous solution open the opportunity to develop new hybrid particles with special mechanical or rheological behavior.[41,42] The first polymer coated plate-like nanomaterial was reported in the literature as early as 1961, when Blumstein demonstrated polymerization of vinyl monomers intercalated into montmorillonite.[43] Fabrication of polymer-layered silicate nanocomposites attracted great interests since Toyota's work on the exfoliation of clay in nylon-6 in the 1980's, which are also the first commercialized polymer-clay nanocomposites.[44] It was demonstrated that a significant improvement in the thermal, rheological and mechanical properties of the polymer has been achieved by reinforcing polymers with clay on the nanometer scale.

Following the initial results, extensive research in this field has been carried out over the past decade.[40,44] One often-employed strategy to modify inorganic clay is the exchange of stabilizing alkali by organic cations such as alkylammonium, making the clay organophilic and compatible with polymers.[45,46] Melt intercalation and in situ polymerizations in the presence of organically modified clays have been used to produce polymer-clay nanocomposites with improved mechanical and thermal properties of the polymer.[47,48] Emulsion polymerization in the presence of clays was employed to prepare polymer/clay hybrid particles, but only armored particles were obtained.[49–51] Surface modification with polymer shell appears to be very challenging due to the disk shape morphology, large aspect ratio, and high surface energy of the plate-like nanomaterial.[52]

Often armored, dumbbell-like or spherical latex particles with one or a few clay platelets per particle are obtained by the reported polymerization approaches.[49,50,52,53] Only few examples of true polymer encapsulation have been achieved, which, however, requires very complicated synthetic procedures. For instance, Ali *et al.* synthesized poly(methyl methacrylate) (PMMA) encapsulated gibbsite nanoparticles by radical addition fragmentation chain transfer (RAFT)-based starved feed emulsion polymerization.[54] Voorn *et al.* encapsulated platelets by controlled heterocoagulation of gibbsite and poly(n-butyl methacrylate) (PBMA) latex particles, followed by thermal annealing of the PBMA.[55] Nevertheless, the thickness of the polymer layer cannot be well controlled in these reports, which makes the encapsulated particles lose the original plate-like morphology. Thus, it remains a challenge to search for an efficient and simple approach to coat the gibbsite platelets with functional polymer with controllable thickness, and to preserve the plate-like morphology after the polymer coating. In addition, incorporation of stimuli-responsive

properties (pH, temperature, or ions) into the plate-like microgel particles would be another interesting point.

1.2.1 Polydopamine coating

Dopamine, a catecholic compound with a primary amine functional group (Figure 1.2.1a), is better known as the neurotransmitter whose deficiency leads to Parkinson's disease and is the most widely distributed catecholic compound.[56] It was first discovered by a Swedish pharmacologist, Arvid Carlsson in 1952. Five years later, Carlsson proved that dopamine was in fact a bonafide neurotransmitter, not just a precursor. Since then, dopamine created a whole new area of scientific study. In 2007, Messersmith *et al.* firstly developed dopamine self-polymerization in alkaline solution at room temperature as a novel and important protocol for multifunctional coatings of polydopamine (PDA) films with controllable thickness onto a wide range of inorganic and organic materials (Figure 1.2.1b and c), including noble metals (Au and Ag), metal oxides (TiO_2 and SiO_2), semiconductors (GaAs), glass, ceramics and synthetic polymers.[57] Unlike other traditional polymerization approaches, such as monolayer self-assembly, layer-by-layer assembly, and Langmuir−Blodgett deposition, surface modification with PDA requires only a single step. Thus, it provides possibilities to coat nanomaterials with controlled thickness.

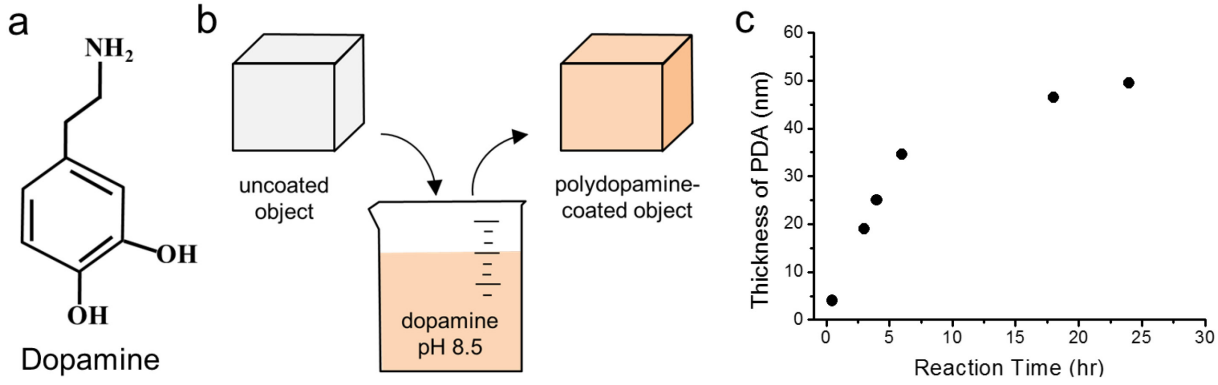

Figure 1.2.1 (a) Chemical structure of the dopamine molecule. (b) A schematic illustration of thin film deposition of PDA by dip-coating an object in an alkaline dopamine solution. (c) Thickness evolution of PDA coating on Si as measured by AFM of patterned surfaces. Reprinted with permission from ref.[57] Copyright 2007 *Science*.

Over the past few years, numerous nanomaterials, including Au/Ag,[58] SiO_2,[59] polystyrene,[60] Fe_3O_4,[61] $Ni(OH)_2$ nanowires,[62] carbon nanotubes,[63] ZnO nanorods,[64] graphene oxide,[65] montmorillonite,[66] and $ZnSnO_3$ nanocubes[67] have been successfully coated by PDA, and

subsequently applied in a broad range of biotechnology, electrochemical detection, membrane, catalysis, and energy storage.[68] However, to the best of our knowledge, encapsulation of 2D gibbsite nanoplates with controllable thickness of PDA shell has not been achieved so far. Moreover, the properties of the 2D anisotropic hybrid nanomaterials need to be further explored.

Recently, a number of advanced (nano) hybrids have been fabricated by taking advantage of combinations of the properties offered by PDA. The catechol groups in PDA are able to reduce noble metal ions, including Ag^{+}, Au^{3+}, and Pt^{3+}, to the corresponding metals as they are oxidized into quinone groups upon the release of electrons and protons.[68] Studies on one-step generation of Au or Ag nanocatalysts using PDA as dual roles of reductant and stabilizer have been reported in some literatures.[69,70] For instance, Cai *et al.* have obtained Fe_3O_4 nanoparticles coated with gold nanoparticles in a two steps procedure.[71] Fe_3O_4 nanoparticles were first coated by PDA by immersion in a buffered dopamine solution, followed by dipping into $HAuCl_4$ aqueous solution. Gold nanoparticles were obtained by reduction of Au^{3+} by catechols of PDA without the need of any other reducing reagent. The as-prepared nanocatalysts show good activity in the reduction of o-nitroaniline. Liu *et al.* deposited Au nanoparticles on the surface of PDA-functionalized graphene for highly efficient catalysis of nitrophenol. Nevertheless, there is a systematic lack of effective investigations on the influence of PDA thickness or Au size/amount on the catalytic performace.

Another application for PDA coatings is their ability to obtain carbonaceous materials by simple carbonization of PDA at high temperatures in an inert environment. High electrical conductivity is one of the most significant properties of PDA derived carbon, which may be attributed to the altered molecular charge transfer behavior induced by the n-type doping by nitrogen and effective π–π stacking.[72] In 2011, Dai *et al.* successfully synthesized PDA derived hollow carbon spheres (Figure 1.2.2a) for the first time by pyrolysis of solution oxidation-derived PDA at 800 °C in N_2.[59] The obtained carbon is doped with about 7.28 wt% nitrogen, and the carbon yield is nearly 60 wt%. Subsequently, Li *et al.* synthesized ultrathin hollow mesoporous carbon nanospheres (HMCNs as shown in Figure 1.2.2b) by using PDA as carbon precursor and SiO_2 spheres as template.[73] The HMCNs demonstrate impressive capacitive properties when applied as supercapacitor electrodes. Besides carbon nanopheres, PDA derived core-shell carbon nanowires[62] (Figure 1.2.2c) and hollow carbon nanotubes[64] (Figure 1.2.2d) have been also reported. They exhibited enhanced performances when applied

as electrode materials in supercapacitors, owing to its outstanding physicochemical properties such as hollow interiors, rich abundance and high electrical conductivity.

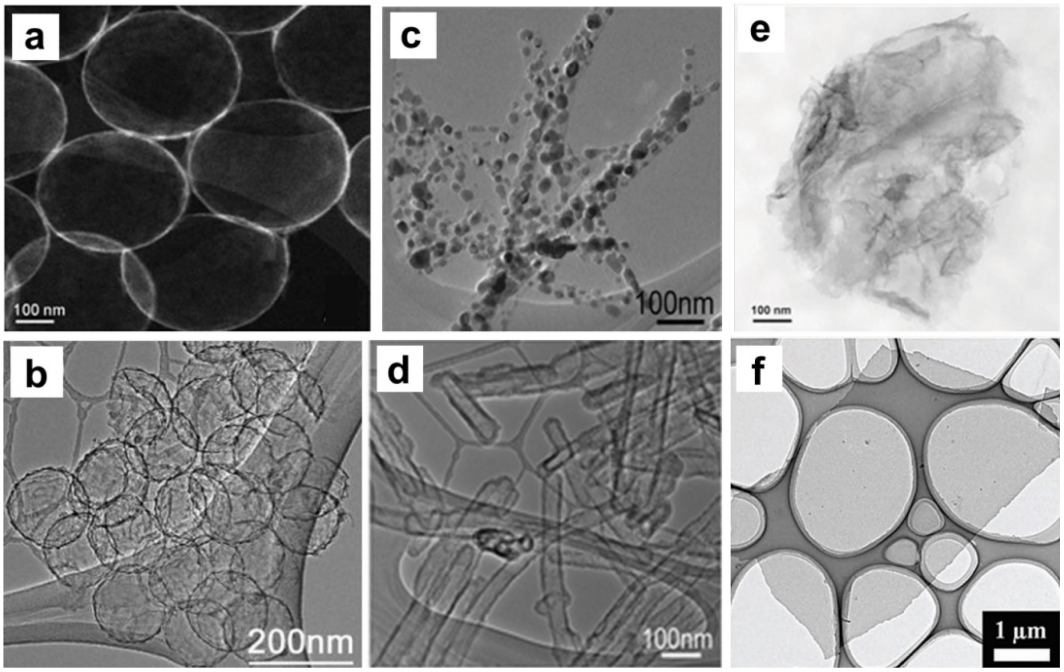

Figure 1.2.2 (a and b) TEM images of PDA derived hollow carbon nanopheres. Reprinted with permission from ref.[59,73] Copyright 2011 *WILEY-VCH* and Copyright 2011 *American Chemical Society.* TEM images of PDA derived (c) core-shell carbon nanowires and (d) hollow carbon nanotubes, Reprinted with permission from ref.[62,64] Copyright 2011 *Royal Society of Chemistry*. TEM images of PDA derived (e) carbon nanosheets and (f) carbon nanoplates. Reprinted with permission from ref.[74,75] Copyright 2013 and 2015 *WILEY-VCH*.

Compared with spherical or tube-like morphology of hollow carbon materials, two dimensional (2D) carbon materials with high aspect ratios, finite lateral sizes and porous structures have attracted increasing interest, making them desirable for potential applications in energy storage.[76,77] Carbon nanoplates are exotic carbon 2D nanostructures that have been studied in only limited examples due to their restricted accessability.[74,75] So far, only few examples of fabricating 2D plate-like hollow carbon materials have been reported.[74,75] For instance, 2D porous carbon nanosheets[74] (Figure 1.2.2e) and microporous carbon nanoplates[75] (Figure 1.2.2f) have recently been synthesized and implied in supercapacitor, which could shorten the ion transport distance in their nanoscaled dimension. In comparison, to our best knowledge hollow carbon nanoplates are unknown carbon nanostructures to be explored. Therefore, the exploration of 2D hollow and mesostructured carbon nanomaterials with regular morphologies would provide great opportunities to find attractive properties in energy storage devices.

1.2.2 PNIPAm coating

Thermoresponsive polymers with lower critical solution temperature (LCST) have been investigated for various biomedical applications.[78,79] One of such polymer with considerable focus is poly (N-isopropylacrylamide) (PNIPAm), which has a lower critical solution temperature around 32 °C.[80–83] Below this temperature, the solution is homogeneous, and the polymer chains are soluble in water due to the formation of hydrogen bonds between the water molecules and the amide side chains. Above this temperature, the polymer chains become hydrophobic, resulting in the shrinkage of polymer by expelling water from the polymer network. Such thermo-responsive polymers have been firstly studied by Heskin and Guillet in 1968.[84] In 1986, Pleton and Chibante firstly synthesized PNIPAm microgels.[85] Later, thermo-responsive core-shell hybrid particles made of PNIPAm shell and organic/inorganic cores have become the subject of intense research. It has been demonstrated that a PNIPAm shell can be affixed to colloidal gold, silica or polystyrene (PS) particles. Spherical core-shell PNIPAm particles are often obtained by different polymerization approaches.[86,87] The corresponding results have been shown in Figure 1.2.3.

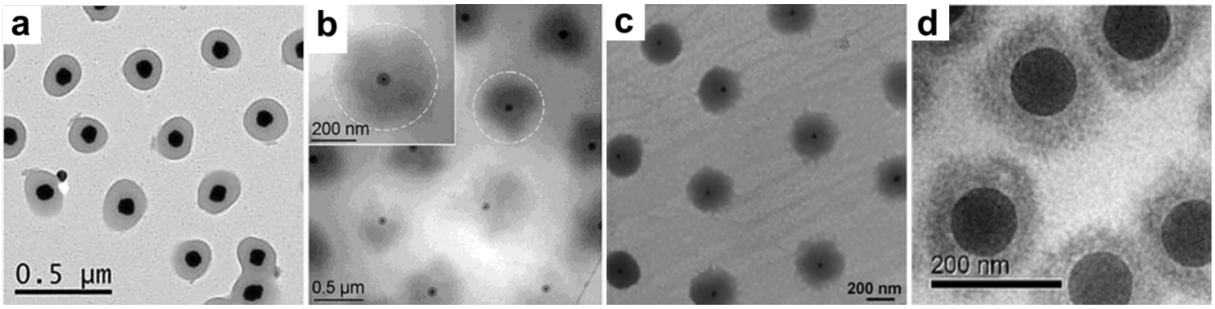

Figure 1.2.3 TEM images of spherical core-shell PNIPAm particles with (a) Au, (b) Au@SiO_2, (c) SiO_2, and (d) PS cores. Reprinted with permission from ref.[87,88] Copyright 2011 *ELSEVIER* and Copyright 2011 *WILEY-VCH*.

Recently, the researches on thermo-responsive core-shell particles have been further developed. Chu *et al.* have successfully modified dumbbell-shaped core with a thermosensitive PNIPAm shell as shown in Figure 1.2.4a, which can act as an excellent model system to study the phase behavior and the rheology of anisotropic colloids.[89] Dietsch *et al.* developed anisotropic thermo-responsive particles using ellipsoidal hematite[90] and maghemite[91] as cores (Figure 1.2.4b and c). Another approach for the preparation of thermosensitive ellipsoids is reported by Crassous and Dietsch by stretching spherical polymeric core-shell particles (Figure 1.2.4d).[92] The aspect ratio can be adjusted by controlling the stretching process. However, despite the increasing number of approaches for

synthesizing well-defined non-spherical colloids with different shapes in the last decade, attempts to synthesize thermo-responsive core-shell particles based on anisotropic nanoparticles are still sparse.

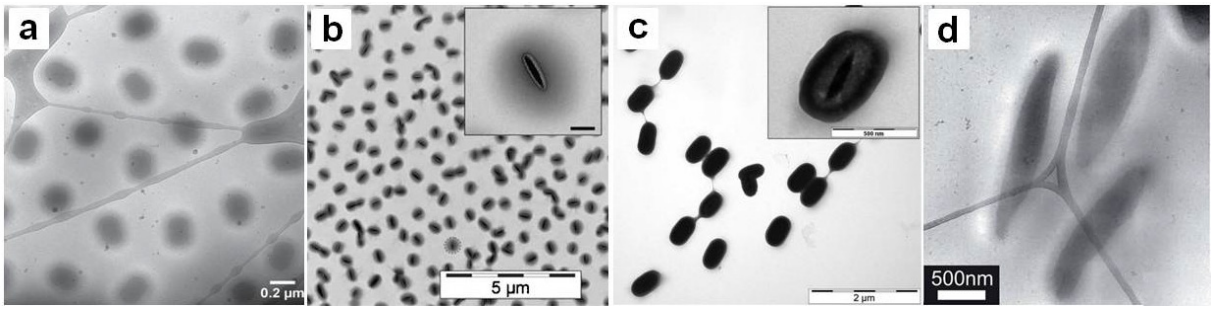

Figure 1.2.4 TEM images of (a) dumbbell-shaped core-shell PNIPAm particles. Reprinted with permission from ref.[89] Copyright 2011 *WILEY-VCH*. TEM images of ellipsoidal core-shell PNIPAm particles with (b) hematite, (c) maghemite, and (d) PS cores. Reprinted with permission from ref.[90–92] Copyright 2010 and 2012 *Royal society of Chemistry*.

2. Objectives of this thesis

The foremost objective of this thesis is to prepare monodisperse anisotropic polymer-gibbsite nanocomposite particles with controllable thickness, and to investigate their corresponding properties and applications in catalysis and energy storage devices. Due to the disk shape morphology, large aspect ratio, and high surface energy of the hexagonally shaped gibbsite nanoplates, it is difficult to modify their surface with controllable thickness of functional polymer shell. Thus, a simple and effective encapsulation approach is highly desirable. To achieve this objective two separate approaches have been performed: One approach via spontaneous oxidative polymerization of dopamine, and another approach using modified gibbsite platelets by a seeded emulsion polymerization.

The first part of this thesis is to modify the gibbsite nanoplates with controllable thickness of PDA shell by a facile method. The coated PDA shell not only enhances the colloidal stability of gibbsite nanoparticles, but also acts as stabilizer and reductant for in situ synthesis of Au nanocatalysts. The effects of the growth time and Au precursor concentration on the size/amount of the Au nanoparticles on the G-PDA nanoplates have been investigated systematically. The catalytic activities of G-PDA-Au nanocatalysts have been then determined using the reduction of 4-nitrophenol as the model reaction and compared with other reported catalytic systems. Moreover, combining the advantage of inorganic gibbsite nanoplates and polydopamine shell, recyclable G-PDA-Au nanocatalysts have been fabricated and tested in the reduction of Rodamine B.

The second part of this thesis is to prepare anisotropic organic/inorganic hybrid core-shell particles with well-defined structure. These thermosensitive core-shell particles consist of plate-like silica coated gibbsite nanoplate as core and crosslinked poly(N-isopropylacrylamide) (PNIPAm) network as shell. The PNIPAm shell enables the hybrid particle to alter its size and ratio with increasing temperature while the core morphology remains unchanged. The morphology of the hybrid particles has been investigated via cryo- and transmission electron microscopy, atomic force microscopy (AFM), dynamic light scattering (DLS), and depolarized dynamic light scattering (DDLS).

Finally, the study is extended to the preparation of highly dispersible mesoporous nitrogen-doped hollow carbon nanoplates (HCPs). Dopamine as carbon precursor is

self-polymerized on the surface of plate-like template to form a homogeneous polymer layer under constant ultrasonification, which not only favors the formation of the homogeneous polymer shell but also prevents the particles from aggregation. Each single plate-like core-shell particle is immobilized and insulated in silica gel via a silica nanocasting method. After confined pyrolysis and elimination of silica, discrete and dispersible hollow carbon nanoplates are obtained. A comprehensive characterization is performed to characterize the morphology, structure and elemental composition of these hollow carbon nanoplates via transmission electron microscopy (TEM), high-resolution TEM (HR-TEM), X-ray diffraction studies (XRD), Raman spectrum, energy-dispersive X-ray spectroscopy (EDX) measurements, hard X-ray photoelectron spectroscopy (HAXPES) measurements, thermo gravimetric analysis (TGA), and N_2 adsorption/desorption methods. Moreover, these hollow carbon nanoplates can show immediate applications in electrochemical double layer (ECDL) capacitors. The performance of hollow carbon nanoplates based ECDL capacitors has been investigated and compared by using poly (ion liquid) (PIL) and the commercial standard poly(vinylidene difluoride) (PVDF) as binder.

3. Theory

3.1 Gibbsite platelets: structure and chemistry

Gibbsite platelets consisting of $Al(OH)_3$ are formed by hydrolysis of $Al(OH_2)_6^{3+}$-groups at temperatures below 100−150 °C, while hydrolysis of the same solutions at higher temperatures yields boehmite (A1OOH).[93,94] The gibbsite surfaces are charged after being dispersed in water according to the following reactions:[95]

$$Al{-}OH_2^+ + OH^- \leftrightarrow Al{-}OH + H_2O \qquad (I)$$

$$Al{-}OH + H_2O \leftrightarrow Al{-}O^- + H_3O^+ \qquad (II)$$

The platelet will be positively charged when the pH value is lower than the isoelectric point (iep), following reaction (I). At pH > iep, a negative surface charge will be induced according to reaction (II).[95] The structure of the gibbsite crystals indicates that the acidity of the A1−OH groups at the edges is different from that on the faces. Therefore, the iep of the edges is different from that on the faces, leading to an inhomogeneous charge density on the gibbsite platelets.[96]

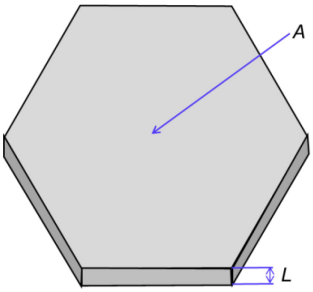

Figure 3.1.1 Schematic drawing of a hexagonally shaped gibbsite platelet. The platelet has a surface area *A* and thickness *L*. As a measure for the diameter *D* of the platelet, the diameter of an equivalent circle is calculated as $D = 2\sqrt{\boldsymbol{A/\pi}}$.[95]

It has been known for a long time that colloidal dispersions are ideal model systems.[97,98] A system consisting of hard spheres displays an isotropic fluid phase to crystal phase transition with increasing of the concentration.[99] If the particles have a different geometry, such as rod-like particles, a nematic phase and a smectic phase will form with increasing of the concentration.[100,101] These phases are called liquid crystals, as only some degrees of freedom are fixed. The liquid crystal phase behavior of plate-like particles such as colloidal gibbsite

platelets have been also studied extensively. Three main classes of liquid crystals including isotropic (I), nematic (N) and columnar (C) phases have been observed.[102] As illustrated in Figure 3.1.2, the isotropic fluid phase is characterized by a complete absence of positional and orientational order. In the nematic phase, the particles possess orientational order along some preferred direction. Their centres of masses are however still distributed homogeneously over the entire system volume, *i.e.* there is no long-range positional order. In the columnar state, the particles are ordered into a two-dimensional hexagonal lattice perpendicular to the preferred orientational direction. In the direction along the columns their arrangement is disordered and hence there are no long-range spatial correlations.

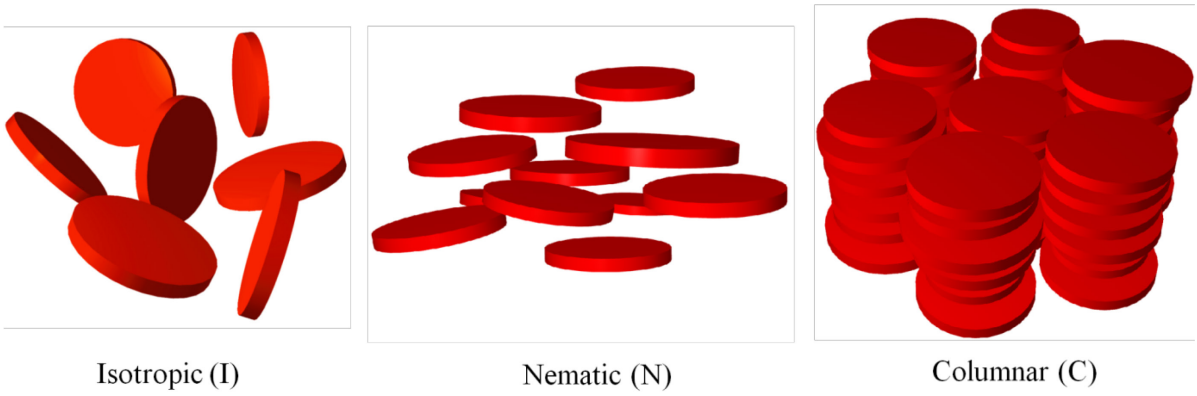

Figure 3.1.2 Schematic representations of various (liquid crystal) phases for plate-like particles. While each of these phases exhibits long-range orientational order, they differ by the positional correlations between the particles. In the nematic phase long-range positional order is absent. The columnar phase has a two-dimensional lattice of columns, which are constituted of liquid-like stacks of particles.

The phase behavior of the gibbsite platelet suspensions as a function of the plate volume fraction ϕ is presented[102] in Figure 3.1.3. I–N phase coexistence is observed just below $\phi = 0.2$, yielding an isotropic upper phase and a birefringent nematic bottom phase. By increasing the volume fraction, a nematic phase will form, in which the particles are more or less aligned, but can still translate freely in all directions. The gain in free-volume entropy by aligning the particles is higher than the loss in orientational entropy. If the plate volume fraction is increased to $\phi = 0.4$, the suspension enters a biphasic region where a nematic phase coexists with a columnar phase, which is suggested by unequivocal Bragg reflections when illuminated by white light. The fact that these reflections appear for wavelengths of visible light demonstrates that the crystalline order pertains to a periodicity on a length scale of the plate diameter (characteristic of columnar ordering).

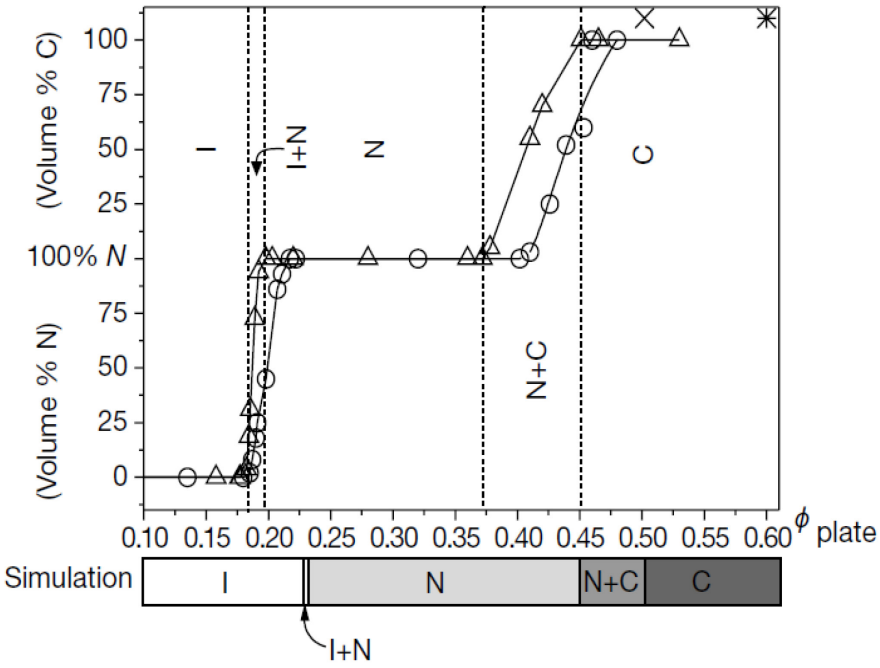

Figure 3.1.3 Phase diagram of the gibbsite suspensions. The relative volume of the nematic and columnar phase are depicted after phase separation as a function of the platelet volume fraction ϕ. Results apply to σ_D = 17% (triangles) and σ_D = 25% (circles), respectively. The dotted lines indicate the boundaries of the coexistence regions of the suspension with σ_D = 17%. Results from computer simulation for monodisperse hard disks, extrapolate to the current aspect ratio <*D*>/<*L*> of roughly 13, are included for comparison. Reprinted with permission from ref.[102] Copyright 2000 *Nature*.

The formation of opal-like columnar crystal with striking iridescent Brag reflections can also be accelerated by orders of magnitude using centrifugation without arresting the system in a disordered glassy phase.[34,103] The ease of crystallization is partially related to particle fractionation during centrifugation. Under high gravitational forces, one expects a compression of the sediment, resulting in a gradient in the periodicity of the Bragg reflections. The top layer of the sediment contains the smallest particles, and the middle as well as lower layers show an increasing average diameter.[34] Thus, the columnar periodicity increases on going down in the sediment, directly causing the iridescent color.

3.2 Surface modification of gibbsite platelet

To stabilize gibbsite platelets and preserve their anisotropic morphology, the platelets can be modified by a protective shell (*e.g.* metal oxides or a polymer network). The protective shell not only provides higher stability, but also allows for incorporation of active molecules and functionalization with new reactive groups, or environment responsive behavior.[55,104,105] Three important examples of possible shells will be discussed here: inorganic amorphous silica,

thermosensitive poly(N-isopropylacrylamide) (PNIPAm), and polydopamine (PDA).

3.2.1 Silica coating

Amorphous silica shells have become one of the most popular methods to stabilize and functionalize metal/metal oxide nanoparticles.[106,107] They are a class of materials widely applied in the field of colloid and material science, offering several advantages: 1) simple coating methodology, 2) cheapness, 3) colloidal stability in a wide range of different media and at high volume fractions, and 4) chemical inertness.[108] In 2003, Graf *et al.* for the first time developed a method to modify anisotropic plate-like gibbsite nanoparticles with a homogeneous silica shell.[109] They followed a modified Stöber process that produced monodisperse silica spheres.[110] The gibbsite platelets have been initially stabilized by the amphiphilic, nonionic polymer polyvinylpyrrolidone (PVP) as a coupling agent. After this functionalization the stabilized gibbsite platelets can be transferred to a solution of ammonia and tetraethyl orthosilicate (TEOS) in ethanol. Under Stöber process condition a smooth and homogeneous silica shell with variable thickness can be grown by hydrolyzation and condensation of TEOS. This process can be easily adapted to coat other metal nanoparticles such as gold/silver colloids, boehmite rods, and polystyrene latex with silica shell.[109]

Another merit for silica modification is that the silica shell can be easily functionalized by a number of different silane reagents such as 3-(trimethoxysilyl)propyl methacrylate (MPS). The surface supplies silanol bonds that can be functionalized via grafting with new silane molecules. It has been shown that thermosensitive PNIPAm network can be attached onto the surface of MPS functionalized silica particles via seeded emulsion polymerization.[86]

3.2.2 PNIPAm

Stimuli-responsive polymers attract a great deal of attention owing to their potential applications in the fields of water treatment, bioseperation, and chemical sensors.[111,112] One such polymer of considerable focus is PNIPAm, which is well known for its thermo-sensitive behavior in aqueous media.[113] PNIPAm chain has a flexible coil structure when the temperature is below its lower critical solution temperature (LCST) of around 32 ºC, whereas the chain undergoes a coil-to-globule transition at temperatures above its LCST. The simultaneous presence of hydrophilic amide groups and hydrophobic isopropyl groups in PNIPAm lead to the thermo-responsiveness. At low temperature, the polymer chains are

soluble due to the strong interaction between amide groups and water through hydrogen bonding. When the temperature increases to above LCST, the polymer chains become hydrophobic because the hydrogen bonds are broken, and phase separation occurs, which is accompanied by expelling of water from the polymer network. As a result of this change in the solubility, the crosslinked PNIPAm microgels undergo a temperature induced phase transition in water from highly swollen networks below the LCST, to shrunken state above the LCST.[114–116]

The modification of PNIPAm shells on the colloidal nanoparticles is done via radical seeded emulsion or precipitation polymerization, which can be thermal or photo-initiated.[117] The polymerization can be assisted by grafting coupling agent (*i.e.*, MPS) on the surface of the colloidal nanoparticles. This coupling agent supplies double bonds and generates a hydrophobic surface. Afterwards, it can react in the radical polymerization allowing for the chemical coupling between the PNIPAm network and the colloidal nanoparticles. The functionality and stabilization of these core-shell systems can be achieved at the same time by using simple approaches.

3.2.3 Polydopamine

Another thoroughly investigated polymer is polydopamine (PDA), which has drawn a lot of interest recently as a universal surface modification agent for various applications.[68] As demonstrated by Messersmith *et al.*,[57] diverse materials can be coated with PDA via the treatment of the surface with a tris(hydroxymethyl) aminomethane (Tris) buffered dopamine solution. The PDA coatings obtained from this approach are highly robust and typically thin (tens of nm thick).[60] Unlike other techniques, surface modification with PDA requires only a single step.[118]

3.2.3.1 Polymerization mechanisms of dopamine

Surface modification with a PDA layer can be achieved in a facile and simple process, but the polymerization mechanism and the resultant PDA structure are still not fully clarified to date, because of the complex redox process as well as the generation of a series of intermediates during the polymerization processes. Two models proposed by researchers shall be introduced.

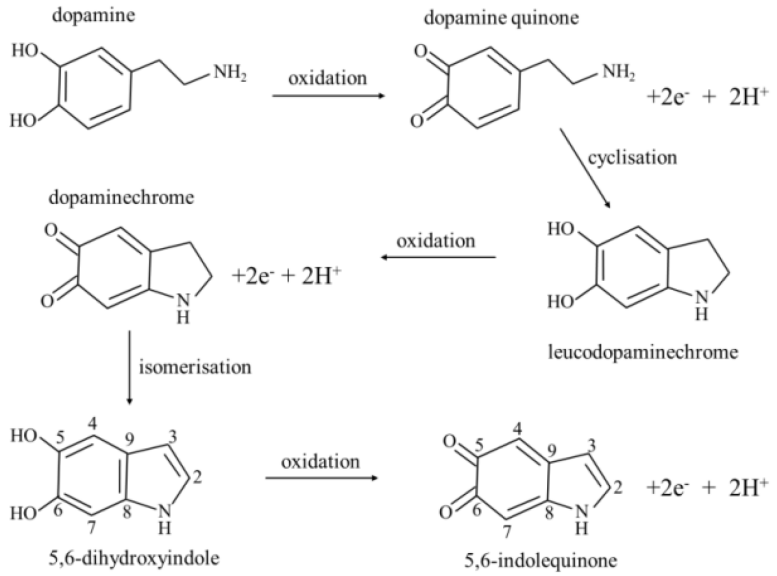

Figure 3.2.1 "Eumelanin" model of the formation mechanism of PDA. Reprinted with permission from ref.[119] Copyright 2011 *American Chemical Society*.

At the early stage of this research field, it was believed that the formation of polydopamine follows a process similar to biosynthetic pathways of melanin (eumelanin) in organism.[120–122] As shown in Figure 3.2.1, dopamine is first oxidized to dopamine-quinone under alkaline conditions. Secondly, leucodopaminechrome is formed by intramolecular cyclization via 1,4 Michael addition when the amine group is deprotonated.[123] Thereafter, leucodopaminechrome is easily oxidized to dopaminechrome, which further rearranges to form 5,6-dihydroxyindole (DHI), and the further oxidation produces 5,6-indolequinone.[124] The last two products are capable of undergoing branching reactions at positions 2, 3, 4, and 7, resulting in multiple isomers of dimers and higher oligomers, which undergo self-assembly through the reverse dismutation reaction between catechol and o-quinone to form PDA particles.[125] However, little solid experimental evidence has been found for this "eumelanin" model. Preliminary verification of this polymerization mechanism is obtained by FTIR analysis, which proves the intramolecular cyclization reaction occurrs in dopamine along with the formation of indole derivatives.[121,126]

In contrast to the "eumelanin" model described above, an alternative structural model for PDA has been recently proposed based on the ability of the monomers to bond in a non-covalent manner.[127] Solid-state ^{15}N nuclear magnetic resonance (NMR) experiments indicate the formation of heterocyclic species such as the indole- or indoline-type structures, which is consistent with the above model. However, solid-state ^{13}C NMR analysis confirms

that the cyclized, nitrogenous species are consistent with the formation of a saturated indoline product, rather than an unsaturated indole in the aforementioned model. Moreover, polydopamine has considered to be a supramolecular aggregate of monomers (consisting primarily of 5,6-dihydroxyindoline and its dione derivative), which are cross-linked through noncovalent forces, including charge transfer, π-stacking, and hydrogen bonding interactions. (Figure 3.2.2).

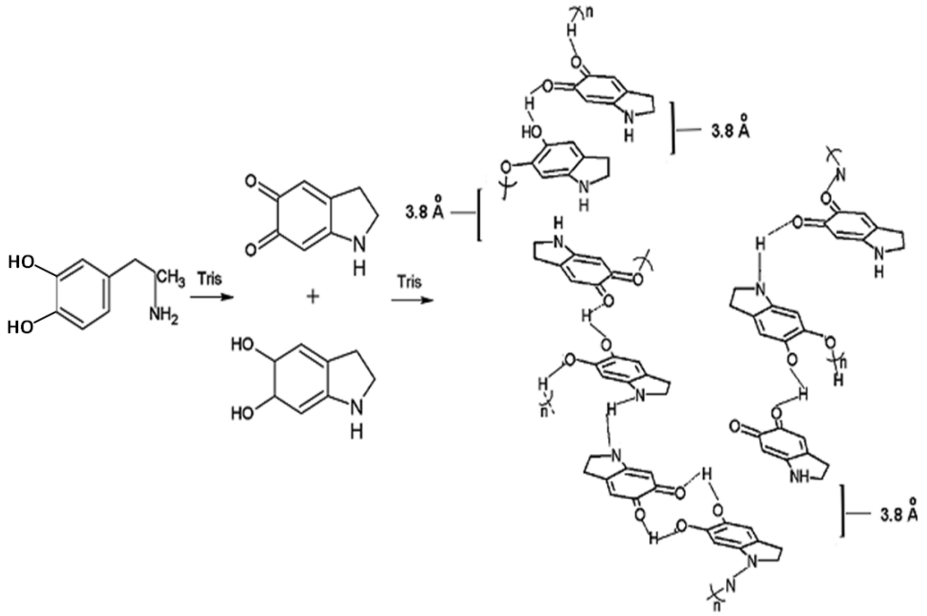

Figure 3.2.2 Proposed formation mechanism of PDA. In this model, PDA is proposed to be comprised of intra- and interchain noncovalent interactions including hydrogen bonding, π-stacking, and charge transfer. Reprinted with permission from ref.[127] Copyright 2012 *American Chemical Society*.

Attention should also be paid to the influence of the pH value on the polymerization process. It has been reported that the thickness of the PDA deposits increases with increasing the pH value of the solution.[128,129] This phenomenon can be explained according to the equilibrium as depicted in Figure 3.2.1. Hydrogen protons produced in the oxidation process will be consumed with increasing pH, and the equilibrium will shift toward the product. In addition, the oxidant involved in the reaction solution is another important factor for the formation of PDA. As illustrated above, oxygen participates in the initial oxidation of dopamine as well as converting 5,6-dihydroxyindole into the corresponding quinone via hydrogen abstraction. Thus, in the deoxygenated solutions, dopamine will not polymerize even at a strongly alkaline environment.[130]

3.2.3.2 In-situ synthesis of metal nanoparticles on PDA

Generally, PDA acts as a versatile layer for the modification of various materials to impart or enhance some specific functions.[131,132] The reducing ability of PDA toward noble metallic salts suggests the potential preparation of metal nanocomposites that display the versatile features of PDA. A representative example is the direct synthesis of metal nanoparticles. Plenty of amino groups and catechol groups in PDA are prone to immobilize and induce metal nanoparticles from in situ reduction of the metal precursor. Metal ions such as Ag^{+}, Pt^{3+}, Au^{3+} are first adsorbed onto the PDA layer and then reduced to the corresponding metal nanoparticles in situ by the catechol groups of PDA while the catechol groups are oxidized to the corresponding quinones simultaneously (Figure 3.2.3).[133,134]

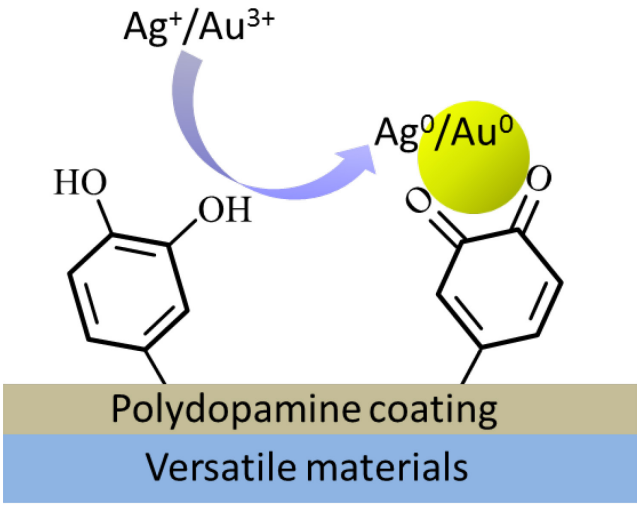

Figure 3.2.3 In-situ deposition of metal nanoparticles on PDA layer.

In this regard, neither metallic seed particles nor additional reducing agents is required. In addition, the PDA layer plays an important role in preventing the metal nanoparticles from agglomeration by the quinones and unoxidized catechol groups. The PDA layer can also serve as stabilizers for the resultant metal (0), which act as the seed precursor for the formation of metal nanoparticles via the atom by atom growth with the continuous reduction of metal ions.

3.3 Catalytic reduction of 4-nitrophenol by Au nanoparticles

Catalysis by metallic nanoparticles is certainly among the most intensely studied problems during recent years.[11,135,136] Au nanoparticles for example have been considered as excellent catalysts in different catalytic reactions, such as oxidations,[137–139] hydrogenations,[140,141]

epoxidations,[142] and C-C coupling reaction.[143] Generally, in order to avoid potential hazards, Au nanoparticles are affixed to a suitable colloidal carrier, which may impede the activity of the nanoparticles for a given reaction.[144] Therefore, a model reaction is required for comparing the catalytic performance of Au nanoparticles immobilized in different carrier systems.

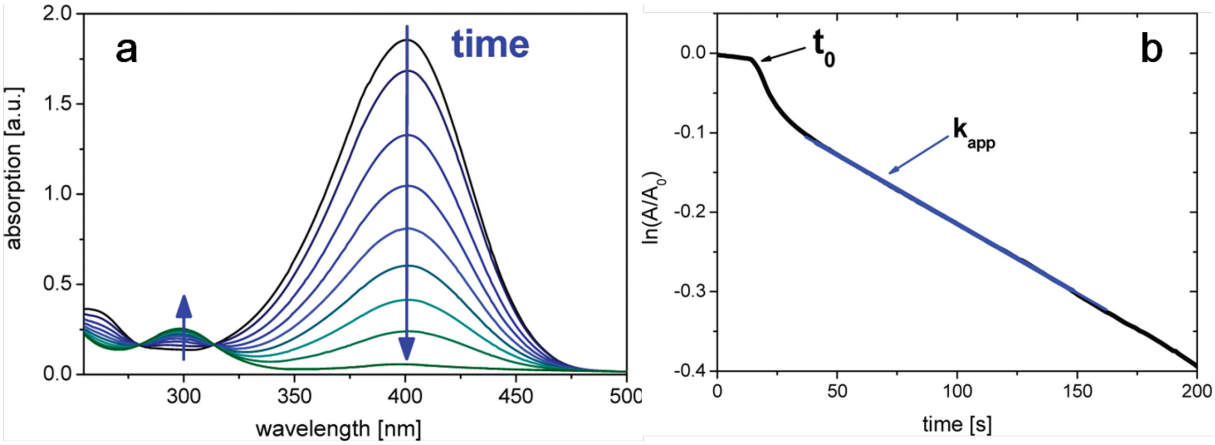

Figure 3.3.1 (a) Absorption spectrum of Nip by sodium borohydride. The main peak of nitrophenolate ions at 400 nm is decreasing with reaction time (blue arrow), while a second peak at 300 nm of Amp is slowly increasing. The two isosbestic points at 280 and 314 nm can be observed. (b) Typical time dependence of the absorption of 4-nitrophenolate ions at 400 nm. The blue portion of the line displays the linear section, from which k_{app} is taken. The induction period t_0 is marked with the black arrow. Reprinted with permission from ref.[145] Copyright 2010 *American Chemical Society*.

The reduction of 4-nitrophenol (Nip) to 4-aminophenol (Amp) by sodium borohydride ($NaBH_4$) has been identified as a such model reaction that can be easily monitored with high precision by UV-Vis spectroscopy.[146] This is due to the fact that the decrease of the strong absorption of 4-nitrophenolate anion at 400 nm can be measured precisely as the function of time. Furthermore, several isosbestic points (Figure 3.3.1a) have been observed in the spectra of the reacting mixtures, indicating that it leads to a single final product without side reactions.[146] Another important feature of the reduction of Nip catalyzed by metal nanoparticles is the induction period, t_0, after which the reaction starts (Figure 3.3.1b). There is strong evidence that t_0 is resulted from the surface-restructuring of the particles surface to render them catalytically active.[147]

The apparent rate constant k_{app} is commonly used to compare the catalytic activity, but it is dependent on the amount of applied catalysts. A comparison of the reaction rate of different catalysts can not be achieved by k_{app}. Thus the reaction rate has to be normalized to be

comparable. Since the reaction takes place on the surface of catalysts, the rate constant k_{app} is therefore expected to be proportional to the total surface S.[148] Hence, the kinetic constants k_{app} and k_1 (the rate constant normalized to S) can be defined through:[149,150]

$$-\frac{dc_{Nip}}{dt} = k_{app}c_{Nip} = k_1 S c_{Nip} \quad (3.3.1)$$

The reaction mechanism for this model reaction hypothesizes that both reactants must be adsorbed on the surface of the nanoparticles to react. [32,33,34] In general, the reaction follows the direct route shown in Figure 3.3.2. Nip is first reduced to 4-nitrosophenol and then quickly to the corresponding 4-hydroxylaminophenol (Hx), which is reduced to the final product Amp in the rate-determining step. The Hx is therefore the only stable intermediate,[153] and the reaction can be treated as a two-step reaction.[154]

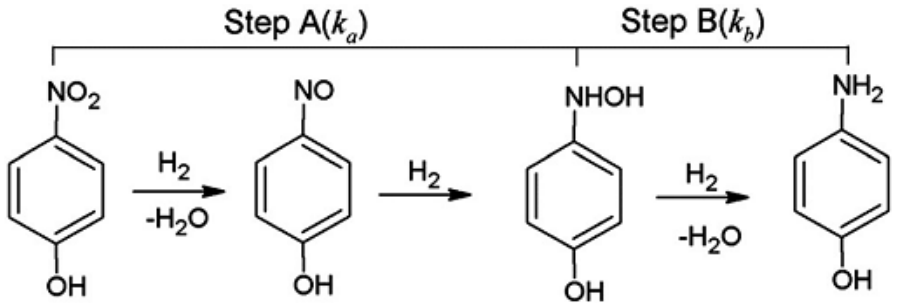

Figure 3.3.2 Proposed mechanism for the reduction of Nip by metallic nanoparticles: in Step A, Nip is first reduced to the 4-nitrosophenol, which is converted to the stable intermediate Hx quickly. Hx is then reduced to the final product Amp in Step B, which is the rate-determining step. All reactions take place at the surface of the particles. There is an adsorption/desorption equilibrium for all compounds in all steps. Reprinted with permission from ref.[154] Copyright 2015 *Royal Society of Chemistry*.

Recently, this reaction has been successfully applied to analyze the spherical polyelectrolyte brushes (SPB) supported Au and Au/Pd nanoalloys systems.[152,154] The analysis yields the full information on the kinetics of the scheme, which can be described by two coupled differential equations. The reaction rate for step A follows as[152]

$$-\frac{dc_{Nip}}{dt} = k_a S \frac{(K_{Nip}c_{Nip})^n K_{BH4}c_{BH4}}{\left[1+(K_{Nip}c_{Nip})^n + K_{Hx}c_{Hx}+K_{BH4}c_{BH4}\right]^2} \quad (3.3.2)$$

The full rate equation for the generation and decay of the intermediate Hx can be obtained by[152]

$$\frac{dc_{Hx}}{dt} = k_a S \frac{(K_{Nip}c_{Nip})^n K_{BH4}c_{BH4}}{\left[1+(K_{Nip}c_{Nip})^n + K_{Hx}c_{Hx}+K_{BH4}c_{BH4}\right]^2}$$

$$-k_b S \frac{K_{Hx}c_{Hx}K_{BH4}c_{BH4}}{\left[1+(K_{Nip}c_{Nip})^n + K_{Hx}c_{Hx}+K_{BH4}c_{BH4}\right]^2} \quad (3.3.3)$$

where, k_a and k_b are the reaction rate constant of step A and B, respectively. K_{Nip}, K_{Hx}, and K_{BH4} are the Langmuir adsorption constants of the respective compounds, and n is the Langmuir–Freundlich exponent.

3.4 Energy storage in electrical double layer capacitors (EDLC)

With the rapidly increasing population, economic development, environmental pollution as well as the depletion of fossil fuels, there is unprecedented interest in sustainable and renewable energy sources.[155–157] It was estimated that the global energy use is projected to double its energy supply by 2050 and to triple by the year 2100. To meet the current and future energy requirements while avoiding environmental deterioration, intensive research efforts have focused on clean and efficient energy storage devices, which are key technologies to deal with the intermittent nature of renewable energy sources.[158–160] Among various energy storage devices, electric double layer capacitors (EDLCs) have recently attracted considerable attention due to their outstanding features, such as ultra-fast charge and discharge rate, high power density, long cycle life, excellent reversibility and safe operation, making them probably the most promising candidates for the next generation energy storage devices.[161,162]

3.4.1 Energy storage mechanism

The main energy storage mechanism in supercapacitors arises from the reversible electrostatic accumulation of ions on the surface of porous carbon materials. The Helmholtz model[163] states that two layers of opposite charge form at the electrode/electrolyte interface and are separated by an atomic distance. This accumulation of charges is called electrical double layer (EDL). The potential in the vicinity of the electrode then decreases when the distance d (m) between the ions and the electrode increases (Figure 3.4.1a).The capacitance C_H of this simplified Helmholtz double-layer, which can be regarded as an electrical capacitor, is defined by equation:[164]

$$C_H = \varepsilon_r \cdot \varepsilon_0 \cdot \frac{S}{d} \quad (3.4.1)$$

where, ε_r and ε_0 are the dielectric constants of the electrolyte solvent and vacuum, S is the surface area of the interface, and d is the effective thickness of the electrical double layer.

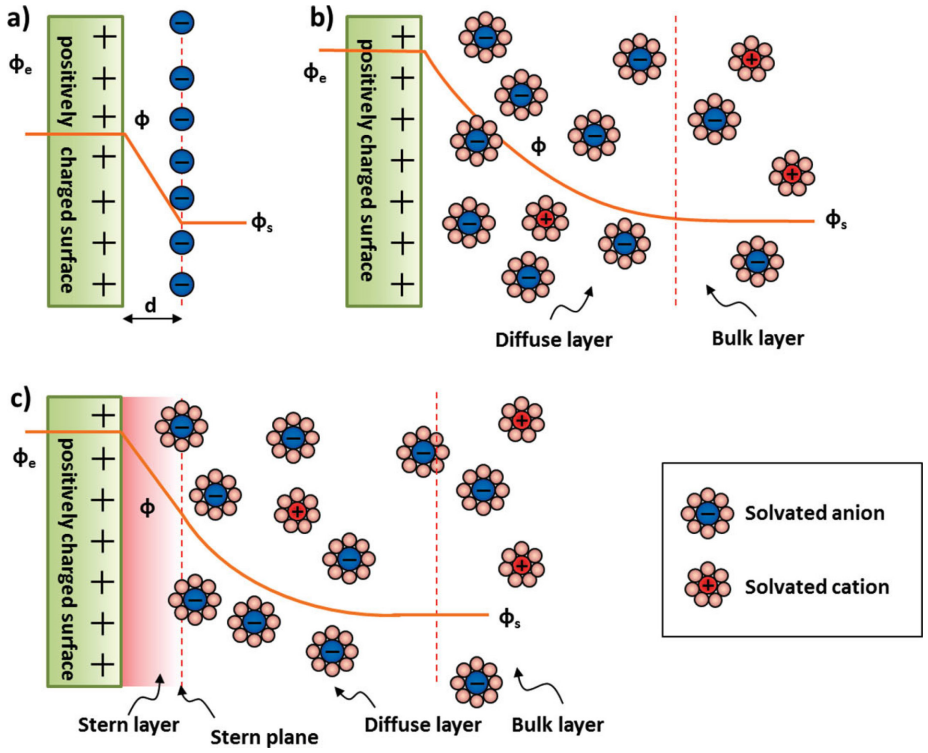

Figure 3.4.1 Models of the electrical double layer at a positively charged surface: (a) the Helmholtz model, (b) the Gouy–Chapman model, and (c) the Stern model, showing the electrical double-layer formed at a positively charged electrode in an aqueous electrolyte. The electrical potential, Φ, decreases when transitioning from the electrode, Φ_e, to the bulk electrolyte infinite away from the electrode surface, Φ_s. The Stern plane marks the distance of closest approach of the ions to the charged surface. Note the absence of charges/ions in the Stern layer. The diffuse layer starts in the range of 10 – 100 nm from the electrode surface. Reprinted with permission from ref.[164] Copyright 2014 *Wiley-VCH*.

This simple Helmholtz EDL model was further modified by Gouy and Chapman[165]. They suggested a diffuse model of the EDL, in which the potential decreases exponentially from the electrode surface to the fluid bulk (Figure 3.4.1b). However, the Gouy–Chapman model is insufficient for highly charged double-layers. Later, Stern proposed a model combining the Helmholtz and Gouy–Chapman models by accounting for the accumulation of ions close to the electrode surface and the hydrodynamic motion of the ionic species in the diffuse layer (Figure 3.4.1c). Thus, the total capacitance of the electrode (C_{DL}) can be treated as a combination of the capacitances from Helmholtz layer (C_H) and the diffuse layer (C_D). C_{DL}

can be expressed by the following equation:[164]

$$\frac{1}{C_{DL}} = \frac{1}{C_H} + \frac{1}{C_D} \tag{3.4.2}$$

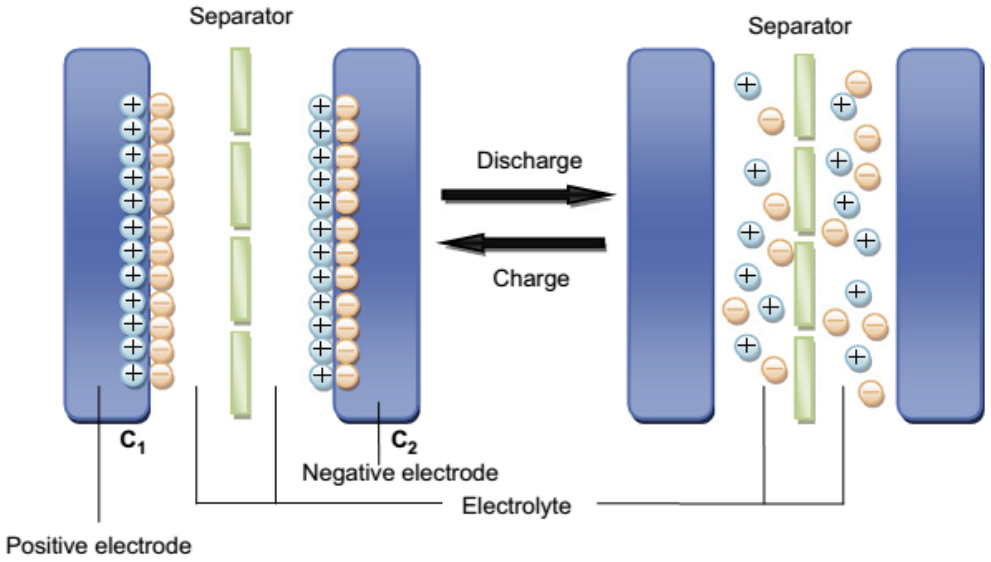

Figure 3.4.2 (a) charged and discharged states of a symmetric electrical double layer capacitor. Reprinted with permission from ref.[166] Copyright 2013 *Elservier*.

An EDLC is composed of two electrodes made of carbonaceous materials, which are soaked in an electrolyte and separated by a porous membrane separator (Figure 3.4.2). When an electrical potential difference is applied on an EDLC cell, the positive electrode electrostatically adsorbs solvated anions while the negative electrode is neutralized by a layer of solvated cations, thus forming an electrical double layer on the surface of each electrode. According to Figure 3.4.2, in its charged state, a supercapacitor is equivalent to two capacitors of capacitance C_1 and C_2 in series. The capacitance of the total system is given by equation:[164]

$$\frac{1}{C} = \frac{1}{C_1} + \frac{1}{C_2} \tag{3.4.3}$$

where, C is the cell capacitance, C_1 and C_2 are the respective capacitances of the positive and negative electrodes, respectively.

To provide a basis for comparison between different electrode materials, it has become common practice to provide a specific gravimetric capacitance C_{SP} (F/g), which is related to the capacitance of one single electrode. In case of a symmetric system, where both electrodes are equal in mass, thickness, size, and material, equation (3.4.4) can be used.[164]

$$C_{sp} = 4 \cdot \frac{C}{M} = 4 \cdot \frac{I \cdot \Delta t}{M \cdot V} \quad (3.4.4)$$

where, M (kg) is the total mass of active materials, and V (V) is the operating voltage, depending on the electrolyte stability window. The factor 4 is related to normalization to the mass of one electrode for the two identical capacitors in series.

The specific energy density E (Wh/kg) and power density P (W/kg) in a supercapacitor can be obtained according to equations (3.4.5) and (3.4.6), respectively:[164]

$$E = \frac{C \cdot V^2}{2 \cdot M \cdot 3600} \quad (3.4.5)$$

$$P = \frac{V^2}{4 \cdot R_S \cdot M} \quad (3.4.6)$$

where, R_s (Ω) is the equivalent series resistance (ESR) of the system. The sum of the resistances is related to the intrinsic resistance of the electrode materials, the interface resistances between the electrode materials and current collectors, the electrolyte resistance, and the ionic resistance of the electrolyte in the separator. As indicated from equations (3.4.5) and (3.4.6), high surface area, wide operating cell voltage, and minimum ESR are required in order to achieve excellent performance for a supercapacitor.

3.4.2 Electrode materials

Nanostructured materials have significantly accelerated the development of supercapacitors because of their several advantages over bulk counterparts as described below: 1) Nanostructured materials can be designed to have a high specific surface area, which provides more ion adsorption or active sites for the formation of electrical double-layer and charge-transfer reactions, resulting in the enhanced specific capacitance. 2) Nanoscale active materials have short diffusion and transport pathways of electrolyte ions within the particles, facilitating the transport of electrolyte ions and accordingly improving the effective electrochemical utilization of active materials and high rate charge/discharge capability. In classical electrochemistry theory, the ion diffusion time constant (τ) can be expressed by the equation (3.4.7):[167]

$$\tau = \frac{L^2}{2D} \quad (3.4.7)$$

where, D is ion transport coefficient, and L is ion diffusion length, which is a critical factor

that determines ion transport resistance, and subsequently determines the rate handling ability of supercapacitors.[167–169] It is obvious that the ion diffusion time decreases with decreasing particle sizes. 3) The small size of particles could effectively buffer the stress from the expansion and shrinkage of the electrodes during the charge/discharge process, preventing the pulverization of electrode and improving the cycle stability. 4) The large surface area of nanostructured materials increases the contact area between electrode and electrolyte, resulting in higher ion flux compared to the bulk one.

3.4.3 Aqueous electrolyte

The two main parameters for selection of an electrolyte are the electrochemical stability window and the ionic conductivity, which strongly determine the specific energy density and the specific power density, respectively. Concentrated acid-based (*e.g.,* H_2SO_4) and alkali (*e.g.,* KOH) aqueous electrolytes with a higher conductivity (up to ~1 S/cm) are normally used in order to overcome the ESR factor, thus giving the system a higher power performance (Equation 3.4.6). However, due to the highly corrosive in nature for current collectors, most of the researches in KOH and H_2SO_4 have been performed using gold current collectors. In addition, the operating voltage window in these media is less than 1 V because of the narrow electrochemical stability window (1.23 V) of water.[170] Consequently, the energy stored in the device is limited (Equation 3.4.5). Recently, it has been demonstrated that it is possible to increase the operating voltage of carbon based supercapacitors in aqueous H_2SO_4 up to 1.6 V, by adjusting the mass of electrodes and/or by using different optimized carbons as positive and negative electrodes.[171] It is important to note that the overpotential for electrolyte decomposition varies depending on the used carbon.

To mitigate the limitations in both acidic and alkaline media, neutral pH electrolytes have been investigated. Voltage values up to 2 V with good charge/discharge cycle life have been observed for activated carbons in Na_2SO_4 and Li_2SO_4.[172,173] The utilization of neutral aqueous electrolytes, such as lithium sulfate, not only prevents the corrosion, but also realizes high voltage and energy density supercapacitors with environmental friendly, cost effective and safe materials.

4. In-situ generation of catalytically active Au nanoparticles onto gibbsite-polydopamine (G-PDA) core-shell nanoplates

In this chapter, we explore the effectiveness of a dopamine-based approach for the encapsulation of platelet-like gibbsite particles to synthesize anisotropic G-PDA core-shell nanoplates. Additionally, G-PDA core-shell nanoplates have been applied as a support to fabricate gibbsite-polydopamine-Au (G-PDA-Au) composite particles which can be effectively separated and recycled for catalysis. The work of this part aims at the synthesis and characterization of G-PDA-Au composite particles and their catalytic activity.

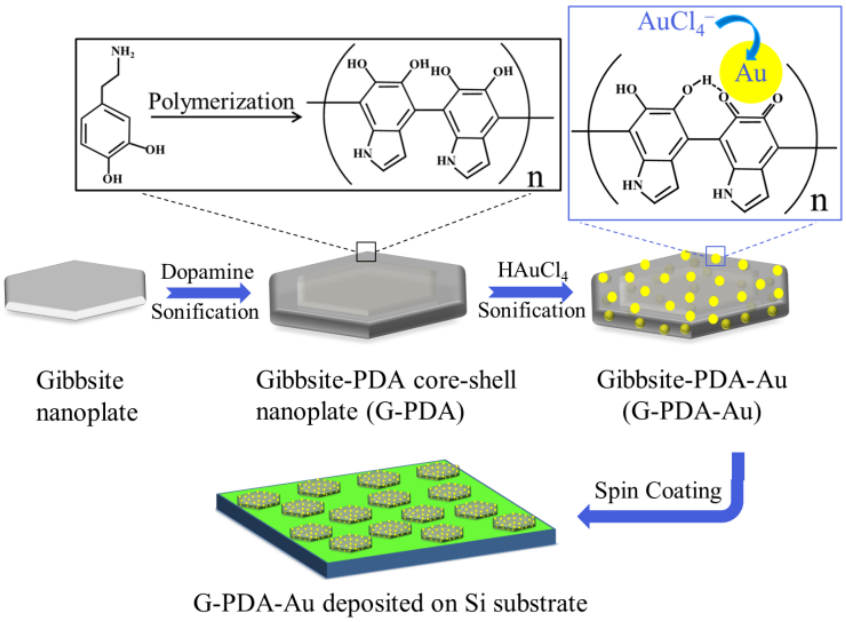

Scheme 1 Synthesis of gibbsite-polydopamine-Au core-shell nanoplates.

Typically, the synthesis of these particles is performed in two steps as shown in Scheme 1: Positively charged gibbsite nanoplates are first modified by poly(acrylic acid sodium salt) (PAA-Na), which can adsorb dopamine through the complexation of COO^- and H_3N^+ groups. Dopamine is self-polymerized on the surface of gibbsite particles under ultrasonification. In the second step, Au NPs are anchored on the surface of G-PDA particles in situ without introducing additional reducing agent or surfactant. The influence of the concentration of $HAuCl_4$ precursor and reaction time on the morphology of Au NPs has been investigated in detail. The catalytic activity of the synthesized G-PDA-Au nanocomposites has been tested for the catalytic reduction of 4-nitrophenol and Rodamine B in the presence of $NaBH_4$. In

addition, the plate-like composite particles has been deposited onto silicon substrate to test the recyclability of the catalyst.

4.1 G-PDA core-shell nanoplates

4.1.1 Gibbsite platelets

Gibbsite platelets have been synthesized according to the method developed by Wierenga *et al.*[95] On dissolving aluminum sec-butoxide (ASB) and aluminum isopropoxide (AIP), the pH of the solution changes from 1 to 4.6 after 10 days' mixing, but ASB and AIP are not completely dissolved. The turbidity of the mixture depends on the dissolution time (1-2 weeks). A clear solution is not expected, since above the Al/Cl ratio of 1.5, gibbsite is formed.[174] The solid content of the dialyzed samples is around 8 g/L. The sediment can be redispersed easily in water. Particles after centrifugation are used directly for further experiments. TEM measurement is performed to investigate the morphology and size distribution of the synthesized gibbsite platelets. The TEM image in Figure 4.1.1a shows the homogeneous hexagonal shape of the obtained gibbsite platelets. By measuring the surface area of over 200 individual particles, the average equivalent circular diameter (ECD) of 198 nm (σ_{ECD} = 25 nm) has been determined (Figure 4.1.1b). The zeta-potential of the as-prepared gibbsite platelets is 40.3 mV, indicating the positive charge of the particle surface.

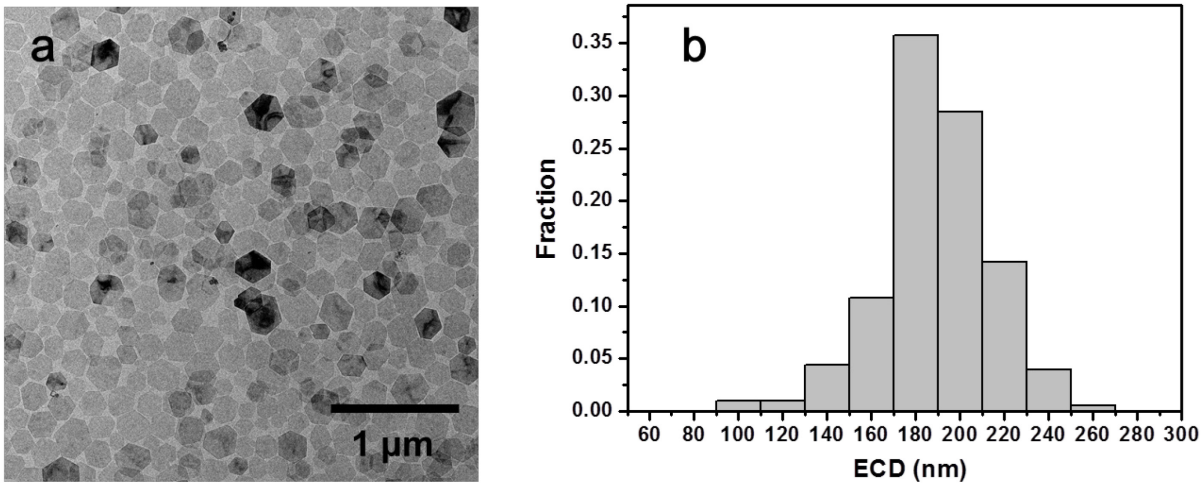

Figure 4.1.1 (a) TEM image of the colloidal gibbsite platelets. (b) Scatter diagram of the equivalent circular diameter (ECD) of the platelet surface as determined from transmission micrographs with average size of 198 ± 25 nm.

Figure 4.1.2a shows the XRD patterns of the gibbsite platelets. Diffraction peaks at 2θ angle of 18.3°, 20.4° and 30.2° can be found for the gibbsite platelets, which are assigned to (002), (110) and (004) planes of the gibbsite platelets, respectively. Figure 4.1.2b shows the TGA/DTA curve of the gibbsite platelets. The measured DTA curve is in agreement with the DTA curve of fine-grade commercial gibbsite platelets.[94] The same transitions can be observed in both the DTA and the TGA curves: at around 100 °C intercrystalline water evaporates, and at around 305 °C gibbsite transforms to Al_2O_3 (presumably of the type χ-Al_2O_3).[95] The weight loss of about 35% between 100 °C and 1000 °C as observed in the TGA curve indeed corresponds to the change in weight resulting from the dehydration reaction of the gibbsite platelets: $2Al(OH)_3 \rightarrow Al_2O_3 + 3H_2O$

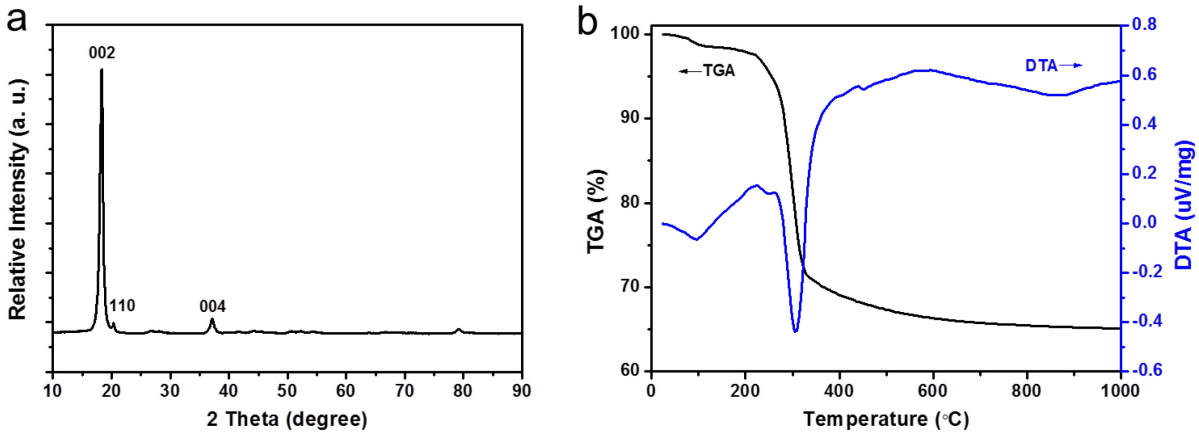

Figure 4.1.2 (a) XRD patterns of the gibbsite platelets. (b) TGA (black) and DTA (blue) curve of the gibbsite platelets.

4.1.2 PDA coating

Before PDA coating the gibbsite platelets have been treated with negatively charged PAA-Na. The deposition of PAA-Na on the gibbsite surface has been confirmed by the zeta-potential measurement with a negative value of -65.0 mV. Dopamine monomer can thus be adsorbed onto the negatively charged gibbsite surface to form the $–COO^-H_3N^+$ ion pairs via electrostatic interactions in the Tris buffer (pH 8.5) solution. G-PDA core-shell particles can then be synthesized through the self-polymerization of dopamine on the surface of PAA-modified gibbsite platelets. Although the exact polymerization mechanism is still not clear at the moment, it is likely to involve oxidation of catechol to a quinine, followed by polymerization in a manner reminiscent of melanin formation, which occurs through the polymerization of structurally similar compounds.[175]

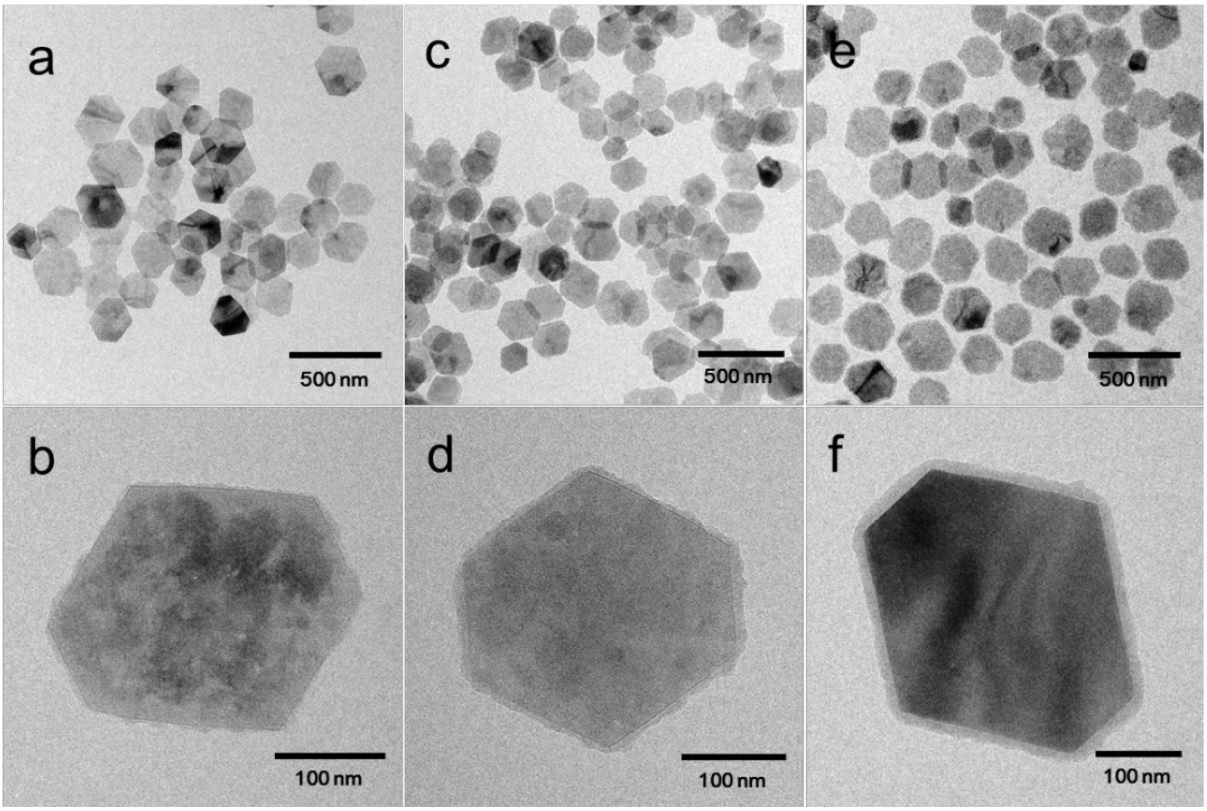

Figure 4.1.3 TEM images of the G-PDA core-shell particles prepared under different reaction times: 3 h (a, b), 6 h (c, d), 9 h (e, f), respectively.

As reported,[176] the PDA surface roughness is closely related to the deposition speed. Higher dopamine concentration leads to a relatively faster polymerization speed, resulting in a rougher PDA film. Thus, in the present work 0.5 $mg \cdot mL^{-1}$ of dopamine has been chosen for subsequent experiments, which is much lower than reported in order to guarantee as few defects as possible.[57] The controllable surface coating of the gibbsite is realized with the same dopamine concentration (0.5 $mg \cdot mL^{-1}$) under various reaction times. Figure 4.1.3 displays the typical TEM images of the G-PDA core-shell particles synthesized under different reaction times. In all cases, no aggregation has been found after PDA coating. The evenly coating of the PDA shell onto the gibbsite nanoplates can be distinguished clearly from the TEM images according to the low contrast of PDA, which demonstrates a well-defined encapsulation of gibbsite nanoplates with the PDA shell. Importantly, the thickness of the PDA shell can be efficiently adjusted by the reaction time. The average thickness of the PDA shell increases from 3 nm (Figure 4.1.3b) to 8 nm (Figure 4.1.3d) and 14 nm (Figure 4.1.3f) when the reaction time increases from 3 h to 6 h and 9 h, respectively. As can be seen clearly from Figure 4.1.3f, the composite particles constitute two distinct components: a black core of gibbsite and a gray shell of PDA. No changes in size or shape of the gibbsite cores are observed; thereby a well-defined

G-PDA core-shell structure has been successfully obtained. Furthermore, a clear interface between the polydopamine shell and the gibbsite core can be observed, indicating tight encapsulation. The gibbsite core is well wrapped by the PDA layer. The average thickness of the PDA shell is about 14 nm. In addition to this, the transforming of the surface charge of the composite particles in acid and alkaline solutions is confirmed by zeta potential measurements. The zeta potential of 26.8 mV turns dramatically to -38.0 mV when the pH value varies from 2.0 to 8.5. This is due to the reaction that the PDA shell is negatively charged at high pH because of the deprotonation of the phenolic group, while it is positively charged at low pH because of the protonation of the amino group.

It is worth noting that ultrasonification is quite essential for the preventing of the aggregation of PDA particles during the polymerization. As shown in Figure 4.1.4a, performing the self-polymerization of dopamine under stirring instead of constant ultrasonification leads to the formation of aggregates with protrusions. (see the large protrusions marked with black arrows in Figure 4.1.4b)

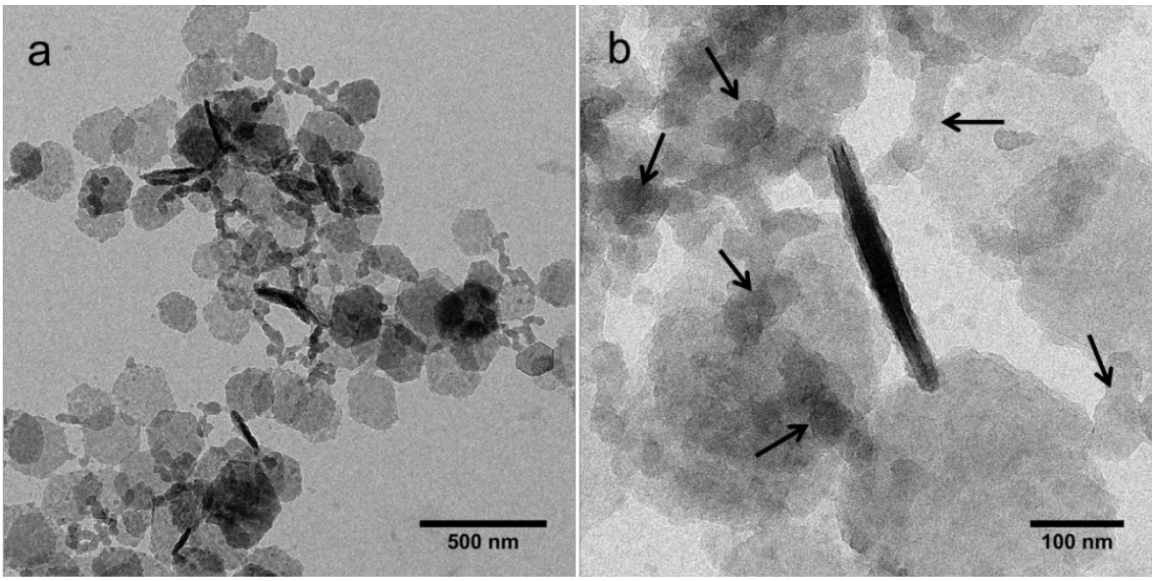

Figure 4.1.4 TEM images of G-PDA core-shell particles synthesized without constant sonification.

Over the last few years, the focus of synthetic opals has attracted increasing attention. Researchers have recognized that both spherical and anisometric colloidal particles can form crystal structures that exhibit Bragg reflection of visible light.[177–179] For instance, an iridescent smectic phase was observed as early as 1925 in suspensions of rod-like β-FeOOH.[180] Later, iridescent lamellar phases of tungstic acid and phospate antimonite were observed.[181,182] Recently, the liquid crystal phase behavior of colloidal gibbsite platelets has been explored.[102]

In particular, suspensions of both sterically and charge stabilized gibbsite platelets[183–185] display beautiful iridescence at sufficiently high concentrations, which are due to Bragg reflections by the columnar arrangement.[186,187] Under normal gravity, the gibbsite suspensions develop sediments with iridescence on a timescale of years. The formation process of an opal-like columnar crystal for both gibbsite platelets and silica coated gibbsite particles can be sped up by modest centrifugation forces.[34,103]

In our study, G-PDA core-shell nanoplates are colloidal stable in aqueous solution, which show black color (Figure 4.1.5a). Dispersions of the G-PDA nanoplates in water are then centrifuged and inspected under white illumination directly after centrifugation. As shown in Figure 4.1.5b, bright Bragg reflections are visible in ring shaped layers at the bottom of the tubes, indicating the formation of columnar phases. When the tubes are inspected upside down, a flow of previously sedimented material emerges along the walls of the tube. Even during flow, bright Bragg reflections remain visible in the sediment. This indicates that colloidal gibbsite particles still keep uniform in shape and size after PDA coating, which is crucial for the formation of the opal-like columnar crystal with iridescent Bragg reflections.

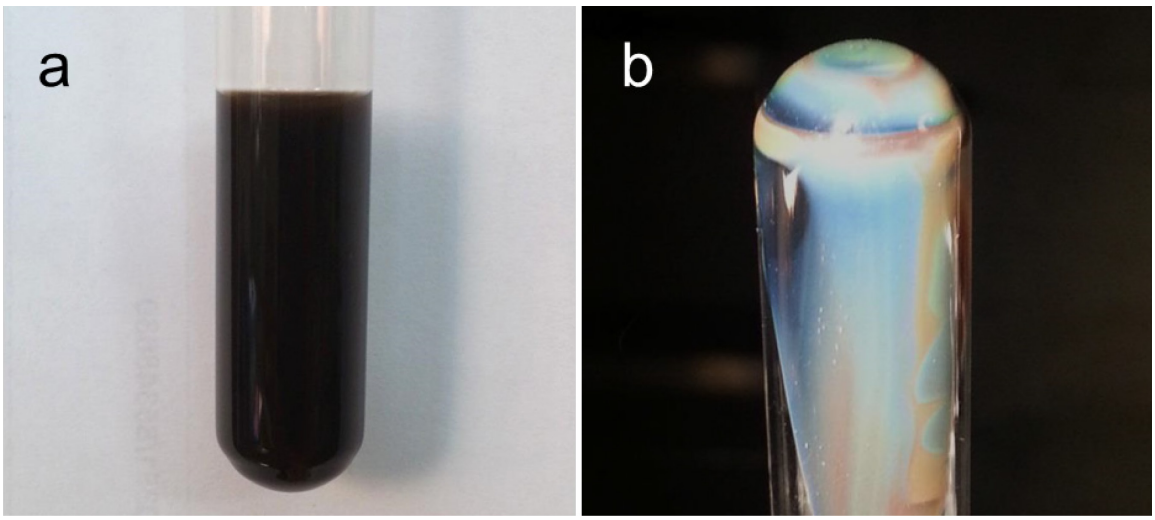

Figure 4.1.5 (a) G-PDA core-shell nanoplates dispersed in water, (b) Centrifugation (3 h, 300 g) of the G-PDA particles leads to the formation of columnar phases in water as is observed from iridescence.

In conclusion, we present a facile approach to synthesize anisotropic plate-like gibbsite-polymer core-shell particles. Hexagonal shaped gibbiste platelets with an average size of 198 nm have been firstly synthesized and characterized by TEM, XRD and TGA measurements. Dopamine is then self-polymerized on the surface of PAA-Na modified gibbsite nanoplates and forms a homogenous layer on it. TEM characterization of the

resulting latexes demonstrates the formation of well-defined plate-like core-shell particles. The thickness of the PDA shell can be efficiently adjusted by controlling the reaction time. Moreover, ultrasonification is found to be an important factor to avoid aggregation. Good control over the plate-like morphology and 100 % encapsulation efficiency have been achieved via this novel route. The resulted well-defined gibbsite-polydamine (G-PDA) core-shell nanoplates show excellent colloidal stability and can form opal-like columnar crystal with iridescent Brag reflection after modest centrifugation. This environment-friendly and facile approach demonstrates the controllable deposition of PDA onto the anisotropic particles with designed thickness, opening opportunities for the design of well encapsulated inorganic-organic anisotropic particles and broadening their applications in catalysis.

4.2 In-situ synthesis of G-PDA-Au nanocomposites

Noble metal nanoparticles have attracted much attention recently due to their unique optical, catalytic, and electrochemical properties, which endow them with high potentials in different areas.[188] Among them, Au nanoparticles have been proven as an active catalyst in a number of oxidation and reduction reactions.[189] The formation of metal nanoparticles is usually carried out by reduction of metal ions in the presence of a stabilizer such as dendrimers,[190,191] micelles,[192] polymers,[193,194] microgels,[195] carbon nanotubes,[196] surfactants,[197] or colloids,[198] which can not only prevent the nanoparticles from aggregating, but also serve as carrier. For instance, Ballauff *et al.* have proved that spherical polyelectrolyte brushes (SPB) and thermosensitive core-shell microgels are excellent model systems for the generation and immobilization of metal nanoparticles like Au, Ag, Pd and Pt.[20,22,23] However, reducing agents such as $NaBH_4$ and sodium citrate are normally required in a typical synthesis, which results in a random distribution of metal nanoparticles by using this approach. PDA as mentioned above has been proved to be an alternative for the in-situ synthesis of metallic nanoparticles due to the apparent reductive and stabilizing capacity of the catechol groups.[65] Studies on one-step generation of Au or Ag nanocatalysts using PDA as dual roles of reductant and stabilizer have been reported in some literatures.[69,70] There is a systematic lack of effective investigations on the relationship between gold concentration and reaction time on size and distribution/amount of Au nanoparticles on the PDA.

4.2.1 Influence of the $HAuCl_4$ concentration on the morphology of Au nanoparticles

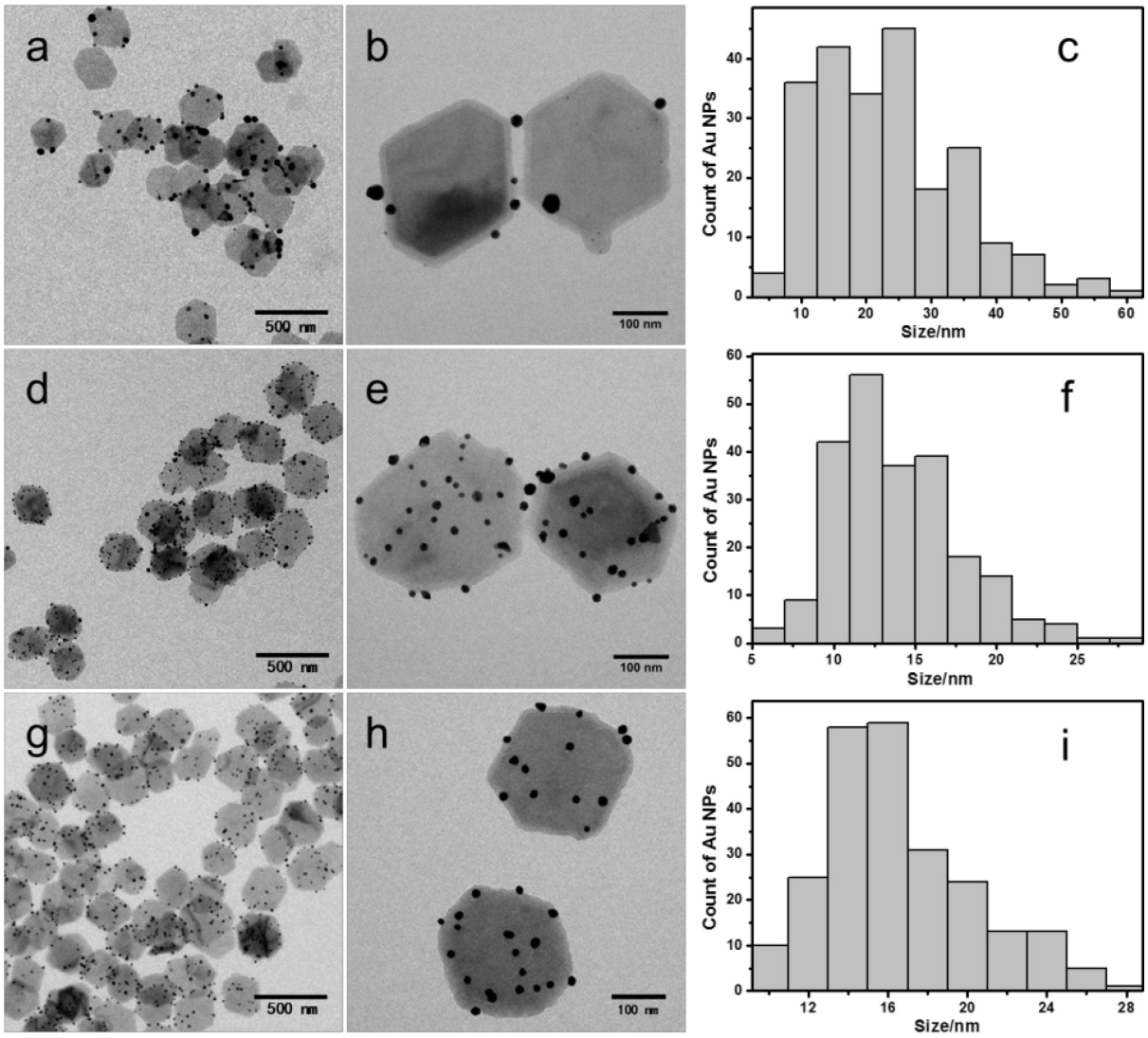

Figure 4.2.1 TEM images of the G-PDA-Au composite particles prepared with different concentration of $HAuCl_4$, and its corresponding size distribution curve of Au nanoparticles deposited on G-PDA. (a, b, c) 0.25 mM, (d, e, f) 0.1 mM, and (g, h, i) 0.05 mM after ultrasonification for 8 min.

In this work, core-shell structured G-PDA-Au nanocomposites are prepared by adding the as-synthesized G-PDA to a $HAuCl_4$ solution. The possible mechanism of the generation and stabilization of Au nanoparticles on the PDA shell is speculated in Scheme. 1. Au precursor ($AuCl_4^-$ ions) is diffused onto the PDA shell and then reduced to Au nanoparticles in situ by the catechol groups of PDA while the catechol groups are oxidized to corresponding quinones simultaneously.[200] No additional reducing agent or thermo treatment is required in this case. The catechol groups of PDA on the surface of the gibbsite particles work not only as reducing agents but also as stabilizers which can help to prevent the Au nanoparticles from

agglomeration. As shown in Figure 4.2.1, individual Au nanoparticles are well distributed on the surface of the G-PDA particles, demonstrating that the PDA molecules effectively prevent the Au nanoparticles from agglomeration. In addition, the G-PDA-Au nanocomposites still remain the plate-like morphology after the deposition of Au nanoparticles.

In order to investigate the influence of the $HAuCl_4$ concentration on the morphology of Au nanoparticles generated on the PDA shell, different amounts of Au precursor have been used for the preparation of Au nanoparticles at fixed reaction time. Representative TEM images and the corresponding size distribution of Au nanoparticles are presented in Figure 4.2.1. The loading amount and size of the Au nanoparticles show strong dependency on the dosage of $HAuCl_4$. When 0.25 mM of $HAuCl_4$ is used, Au nanoparticles with broad size distribution ranging from 6.9 nm to 62.7 nm have been formed on the PDA shell (Figure 4.2.1a, b and c). It is caused by the fast redox reaction between the catechol groups and $AuCl_4^-$ ions, which results in the uncontrolled particle deposition. The loading amount of the Au nanoparticles in the composites is determined to be 39.10 wt% via TGA measurements. Decreasing the concentration of $HAuCl_4$ to 0.1 mM leads to the formation of more and smaller Au nanoparticles with diameter of 13.9 nm, which are homogenously distributed on the PDA surface (Figure 4.2.1d, e and f). The loading amount of the Au nanoparticles is decreased to be 17.52 wt%. When the concentration of $HAuCl_4$ is further decreased to 0.05 mM, the number of the Au nanoparticles decreases slightly and the loading amount is 10.95 wt%. No obvious change has been found for the size of the Au nanoparticles in this case (Figure 4.2.1g, h and i). Table 4.2.1 summarizes the loading amount and size of the Au nanoparticles formed under different reaction conditions, which indicates that the concentration of the Au precursor plays an important role on the final morphology of the Au nanoparticles. In general, at a fixed reaction time, the loading amount of the Au nanoparticles generated in the system decreases with the decrease of Au precursor concentration.

4.2.2 Influence of the reaction time on the morphology of Au nanoparticles

The influence of the reaction time on the morphology of the Au nanoparticles has been also investigated by keeping the $HAuCl_4$ concentration constant. When the reaction time decreases from 8 min to 4 min, numerous uniformly distributed Au nanoparticles with an average size of 11.7 nm (Figure 4.2.2a, b and c) have been formed on the PDA shell. When the reaction time decreases to 0.5 min (Figure 4.2.2d, e and f), the loading amount of Au nanoparticles on the G-PDA nanoplates is significantly decreased from 13.97 wt% to 7.38 wt% as shown in

Table 4.2.1. This indicates that reduction of the reaction time also leads to the decrease of Au loading.

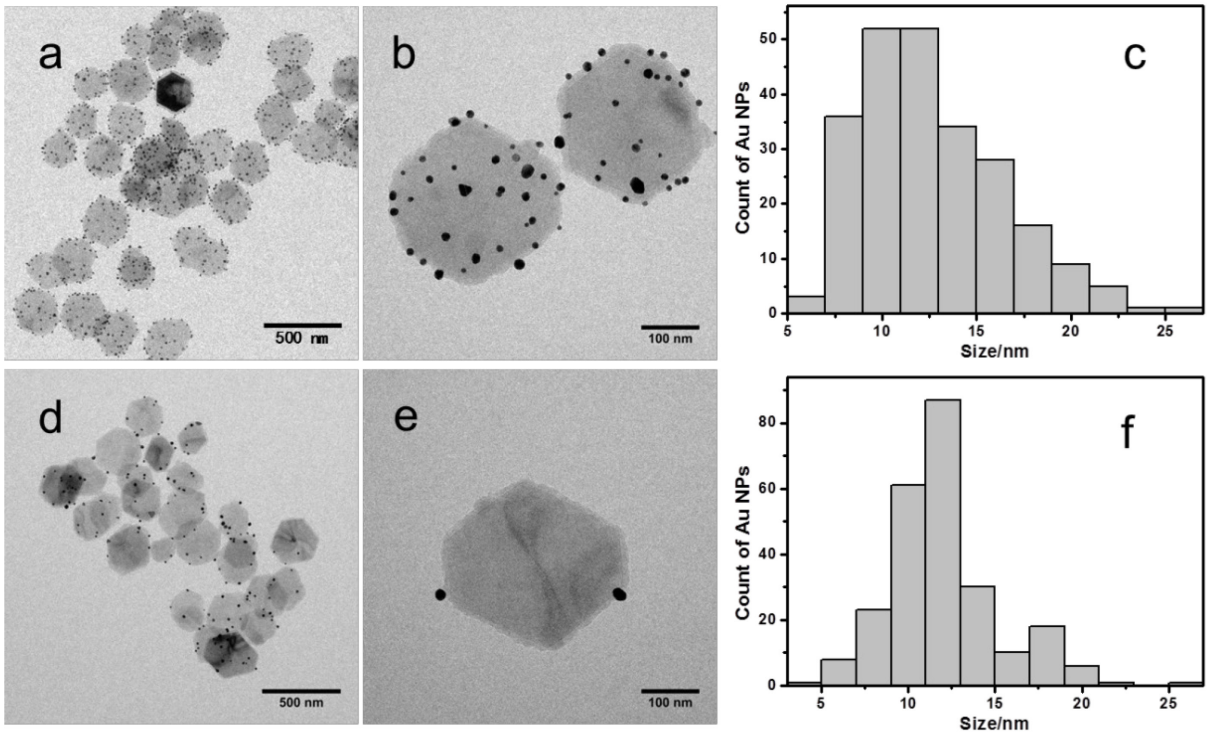

Figure 4.2.2 TEM images of the as-prepared G-PDA-Au nanoparticles under different ultrasonification times, and its corresponding size distribution curve of Au nanoparticles deposited on G-PDA. (a, b and c) 4 min, (d, e and f) 0.5 min in 0.1 mM $HAuCl_4$ solution.

Table 4.2.1 Au nanoparticles with various sizes synthesized under different reaction conditions.

No.	PDA thickness (nm)	c_{HAuCl4} (mM)	Reaction time (min)	Diameter of Au nanoparticles* (nm)	Au loading** (wt%)
1	14	0.25	8	29.1 ± 9.2	39.10
2	14	0.1	8	13.9 ± 4.6	17.52
3	14	0.05	8	15.5 ± 3.6	10.95
4	14	0.1	4	11.7 ± 3.6	13.97
5	14	0.1	0.5	11.1 ± 3.2	7.38

* determined by TEM; ** determined by TGA.

Figure 4.2.3 shows the XRD patterns of the gibbsite platelets and the G-PDA-Au particles. All diffraction peaks in the red spectrum can be easily indexed as the gibbsite platelets, which match well with the reported data. In the pattern of G-PDA-Au (black), the diffraction peaks at (002) and (110) planes have been also found, indicating that the amorphous PDA coating

does not change the crystalline phase of the gibbsite. In addition, four new diffraction peaks of 2θ at 38.2°, 43.0°, 64.6°and 78.1° appear, which are assigned to the (111), (200), (220) and (311) of Bragg reflection of the face-centered cubic (*fcc*) structured Au, respectively.

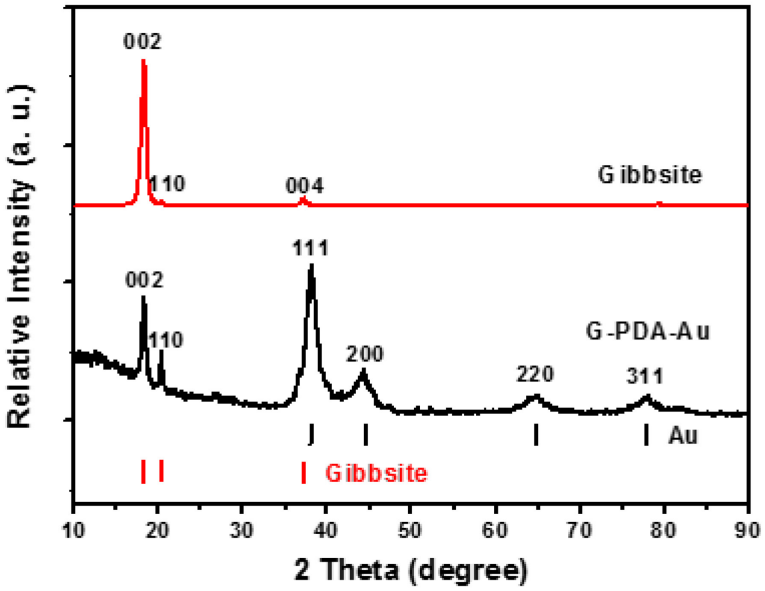

Figure 4.2.3 XRD patterns of the gibbsite and the G-PDA-Au nanoparticles.

In conclusion, anisotropic G-PDA-Au nanocomposites have been synthesized by simply mixing the G-PDA core-shell particles with Au precursor. PDA shell serves as a reductant as well as a stabilizer for the generation of Au nanoparticles in situ so that additional reducing agents and thermal treatment are not necessary. TEM and XRD characterizations of the resulting nanocomposites demonstrate *fcc*-structured Au nanoparticles with tunable size are well dispersed on the G-PDA particle surface without agglomeration. It is found that both the concentration of the Au precursor and the reaction time play important roles on the final morphology of the Au nanoparticles. In general, the loading amount of Au nanoparticles generated in the system decreases with the decrease of the Au precursor concentration at a fixed reaction time. Reducing the reaction time also leads to the decrease of Au loading.

4.3 Catalytic application of G-PDA-Au nanocomposites

4.3.1 Reduction of 4-nitrophenol

Au nanoparticles are well-known to be catalytically active for reduction and oxidation reactions.[201] The introduction of Au nanoparticles onto the surface of G-PDA nanoplates might offer good catalytic reactivity to the composites. Considering that the catalytic

performance of Au nanoparticles is greatly dependent on their size and size distribution, G-PDA-Au-1 nanocomposites prepared under ultrasonification for 4 min in 0.1 mM $HAuCl_4$ has been selected for the catalysis test. The reduction of 4-nitrophenol (Nip) to 4-aminophenol (Amp) in the presence of $NaBH_4$ has been chosen as a model reaction.[146] Since the concentration of $NaBH_4$ is much higher than that of Nip, the reaction can be analyzed by a first order rate law.

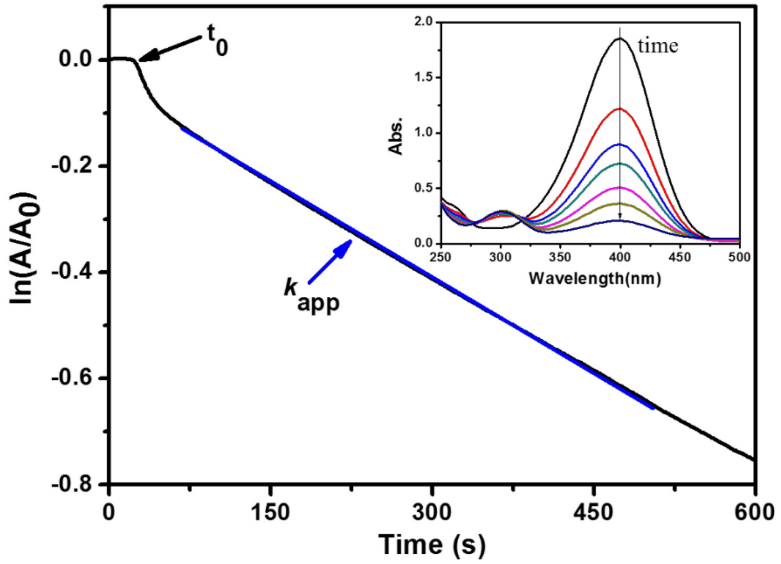

Figure 4.3.1 Typical time dependence of the absorption of 4-nitrophenolate ions at 400 nm. Inset: UV-Vis absorption spectra of Nip during the catalytic reaction using G-PDA-Au-1 particles as catalyst.

The inset of Figure 4.3.1 shows the typical UV-Vis absorption spectra during the reaction with the characteristic peaks of 4-nitrophenolate ions at 400 nm. After the addition of G-PDA-Au-1 nanocomposites into the reaction mixture, the absorption of 4-nitrophenolate ions at 400 nm successively decreases, while a new peak of Amp at 295 nm appears. These indicate the gradual reduction of 4-nitrophenolate to Amp using G-PDA-Au-1 nanocomposites as the catalyst. From this plot, Figure 4.3.1 can be obtained by normalizing with the absorption at 400 nm at a given time (A) by the absorption at 400 nm at t = 0 s (A_0). Firstly, there is a decay time in which no reduction takes place. The induction period t_0 was related to a surface restructuring of the nanoparticles before the catalytic reaction starts.[151] Then the reaction starts and after an intermediate period the reaction becomes stationary. The apparent rate constant k_{app} is taken from the slope of this linear section (marked with blue). The apparent rate constant k_{app} is defined through the following equation:

$$-\frac{dc_{Nip}}{dt} = k_{app}c_{Nip}$$

Our previous study on the kinetics of this reduction demonstrates that the reduction of Nip follows the direct route.[202] 4-hydroxylaminophenol is the only stable intermediate. In the early stage of the reaction, Nip is reduced to 4-hydroxylaminophenol (Hx). In the second step, Hx is reduced to the final product, namely 4-aminophenol (Amp), which is the rate-determining step.[152]

Figure 4.3.2a shows the linear relationships of ln (c_t/c_0) versus time (t). It is observed that the catalytic activity for Nip increases with the increase of Au nanoparticles dosage. Recent work on the kinetic study of Au nanoparticles for the reduction of Nip has clearly revealed that the reduction proceeds on the surface of the Au nanoparticles.[87,203] The rate constant k_{app} is therefore expected to be proportional to the total surface S of the Au nanoparticles present in the system: $k_{app} = k_1 S$, where k_1 is the rate constant normalized to S, the surface area of Au nanoparticles normalized to the unit volume of the system.[204,205] The specific surface S can be calculated from the total amount of Au in the sample (13.97 wt% in the G-PDA-Au-1 nanocomposites), the average size of the Au nanoparticles (d = 11.7 nm), and the density of gold (19.3 g/cm^3). Figure 4.3.2b demonstrates that the apparent rate constant k_{app} depends linearly on the specific surface area of G-PDA-Au-1 nanocomposites as expected. From the linear fit we obtain $k_1 = 0.080$ s^{-1}·m^{-2}·L, which is 10 times larger than that of CTAB-stabilized Au nanoparticles ($k_1 = 0.008$ s^{-1}·m^{-2}·L) with similar size (d = 10.9 nm) that has been reported for the same reaction.[206]

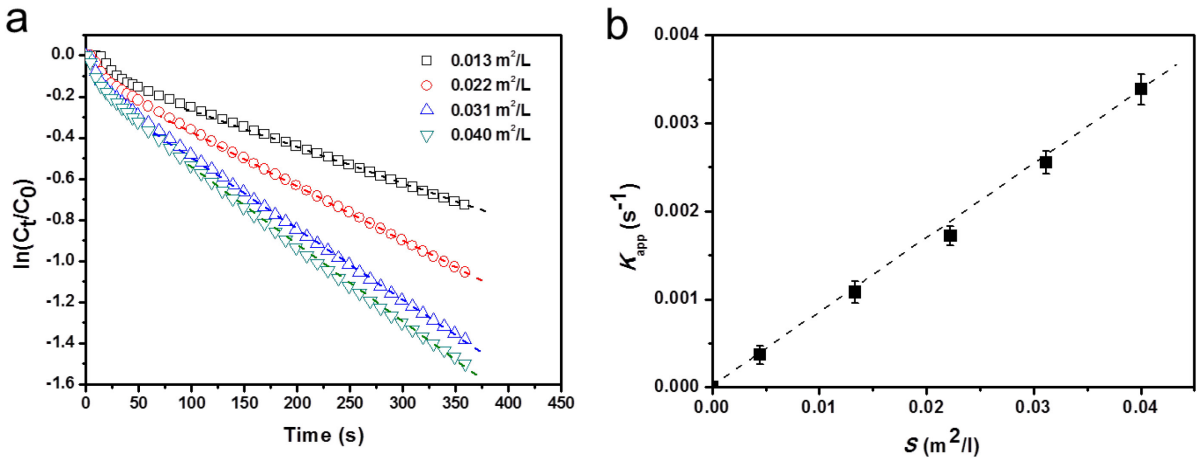

Figure 4.3.2 (a) The dependence of ln(c_t/c_0) on the reaction time for the reactions catalyzed by 0.013 m^2/L, 0.022 m^2/L, 0.031 m^2/L, and 0.040 m^2/L G-PDA-Au-1 particles, respectively. (b) Rate constant k_{app} as a function of surface area S of Au nanoparticles on G-PDA-Au-1 particles normalized to the unit volume of the system.

An additional comparison about the catalytic activity has been made between the present G-PDA-Au-1 nanocomposites and other reported catalyst systems for the reduction of Nip (Table 4.3.1). Here the surface area-normalized rate constant, k_1, is applied for direct comparison in order to exclude the influence of particle size. In general, G-PDA-Au-1 nanocomposites show quite high catalytic activity, which is comparable with the ligand free Au nanoparticles with similar size.[207] Comparing with ligand-stabilized Au nanoparticles, such as CTAB-Au,[206] and HS-PEG200-Au,[208] the G-PDA-Au-1 nanocomposites show much higher catalytic activity. Furthermore, comparing with graphene oxide (GO)-supported Au nanoparticles, such as Au nanoparticles deposited on tannic acid (TA)-functionalized graphene oxide (GO)[209] or AuNPs/TWEEN/GO,[210] the present catalyst system also shows better results. This may be due to the reason that π-rich Nip prefers to adsorb onto the PDA shell via π-π stacking interactions. The π-π interaction between Nip and PDA will increase the local concentration of Nip on the PDA shell, which enhances the catalytic activity of the Au nanoparticles. In addition, the Au nanoparticles on the G-PDA-Au nanocomposites are synthesized in situ without any stabilizer or surfactant. Therefore the unsaturated surface atoms of Au nanoparticles may coordinate in a better manner and adsorb Nip,[211] thus speeding up the reaction.

Table 4.3.1 Catalytic activity of the different reported catalyst systems based on Au nanoparticles for the reduction reaction of Nip.

Sample	Carrier System	d_{Au} (nm)	k_1[a] ($s^{-1}\cdot m^{-2}\cdot L$)
This work (G-PDA-Au-1)	Polydopamine	11.7	0.080
Jia[206]	CTAB-Au	10.9	8×10^{-3}
Ciganda[208]	HS-PEG2000	13.5	3×10^{-3}
Lu[210]	TWEEN-GO	10.7	3.4×10^{-4}
Zhang[209]	TA-GO	20	1.1×10^{-2}
Gu[207]	Ligand-free	11.1	0.17

[a] k_1: apparent rate constant normalized to the surface of Au nanoparticles in the system.

The influence of the amount of Au nanoparticles on the catalytic activity of the composite particles has been also studied. Two additional samples synthesized with 0.25 mM $HAuCl_4$ for 8 min (G-PDA-Au-2) and 0.1 mM $HAuCl_4$ for 0.5 min (G-PDA-Au-3) have been tested. Figure 4.3.3 shows again the linear relationship between apparent rate constant k_{app} and the

specific surface area of G-PDA-Au nanocomposites. k_1 can be obtained from the linear fit. Table 4.3.2 summarizes the catalytic activity of the G-PDA-Au nanocomposites prepared under different reaction conditions for the reduction of 4-nitrophenol. From Table 4.3.2, it can be observed that the composite particles with higher Au loading amount show higher apparent rate constant for the reduction of Nip, which is due to the increase of the Au catalysts in the system. But no marked difference has been found for the normalized rate constants k_1 for the composite particles with different Au loading.

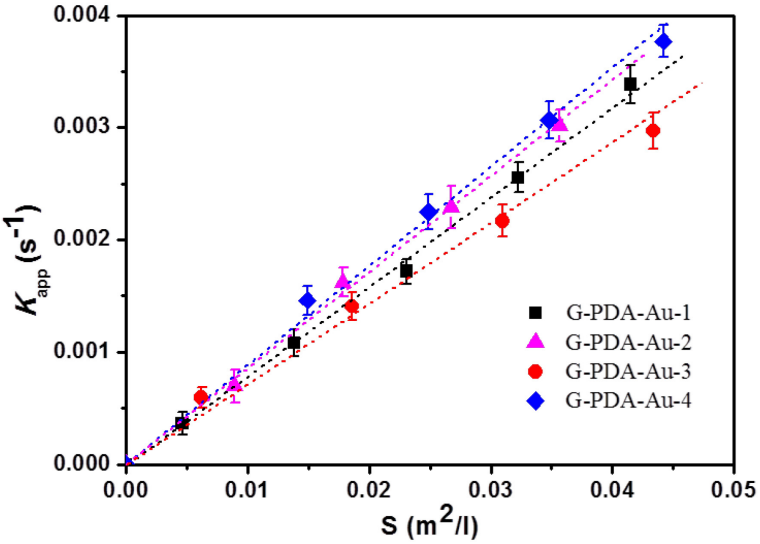

Figure 4.3.3 Rate constant k_{app} as a function of surface area S of Au nanoparticles on G-PDA-Au nanocomposites normalized to the unit volume of the system.

Table 4.3.2 Catalytic activity of G-PDA-Au nanocomposites prepared under different reaction conditions for the reduction reaction of Nip.

Sample	PDA thickness (nm)	c_{HAuCl4} (mM)	Reaction time (min)	Au loading (wt%)	d_{Au} (nm)	k_{app}[a] ($\times 10^{-3}$ s^{-1})	k_1[b] ($s^{-1}\cdot m^{-2}\cdot L$)
G-PDA-Au-1	14	0.1	4	13.97	11.7 ± 3.6	1.17	0.080
G-PDA-Au-2	14	0.25	8	39.10	29.1 ± 9.2	2.10	0.085
G-PDA-Au-3	14	0.1	0.5	7.38	11.1 ± 3.2	0.59	0.074
G-PDA-Au-4	8	0.1	4	15.14	10.4 ± 4.4	1.46	0.087

[a] k_{app}: apparent rate constant obtained by addition of 13.5 µg of the core particles.

[b] k_1: Rate constant normalized to the surface of the Au nanoparticles in the system.

In addition, in order to investigate the effect of the thickness of the PDA coating on the catalytic activity, G-PDA-Au-4 nanocomposites (Figure 4.3.4a) with thinner PDA thickness

(8 nm) have been synthesized under ultrasonification for 4 min in 0.1 mM $HAuCl_4$. The average size of Au nanoparticles (Figure 4.3.4b) deposited on the PDA shell is 10.4 nm and the loading amount is 15.14 wt%. $k_1 = 0.087\ s^{-1}\cdot m^{-2}\cdot L$ is obtained from the linear fit (blue line) in Figure 4.3.3. As shown in Table 4.3.2, it is found that the thickness of PDA has almost no influence on the rate constant of the immobilized Au nanoparticles, which is similar to the results reported by Duan *et al.*[212] In general, the present plate-like G-PDA core-shell particles can act as efficient carrier systems for the immobilization of catalytically active Au nanoparticles.

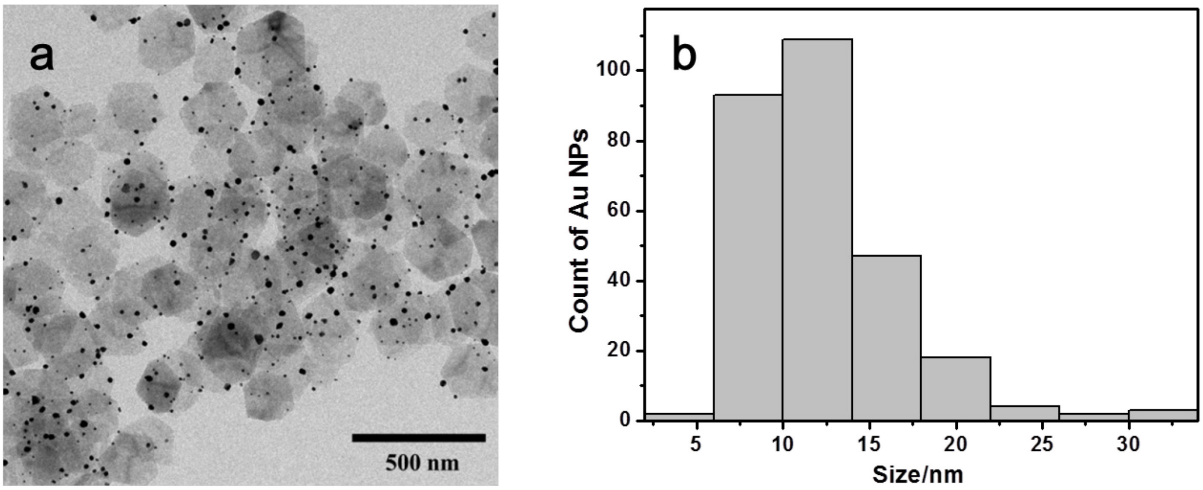

Figure 4.3.4 (a) TEM image of G-PDA-Au-4 nanocomposites under ultrasonification for 4 min in 0.1 mM $HAuCl_4$ aqueous solution and (b) its particle size distribution curves of Au nanoparticles on the G-PDA particles.

4.3.2 Catalytic activity evaluation for the reduction of Rodamine B

The reduction of RhB has been also selected as a model reaction to test the catalytic activity of the G-PDA-Au-1 nanocomposites. As reported,[213] without Au catalyst, the reduction of RhB will not proceed even with a large excess of $NaBH_4$. The kinetics of this reaction can be monitored by UV-Vis spectroscopy. Here, it is found that the reduction of RhB occurs immediately after G-PDA-Au-1 nanocomposites are added, as evidenced by the vanishing of the color. As shown in Figure 4.3.5a, after addition of G-PDA-Au-1 nanocomposites the characteristic absorption band of RhB at 554 nm decreases rapidly as the reaction proceeds. A first order kinetics with regard to the RhB concentrations could be used to evaluate the reaction rate. The induction period t_0 was related to a surface restructuring of the nanoparticles before the catalytic reaction starts.[151] From the subsequent slope of the

absorbance in Figure 4.3.5b (marked with blue), the apparent rate constant (k_{app}) can be obtained.

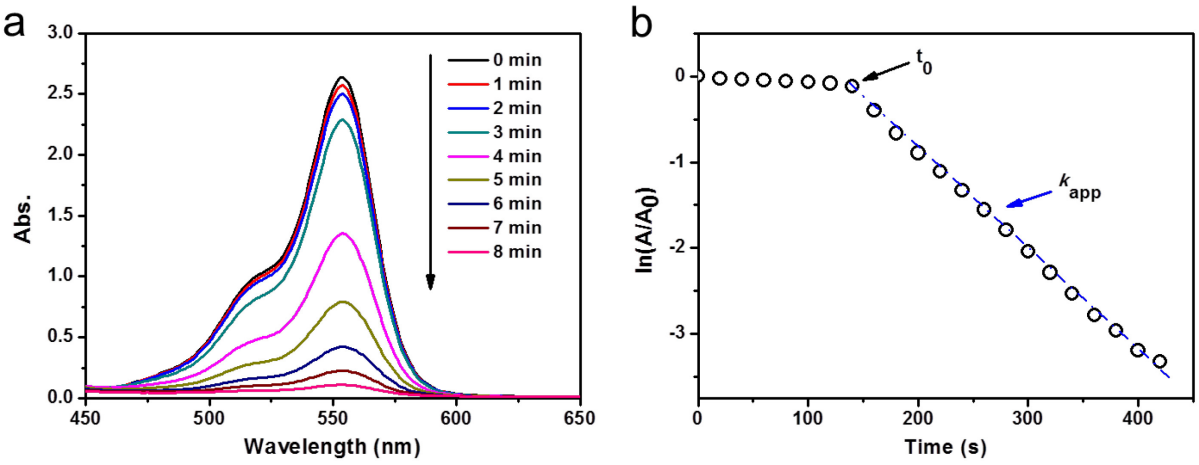

Figure 4.3.5 (a) UV-Vis absorption spectra of RhB during the reduction catalyzed by G-PDA-Au-1 nanocomposites at room temperature. (b) Typical time dependence of the absorption of RhB at 554 nm.

Similarly, a linear dependence of the apparent rate constant k_{app} on the total surface S of the Au nanoparticles has been observed as shown in Figure 4.3.6. The rate constant (k_1) of the G-PDA-Au-1 nanocomposites has been determined as 1.88 $s^{-1} \cdot m^{-2} \cdot L$.

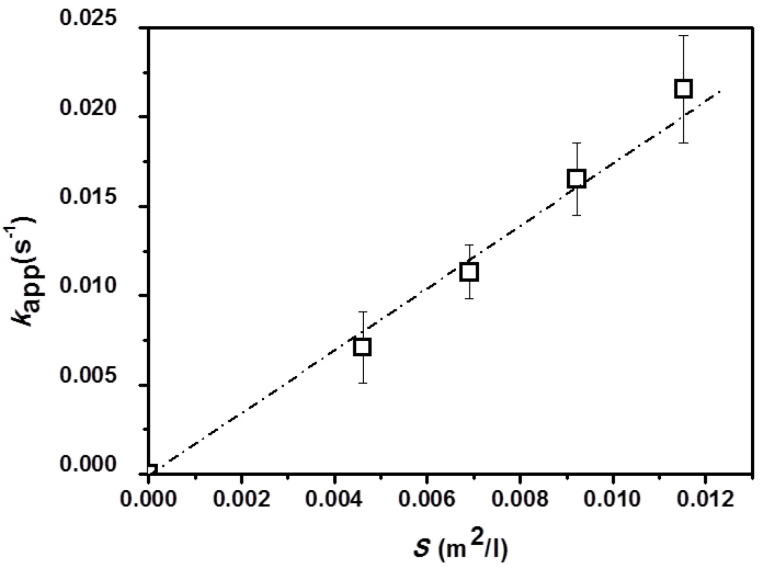

Figure 4.3.6 Rate constant k_{app} as a function of the surface area S of Au nanoparticles on G-PDA-Au-1 normalized to the unit volume of the system.

In addition, CTAB-stabilized Au nanoparticles (Figure 4.3.7a) with an average size of 14.8 nm have been synthesized and used for comparison. In the case of CTAB-stabilized Au nanoparticles used in this work, the apparent rate constant k_{app} has a linear dependence on the

surface of the Au nanoparticles as shown in Figure 4.3.7b. The surface normalized rate constant is k_1 = 0.12 $s^{-1} \cdot m^{-2} \cdot L$. Again, G-PDA-Au-1 nanocomposites show much higher catalytic activity than that of the CTAB-stabilized Au nanoparticles.

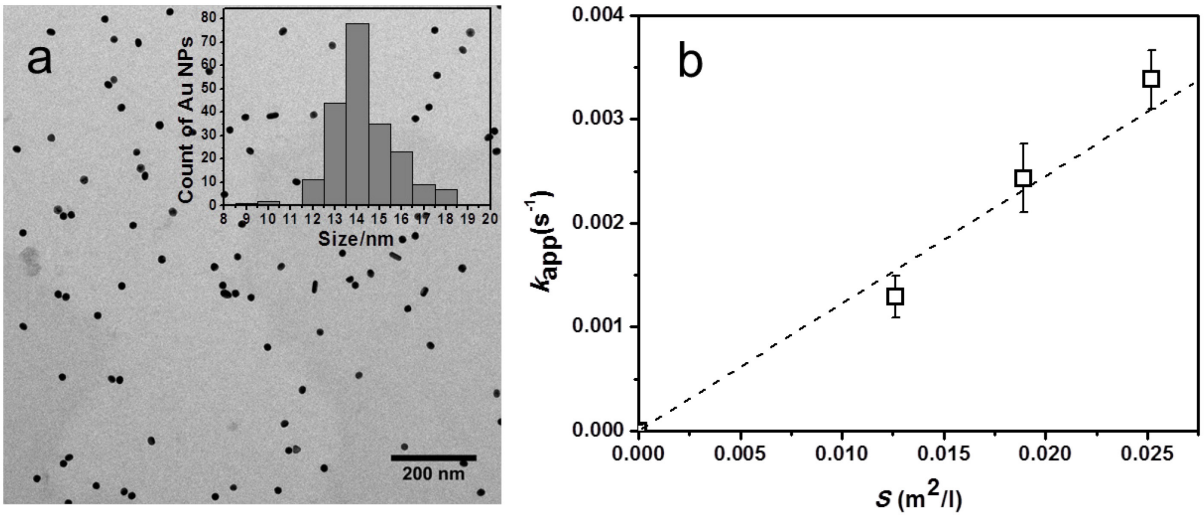

Figure 4.3.7 (a) The TEM image of CTAB-stabilized Au nanoparticles and its size distribution curve. (b) Rate constant k_{app} as a function of the surface area S of CTAB-stabilized Au nanoparticles normalized to the unit volume of the system.

4.3.3 Fabrication of the substrate-deposited nanocatalysts and recyclability test

Effective separation and easy recycling of the tiny catalysts remain a technological challenge. To solve the separation problem, one of the most common methods is to use magnetic materials as the solid matrix to support Au nanocatalysts. Several studies have been reported on the synthesis and application of magnetic materials (*e.g.*, β-FeOOH and Fe_3O_4) supported Au nanocatalysts.[214,215] The nanocatalysts can be recovered and recycled through a convenient magnetic separation process. An alternate strategy is immobilization of nanocatalysts on the substrate by physical binding. Zhou *et al.* developed recyclable nanocatalysts by interfacially assembling spherical Au@Ag@PDA nanoparticles on the solid substrate due to PDA's strong adhesion properties.[58] Although these recyclable nanocatalysts show relatively high catalytic activity and recyclability, the synthesis/self-assembly procedures are somewhat complicated and toxic reagents/solvents are involved. Therefore, development of a simple and low toxic approach to synthesize recyclable nanocatalysts has become crucial.

The mussel-inspired PDA molecules are well-known for their strong adhesion to nearly all types of inorganic and organic substrates,[216,217] which facilitates robust binding of the PDA

supported G-PDA-Au nanocomposites onto solid substrates. In addition, plate-like G-PDA-Au particles have larger contact area with substrate compared to that of spherical particles. Thus, the G-PDA-Au nanocomposites can be well immobilized on the silicon substrate by spin coating. As shown in Figure 4.3.8a, a homogeneous monolayer of the G-PDA-Au particles is formed on the silicon substrate with high surface coverage, which is beneficial for the catalysis.

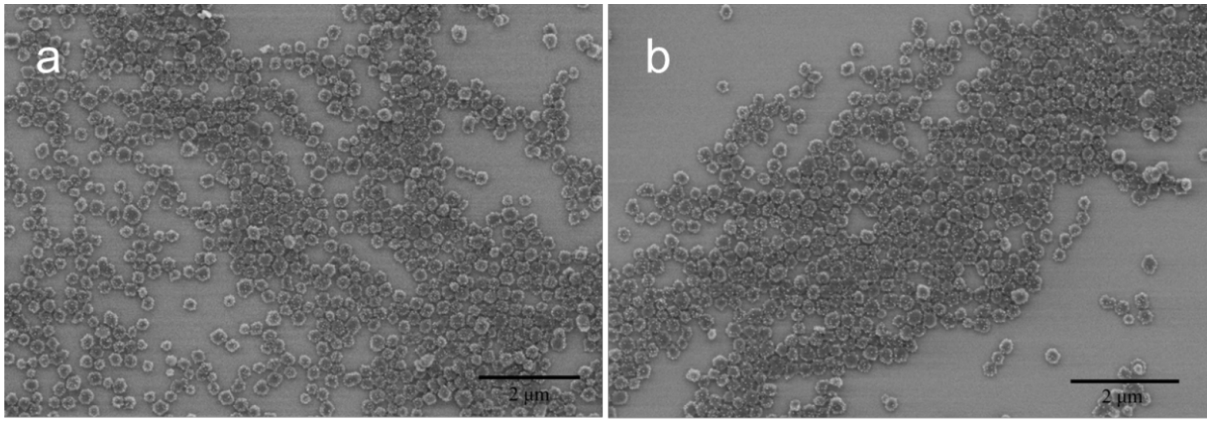

Figure 4.3.8 SEM images of the G-PDA-Au particles monolayers on silicon substrate (a) before and (b) after catalysis.

In our study, the reduction of RhB is used to test the catalytic recyclability of the substrate-deposited G-PDA-Au nanocatalysts. The reusability of the supported catalysts was measured by repeating the catalytic reaction for 90 min for each run. Between each cycle, the supported catalyst is separated from the reaction mixture, rinsed with distilled water, and dried at room temperature. As shown in Figure 4.3.9, the catalysts show almost identical activities in five successive cycles without decreasing of the conversion. Extending the reaction time from 90 min to 150 min, 100% conversion efficiency can be achieved. Moreover, there is nearly no evident detachment of the coating layer from the substrates after catalysis (Figure 4.3.8b), which is resulted from the strong adhesion of the PDA layer. This is highly important for the consistent catalytic performance.

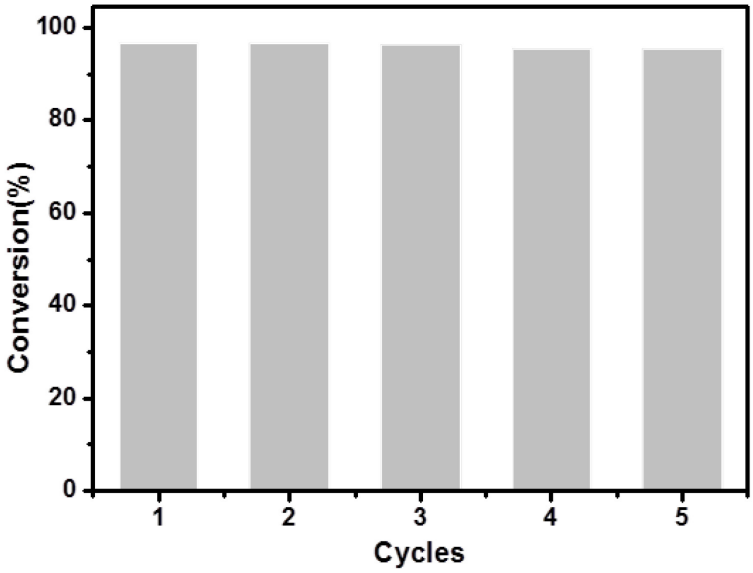

Figure 4.3.9 Conversion efficiency for the reduction of RhB using G-PDA-Au composite particles as catalyst in 90 min reaction in 5 consecutive reaction cycles.

In conclusion, the G-PDA-Au nanocomposites show high catalytic activity in the reduction of Nip and RhB. The influence of the number and size of Au nanoparticles on the catalytic activity have been investigated. The catalytic study indicates that the G-PDA-Au nanocomposites with larger amount of Au show higher apparent rate constant for the reduction of Nip, which is due to the increase of Au catalyst amount in the system. But no big difference has been found for the normalized rate constants k_1 for the composite particles with different amount of Au. Furthermore, the influence of the thickness of the PDA shell on the catalysis has also been studied. It is observed that both k_{app} and k_1 for the G-PDA-Au with thinner PDA shell (8 nm) are similar as that of G-PDA-Au with thicker PDA shell (14 nm) for the reduction of Nip, indicating that PDA thickness shows almost no influence on the catalytic activity.

In addition, due to the strong adhesive behavior of PDA and large contact area of plate-like G-PDA-Au particles with substrate, the substrate-immobilized G-PDA-Au nanocatalysts have been successfully obtained by spin-coating the G-PDA-Au nanocomposites onto the silicon substrate. The substrate-deposited G-PDA-Au nanocatalysts show excellent catalytic recyclability in the reduction of RhB. SEM measurements indicate that there is nearly no change on the surface coverage before and after catalysis. This simple, low-cost and low-toxic approach might be extended for the preparation of other recyclable nanocatalysts for practical application in the field of organic pollutant degradation.

5. Thermo-responsive core-shell hybrid microgels based on anisotropic plate-like nanoparticles

Anisotropic colloidal particles have received considerable attention in a wide range of scientific fields including electronics, energy, and nanotechnology.[10] Their self-assembly and phase behaviors have been investigated theoretically and experimentally for rod-like, dumbbell-like, disc-like, ellipsoidal, and cubic particles.[218–220] Despite the increasing number of approaches on the synthesis of well-defined non-spherical colloidal particles with a broader range of shapes, attempts to synthesize responsive anisotropic particles are still sparse.

Microgel particles have attracted growing interest over the years owing to their tunable and stimuli-responsive properties.[221–223] These systems are responsive to external stimuli, such as pH, ionic strength, light, and temperature, leading to variations in the properties like dimensions, structure, and interactions.[224–227] In particular, microgels composed of N-isopropylacrylamide (NIPAm) crosslinked with N,N'-Methylenebisacrylamide (BIS) have been established as a model system for a comprehensive investigation of the structure, dynamics, and flow behavior of the concentrated suspensions.[87,228,229] Size, degree of softness, swelling ratio, and hydrophobicity of the PNIPAm microgel particles can be controlled by a temperature induced volume phase transition.[114–116]

So far, hybrid microgels with core-shell structures have been prepared by using organic/inorganic particles, *e.g.* polystyrene, gold and silica, as core.[230–232] Often, spherical hybrid microgels are obtained.[87] Attempts to synthesize anisotropic hybrid microgels are still rare. Only few examples of anisotropic hybrid microgels which constitute model systems with a rich orientational and positional ordering behavior have been achieved.[89,233] For example, monodisperse thermosensitive dumbbell-shaped core-shell microgels have been reported, which serve as model systems to investigate the phase behavior and the crystallization.[89] Dagallier *et al.* reported the synthesis of hybrid magnetic microgel particles with an embedded ellipsoidal hematite (α-Fe_2O_3) core, and investigated the rotational behavior of these hybrid microgel particles due to the ellipsoidal shape of the cores.[233] Challenges remain in the synthesis of relevant quantities of anisotropic hybrid microgel particles with low size polydispersity, and no attempts have been made for plate-like core geometries so far.

In this chapter, well-defined core-shell thermosensitive plate-like microgel particles with controllable shell thickness by using gibbsite platelet as template have been synthesized. Comprehensive characterizations including Transmission Electron Microscopy (TEM), cryo-TEM, Field-Emission Scanning Electron Microscopy (FE-SEM), Atomic Force Microscopy (AFM), and Depolarized Dynamic Light Scattering (DDLS) have been performed. Special emphasis is put on the morphology and thermosensitivity of the as-obtained hybrid microgels.

5.1 Synthesis and functionalization of silica coated gibbsite platelets

It is difficult to conduct the polymerization on the surface of the gibbsite platelets directly for the synthesis of hybrid microgels because of lacking an appropriate interaction between the gibbsite platelets and the monomer. Coating the gibbsite platelets with a silica layer meets such requirement. Reactive hydroxyl groups on the surface of silica layer enable the gibbsite/SiO_2 composites to be well dispersed in ethanol. Thus, silica coated gibbsite platelets can act as template for the further-stage polymerization. The silica coated gibbsite platelets used in this work have been prepared in two steps. Figure 5.1.1 displays the synthesis routine in a schematic fashion. Firstly, plate-like gibbsite nanoparticles are coated with a layer of silica shell by using a modified Stöber method with the aid of the amphiphilic poly(vinylpyrrolidone) (PVP).[104] In a second step, silica coated gibbsite platelets (GS) is functionalized with coupling agent 3-(trimethoxysilyl)propyl methacrylate (MPS) according to the method reported by Liz-Marzán and Hellweg *et al.*[86]

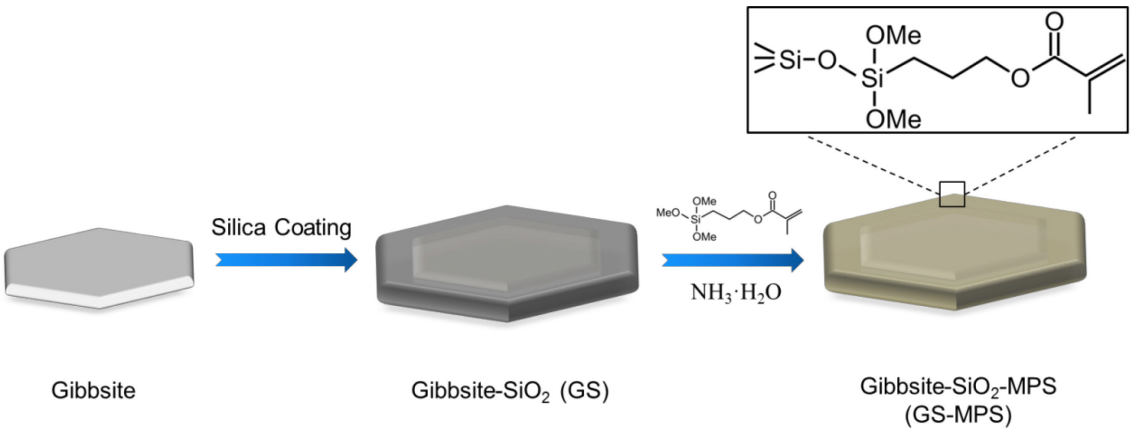

Figure 5.1.1 Schematic presentation of the synthesis and functionalization of silica coated gibbsite platelets.

In a Stöber synthesis, silica is grown in a mixture of ethanol, ammonia and water, to which tetraethoxysilane (TEOS) is added. Smooth silica layers can be produced by using this

method, and the thickness of silica layers can be well controlled by the amount of TEOS. If the particles are not stable in the Stöber mixture, the particle surface needs to be firstly modified by sodium silicate solution,[234] PVP[109] or (3-aminopropyl)trimethoxysilane (APTES).[235] Since gibbsite is not stable in ethanol, surface modification is thus required. Here, the gibbsite particles have been first modified with amphiphilic PVP, which enables the affinity of the gibbsite surface to silica. Zeta-potential of the particles converts from 40.3 mV to –19.2 mV, indicating the successful deposition of PVP on the gibbsite surface. Silica coating is then conducted by adding PVP-modified gibbsite particles into the Stöber mixture.

In order to investigate the influence of the ammonia concentration on the silica coating, several ammonia concentrations have been applied. As can be seen from Figure 5.1.2a, the corners of the silica coated gibbsite particles (GS) are less sharp compared with pure gibbsite particles. However, numerous secondary silica particles have been formed when an ammonia concentration of 4% *v*/*v* is used. Figure 5.1.2b shows two standing particles at higher magnification. The silica shell is clearly visible, which has been indicated with blue arrows. The silica layer is measured to be about 16 nm, which is thinner than expected, because a big part of the TEOS is grown into secondary silica particles in the solution.

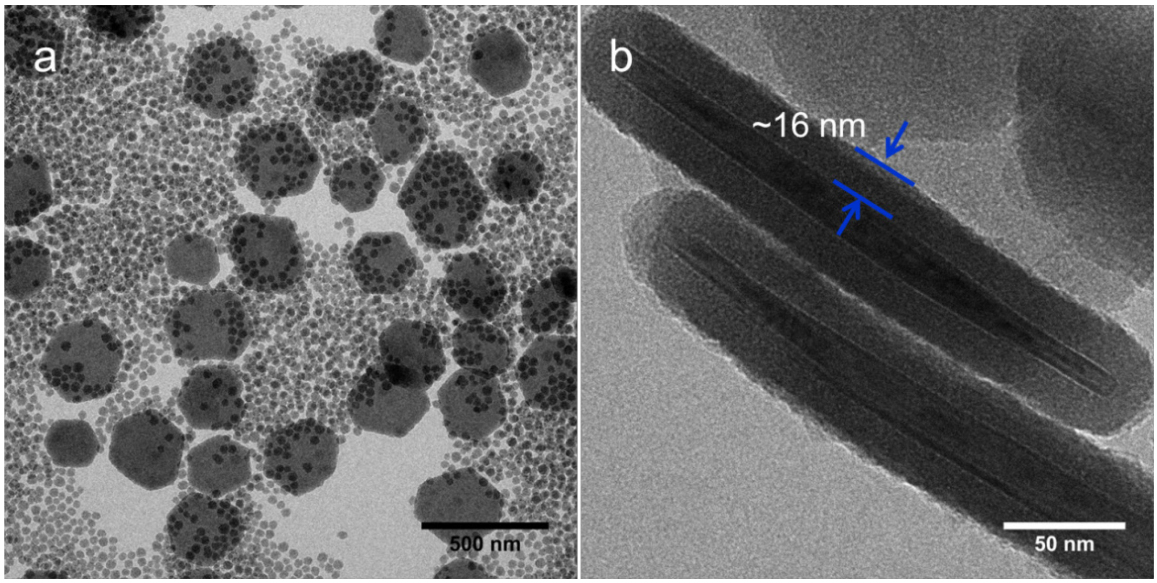

Figure 5.1.2 (a) TEM image of GS nanoparticles synthesized by using 4% *v*/*v* ammonia. Numerous silica particles are nucleated in the solution. (b) TEM image of the standing GS nanoparticles. The blue arrows point to the silica layer (~16 nm).

It is known that the second nucleation in growing silica layers around silica spheres can be suppressed by a higher ammonia concentration.[236] By increasing the concentration of

ammonia from 4% to 7%, no secondary silica particles can be found in the sample as shown in Figure 5.1.3a. However, higher concentration of ammonia leads to the formation of aggregates, although a lot of nicely silica coated particles can be seen in this sample. Figure 5.1.3b shows two aggregated gibbsite particles covered and joined with silica indicated by a white arrow. The silica layer is around 25 nm, which is indicated by blue arrows.

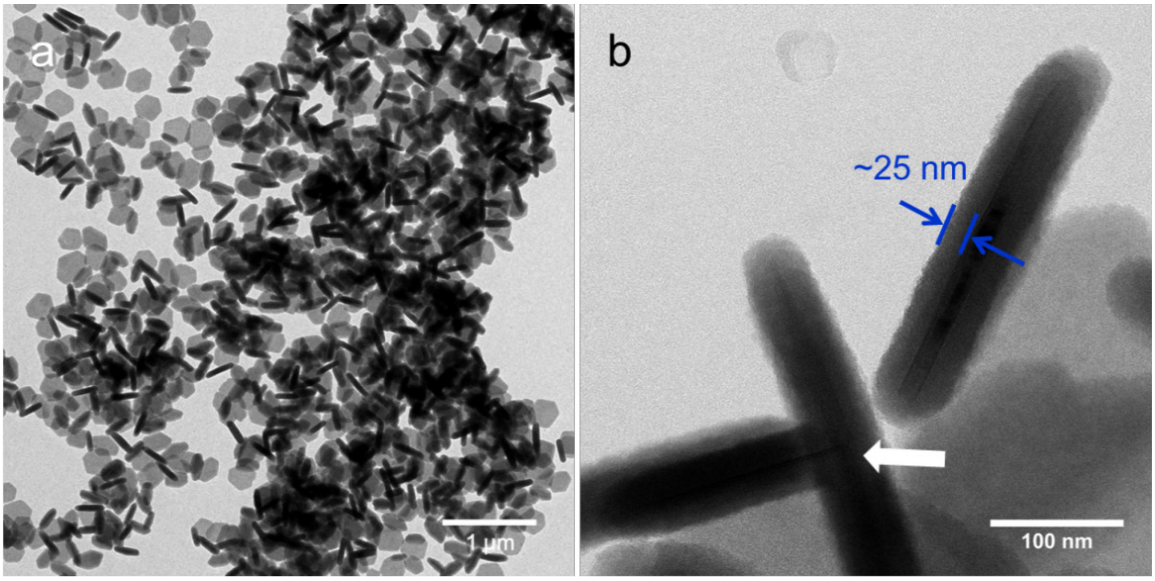

Figure 5.1.3 (a) TEM image of GS nanoparticles synthesized by using 7% *v*/*v* ammonia. (b) TEM image of the standing GS nanoparticles. The white arrow points to two aggregated gibbsite platelets covered and joined with silica. The blue arrows point to the silica layer (~25 nm).

Figure 5.1.4a gives an overview of GS particles synthesized with 5.5% *v*/*v* of ammonia. Neither secondary silica particles nor aggregates can be observed after silica coating. Some particles can easily stand on their sides indicated by red arrows. The aspect ratio (diameter/thickness) of the particles is around 4.2, which is about 25 before silica coating. At some parts of the image, the concentration of particles is quite high. Particles are lying on the top of each other. They are still single particles, not aggregates. The inset in Figure 5.1.4a shows a single GS particle at higher magnification. The whole particle is evenly coated with a smooth silica layer which is around 25 nm. The average equivalent circular diameter of 245 nm (σ_{ECD} = 46 nm) has been obtained by measuring the surface area of over 200 individual hexagonal particles (Figure 5.1.4b).

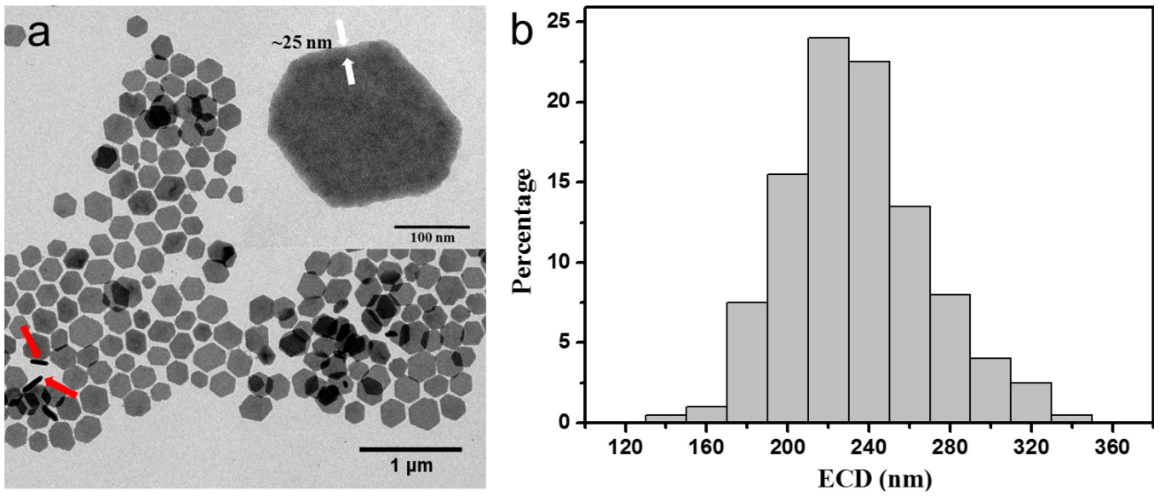

Figure 5.1.4 (a) TEM image of gibbsite particles coated with silica. No secondary silica particles or aggregates are produced by using 5.5% *v*/*v* of ammonia. The red arrows point to the standing particles. (b) Scatter diagram of the equivalent circular diameter (ECD) of the GS particle as determined from transmission micrographs, average size is 245 ± 46 nm.

The presence of the silica layer cannot be proved by X-ray diffraction due to the amorphous phase of the silica shell. Therefore, EDX is used to prove the presence of silica. As shown in Figure 5.1.5, the EDX spectrum of the silica-coated gibbsite particles shows that the signals of Al, O and Si are detected, indicating the successful modification of silica shell on the gibbsite nanoparticles.

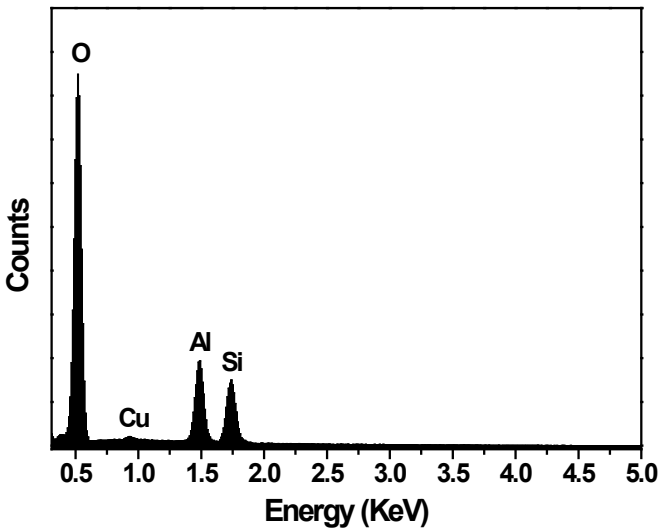

Figure 5.1.5 EDX spectrum of GS nanoparticles. Cu signal derives from the Cu foil substrate.

In the second step, narrow-disperse MPS-modified GS nanoparticles have been prepared by the hydrolysis of MPS via self-condensation reaction between the hydroxyl groups of silica shell to provide the reactive vinyl groups for further-stage polymerization. The core-shell structure of the particles has been well maintained after MPS modification. No aggregates can be observed from Figure 5.1.6a. The silica-MPS shell has thickness of 25 nm which is similar as that of silica shell without MPS modification (Figure 5.1.6b).

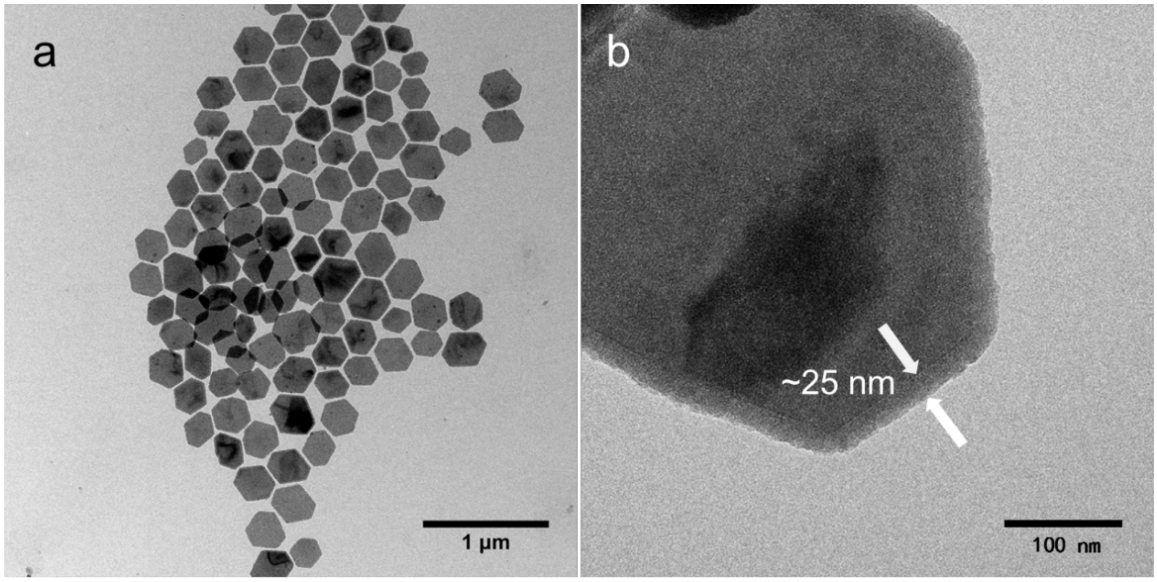

Figure 5.1.6 (a) TEM image of MPS modified GS particles. No aggregates can be found after MPS modification. (b) TEM image of a single GS-MPS particle at higher magnification. The white arrows point to the silica layer (~25 nm).

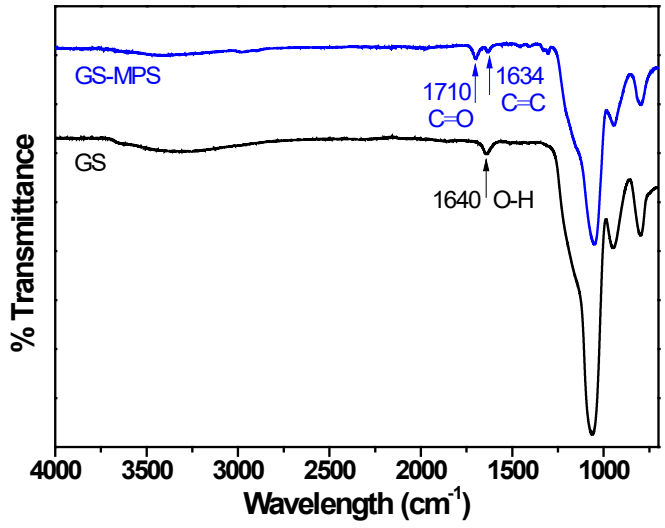

Figure 5.1.7 FT-IR spectra of GS and GS-MPS particles.

The successful functionalization of carbon–carbon double bonds on the GS surface has been confirmed by FT-IR spectra as shown in Figure 5.1.7. The peak at 1642 cm^{-1} is due to the O-H bending vibrations of the adsorbed molecular water. The bands at 1634 and 1710 cm^{-1} are attributed to the stretching vibrations of the vinyl and carbonyl groups of MPS component, respectively.[237]

In conclusion, monodisperse silica coated gibbsite particles with an average size of 245 nm have been successfully obtained by using the modified Stöber method. By adding proper amount of ammonia, aggregation and second nucleation of silica can be effectively avoided. The as-synthesized core-shell GS particles are stable in ethanol and have the same surface properties as pure silica particles. MPS is then modified on the surface of GS particles to incorporate the reactive vinyl groups, which has been proved by FT-IR measurements.

5.2 Synthesis and characterization of GS-MPS-PNIPAm microgels

MPS-modified GS particles with vinyl groups on the surface have been used as seeds in the emulsion polymerization for the synthesis of the cross-linked PNIPAm shell. The coupling agent MPS generates a hydrophobic surface on the silica particles and can afterwards react in the radical polymerization allowing for the chemical coupling between the PNIPAm network and the inorganic core. A shell of PNIPAm cross-linked by N,N'-Methylenebisacrylamide (BIS) is then grafted onto the core particles via seeded emulsion polymerization as shown in Figure 5.2.1.[238] In order to improve the stability of the GS-MPS particles, PVP has been used as stabilizer during the polymerization.

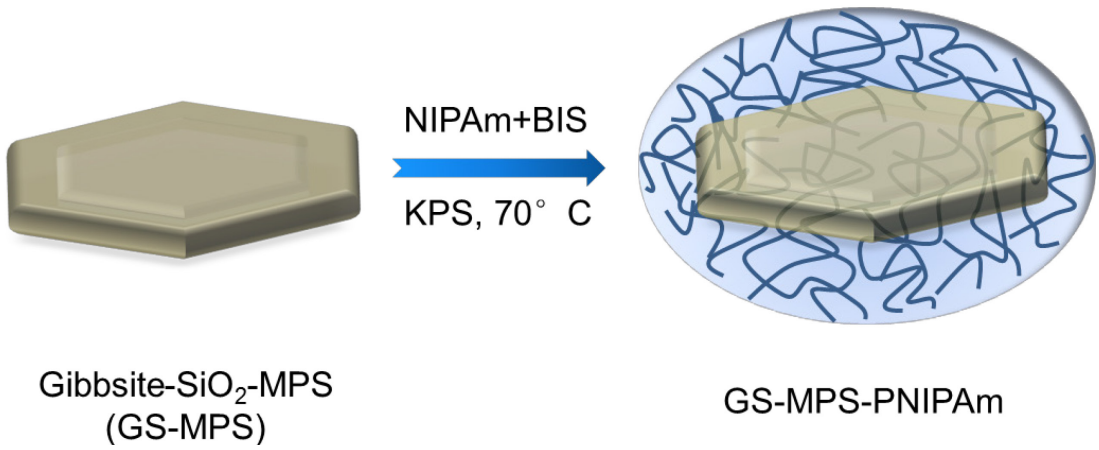

Figure 5.2.1 Schematic presentation of the synthesis of thermo-responsive hybrid microgels.

An analysis of the dilute suspension of the as-synthesized particles by zeta-sizer shows that zeta-potential of the GS-MPS-PNIPAm microgels is −17 mV at 25 ºC and −34 mV at 45 ºC, respectively. This effect has been already observed in previous studies of the PNIPAm particles, which is due to the residual charges originating from the synthesis of these particles.[239,240,241] The charge of the GS-MPS particles will be preserved when polymerizing the shell onto these cores, and result in the observed electrophoretic mobility. The charges of the core particles are very important, which provide sufficient stabilization even at high temperatures during the polymerization process in which the PNIPAm shell is affixed to the core.[242]

GS-MPS-PNIPAm core-shell microgels with different PNIPAm thickness have been prepared with high yields of particles containing a single nanoparticle core. The size, shape and polydispersity of the hybrid microgel particles have been investigated by using different methods. The formation of PNIPAm shell on the surface of GS-MPS particle has been first confirmed from TEM images as shown in Figure 5.2.2. Microgel dispersions are stable for a few weeks and no secondary PNIPAm particles can be found in the TEM images after washing procedure. Due to the difference in electron density between the GS-MPS core particles and the surrounding PNIPAm network, the core-shell structure of the hybrid microgels can be clearly observed. The GS-MPS cores are incorporated in the center of the PNIPAm network and each hybrid microgel with a single core is found. When 0.077 M of NIPAm monomer is used, PNIPAm shell with thickness about 260 nm can be observed from the TEM image shown in Figure 5.2.2b, which is homogenously coated on the GS-MPS surface. The gibbsite core, silica layer and PNIPAm shell are indicated by black, blue and red arrow, respectively. Decreasing of the NIPAm monomer concentration in the polymerization leads to the decrease of the thickness of PNIPAm shell as seen from the TEM image of the particles (Figure 5.2.2d). The PNIPAm shell is around 175 nm when 0.062 M NIPAm monomer is used. This has been also confirmed by DLS measurements that the hydrodynamic diameter of the microgel particles decreases with the decrease of the NIPAm concentration as shown in Figure 5.2.3. Decreasing NIPAm monomer amount to 0.049 M, GS-MPS-PNIPAm microgel with a thin PNIPAm layer of about 90 nm is obtained (Figure 5.2.2f). As a reference, polymerization of NIPAm has been also conducted by using GS particles without MPS modification as seeds, agglomeration is formed in this case and the system is unstable. This proves that the vinyl group on the GS particle surface is essential for the grafting of polymer onto silica.

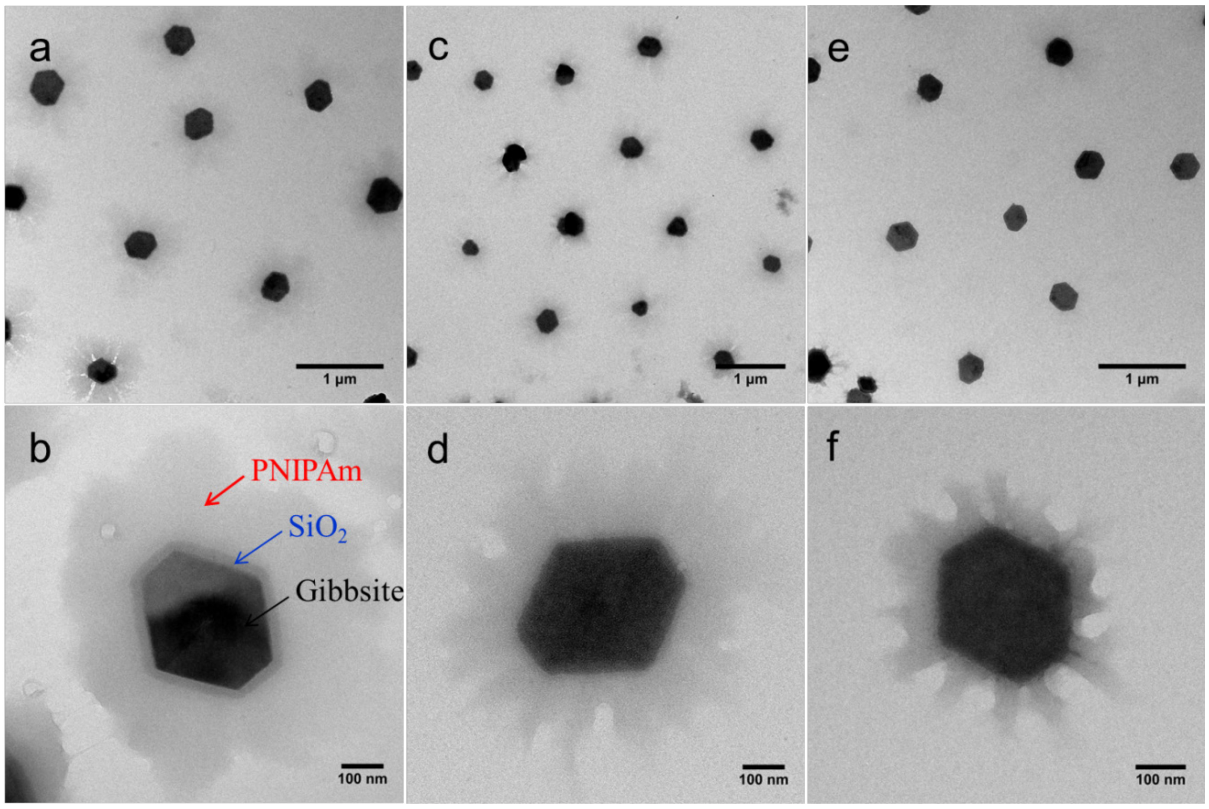

Figure 5.2.2 TEM images of the GS-MPS-PNIPAm trilayer microgels synthesized with different NIPAm monomer concentrations (a, b) 0.077 M, (c, d) 0.062 M, and (e, f) 0.049 M, during polymerization.

The thermosensitive properties of the GS-MPS-PNIPAm particles have been investigated by DLS measurements as a function of temperature. Figure 5.2.3 shows the variation of the hydrodynamic radius (R_h) of the core-shell microgels prepared with different NIPAm dosages when the temperature is varied from 20 to 50 ºC. With increasing the dosage of NIPAm, the R_h of the particles increases. Taking at 20 °C for example, the R_h of the core-shell microgels prepared with 0.077 M, 0.062 M and 0.049 M of NIPAm dosages at this temperature are 463, 362 and 240 nm, respectively. Considering the R_h of the GS-MPS core at 20 °C is 124 nm by DLS, the thickness of the PNIPAm shell is about 339, 238 and 116 nm, respectively. Moreover, there is a strong change in size induced by the change of the temperature. The well-defined volume transition temperature of the hybrid microgels is found to be around 32 ºC, which exhibits a similar swelling behavior as pure PNIPAm microgels. In addition, the transition is fully reversible under the heating-cooling circles. This indicates that the presence of GS-MPS template does not significantly affect the swelling-deswelling behavior of the PNIPAm shell. As a reference, without PNIPAm shell, the R_h of GS-MPS core keeps constant as a function of temperature. This proves that the thermosensitive properties of the hybrid microgels result from the PNIPAm shell.

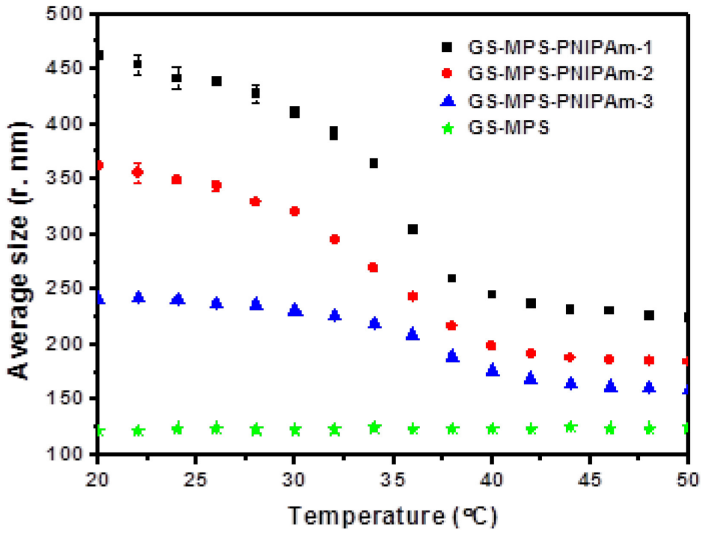

Figure 5.2.3 Hydrodynamic radius of the GS-MPS-PNIPAm particles as a function of temperature. GS-MPS-PNIPAm-1, GS-MPS-PNIPAm-2, and GS-MPS-PNIPAm-3 are the hybrid microgel particles prepared with different NIPAm monomer concentrations (black square) 0.077 M, (red circle) 0.062 M, and (blue triangle) 0.049 M, respectively. And hydrodynamic radius of the GS-MPS core particles (green star) as a function of temperature.

Figure 5.2.4 shows SEM images of the as-prepared core-shell microgels in the dried state by dropping a diluted aqueous solution onto silicon wafer. A homogeneous monolayer of GS-MPS-PNIPAm particles can be then obtained after drying. Most of the as-prepared hybrid microgels have a single plate-like core of GS-MPS. Due to the polymeric shell, the GS-MPS cores are well separated with inter-particle distances in the order of ~1 μm.

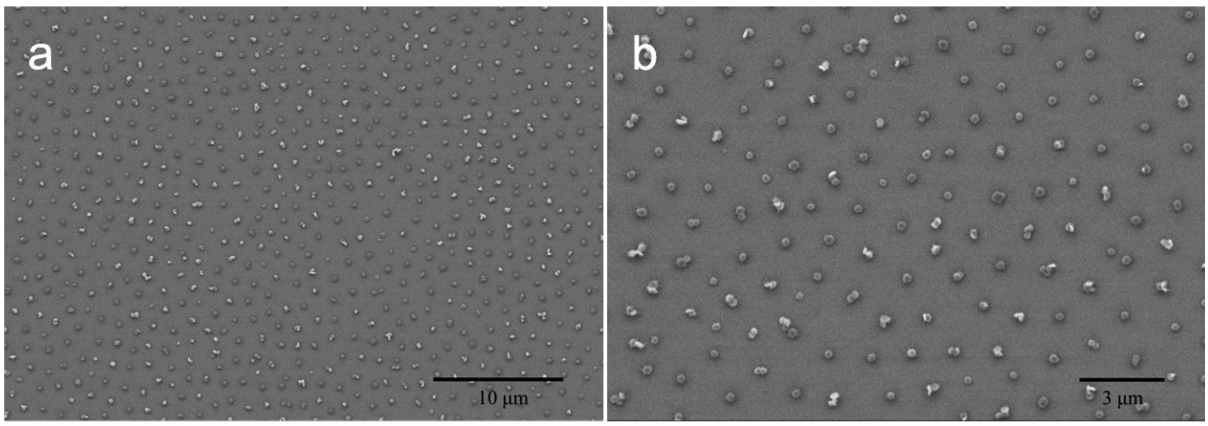

Figure 5.2.4 SEM images of the GS-MPS-PNIPAm trilayer microgels dried on a silicon substrate.

Recently, cryo-TEM has been demonstrated as a suitable method for the study of thermosensitive microgel particles.[243] Cryo-TEM measurements have been performed by vitrifying the GS-MPS-PNIPAm microgels synthesized with 0.062 M NIPAm in water to investigate the morphology of the hybrid microgels in situ. The PNIPAm shell is in its swollen state as shown in Figure 5.2.5a. The images of the GS-MPS-PNIPAm microgels reveal that the core-shell particles are indeed narrowly distributed. Moreover, the silica mid-layer and the thermosensitive shell are clearly visible in Figure 5.2.5b. The cross-linked PNIPAm shell is homogeneously attached to the surface of their corresponding plate-like core particles. Note that no contrasting agent is used to enhance the contrast of any part of the particles. A much thicker PNIPAm shell of approximately 230 nm compared to the shell thickness from TEM images has been determined, which agrees well with the thickness of the PNIPAm shell determined by DLS at 20 ºC.

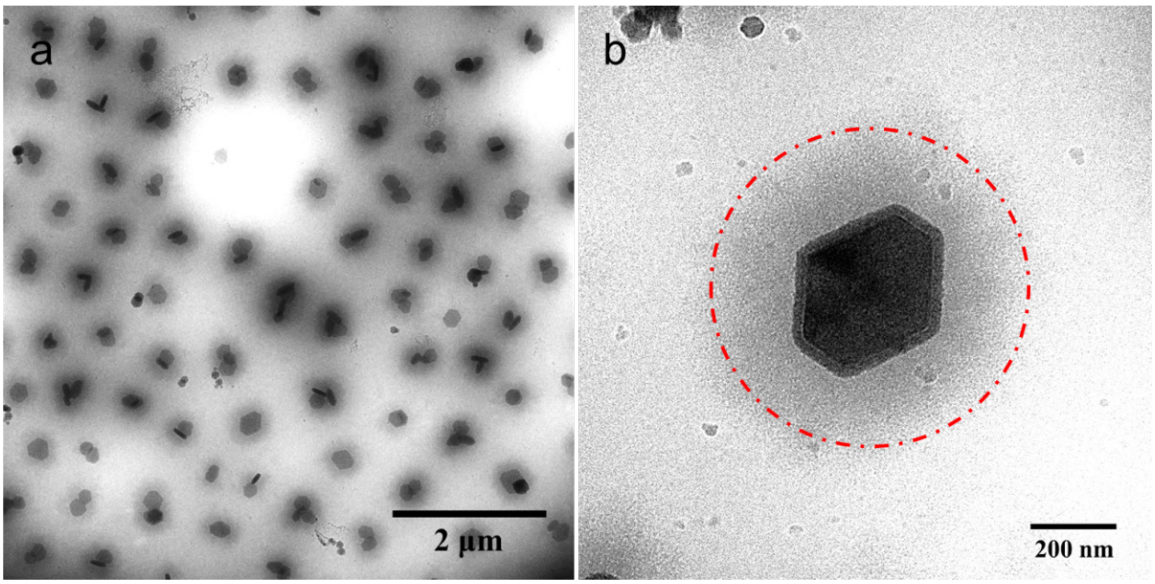

Figure 5.2.5 (a) Cryo-TEM micrographs of the thermosensitive GS-MPS-PNIPAm core-shell particles synthesized with 0.062 M NIPAm monomer in aqueous solution at room temperature. The samples were maintained at 20 ºC. (b) The dark core consists of GS-MPS, and the corona of PNIPAm cross-linked with BIS is indicated by dash line.

AFM has been also used to analyze the morphology of the obtained hybrid microgels. Due to the hard character of the core and the soft PNIPAm shell, AFM in tapping mode can detect the solid cores in-situ. However, because of the smearing effect of the fuzzy shell, an estimation for the core radius can only be obtained by AFM. In Figure 5.2.6a, the AFM image shows the GS-MPS-PNIPAm microgels form an array with spaces between them. This is similar to the spontaneously array of PNIPAm microgels and particles with PNIPAm chains

on the surface reported by Kawaguchi.[244] The self-assembly of GS-MPS-PNIPAm microgels is attributed to the capillary forces between the particles and exclusive effect of the PNIPAm shell. The cross-section analysis in Figure 5.2.6b shows a pronounced increase in the vertical dimensions and then a platform due to the plate-like morphology of the core, indicating that the particle stands out from its polymer surroundings. This is clearly different from spherical core-shell microgels.[245,246] The presented AFM analysis is in good agreement with the expected structure of these core-shell systems.

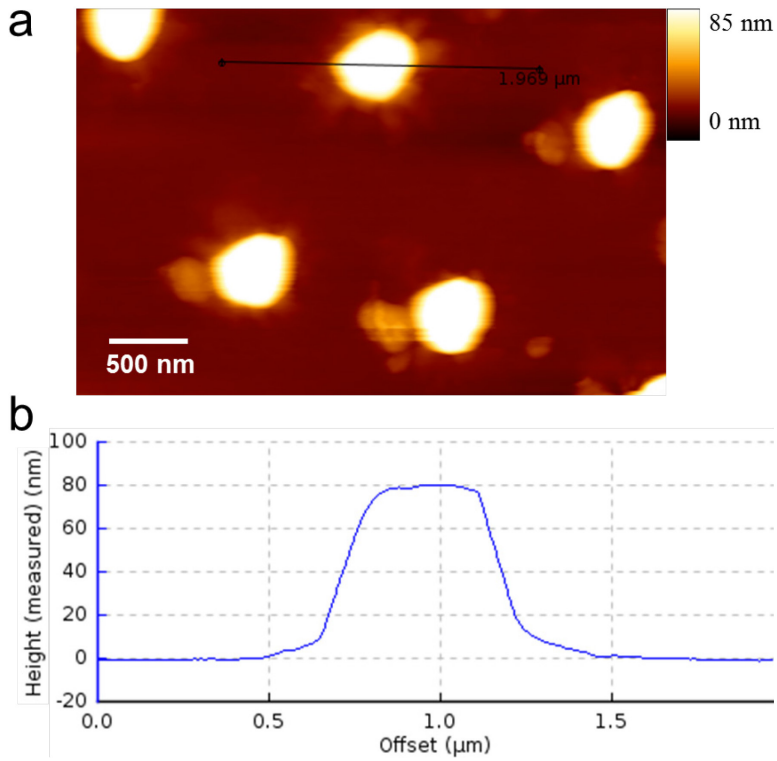

Figure 5.2.6 a) AFM height image of the GS-MPS-PNIPAm microgels synthesized with 0.062 M NIPAm monomer. b) the corresponding cross-section profile taken along the black line in a.

In the following, we discuss the results of the translational and rotational motion of the GS-MPS-PNIPAm particles by dynamic light scattering (DLS) and depolarized dynamic light scattering (DDLS). The scattering from optically anisotropic particles leads to a depolarization of the scattered light, allowing for the determination of their rotational diffusion coefficient (D^R) by DDLS. The size parameters of an anisotropic object can be calculated from the diffusion coefficients D^T and D^R for different geometries such as spheres, ellipsoids, rigid rods, and dumbbell-shaped particles.[91,247–249] Here we apply both DLS and DDLS to the GS-MPS-PNIPAm particles and interpret the experimental data in terms of a

slow (Γ_{slow}) and a fast relaxation mode (Γ_{fast}) of the measured intensity autocorrelation function (Figure 5.2.7a)[249]

$$\Gamma_{slow} = D^T \cdot q^2 \tag{5.2.1}$$

$$\Gamma_{fast} = D^T \cdot q^2 + 6D^R \tag{5.2.2}$$

D^R characterizes the rotational diffusion around the axis perpendicular to the long symmetry axis of the particles.

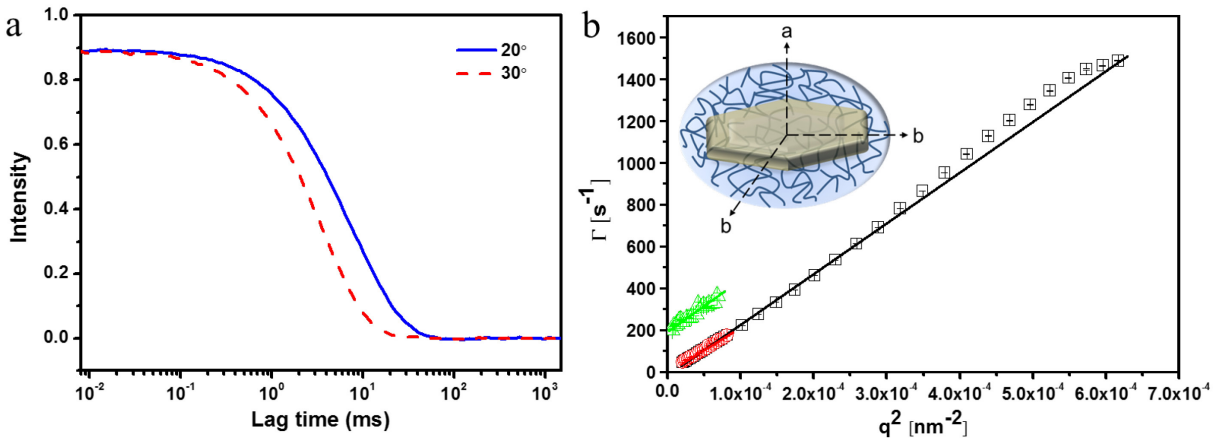

Figure 5.2.7 (a) The correlation functions of the GS-MPS-PNIPAm microgels that are measured at the scattering angle of 20° (blue solid line) and 30° (red dashed line) under the temperature of 50 °C. (b) The relaxation rate Γ is plotted as a function of the square of the scattering vector (q^2). The solid lines are linear fits to the data.

Figure 5.2.7b displays the corresponding relaxation rate Γ plotted as a function of the square of the scattering vector q^2 for the GS-MPS-PNIPAm particles. The slow mode measured from DLS (balck squares) is assigned to the translational motion of the particle, which is comparable to that from DDLS (red circles) within experimental error. Based on the slow mode, the translational diffusion coefficient D^T can be calculated according to equation 5.2.1. The fast DDLS mode (green triangles) describes the rotational relaxation as well as the q-dependent translational term according to equation 5.2.2. The resulting D^T and D^R values of the GS-MPS-PNIPAm microgels at 50 ºC are listed in Table 5.2.1.

Table 5.2.1 Translational diffusion coefficients D^T measured from both DLS and DDLS experiments and rotational coefficients D^R measured from DDLS experiments of the GS-MPS-PNIPAm microgels at 50 °C.

Sample	D^T_{DLS} 10^6 nm^2 s^{-1}	D^T_{DDLS} 10^6 nm^2 s^{-1}	D^R_{DDLS} s^{-1}
GS-MPS-PNIPAm$_{(50\,°C)}$	2.17±0.01	2.07±0.03	28.22±0.05

The Stokes–Einstein relation[250] gives the diffusion constant of a sphere in terms of its size and the solvent viscosity η. Perrin[251] extended the Stokes–Einstein relation to ellipsoids of revolution:

$$D_t = \frac{k_B T}{6\pi\eta a} G(\rho) \tag{5.2.3}$$

$$D_r = \frac{k_B T}{8\pi\eta a^3}\left\{\frac{3}{2}\left[\frac{\left(2-\frac{1}{\rho^2}\right)G(\rho)-1}{1-\frac{1}{\rho^4}}\right]\right\} \tag{5.2.4}$$

where k_B is the Boltzmann constant, T the absolute temperature, $\rho = a/b$, the aspect ratio with the ellipsoid's short half axis a and G(ρ) in case of a oblate ellipsoid of rotation ($\rho < 1$):

$$G_{oblate}(\rho) = \frac{1}{\sqrt{\frac{1}{\rho^2}-1}} \tan^{-1}\sqrt{\frac{1}{\rho^2}-1} \tag{5.2.5}$$

In order to calculate the size parameters of the colloidal particle from the diffusion coefficients, the oblate ellipsoidal model with semiaxis a and b ($a < b$) has been used. The thickness of the PNIPAm shell is assumed to be homogeneous on the core surface. For the viscosity of water at 50 °C, the value η = 0.5465 cp has been used. The semiaxis a is calculated to be 196 nm. The aspect ratio ρ is around 0.7, indicating that the hybrid microgels in the collapsed state still have an anisotropic shape.

In conclusion, core-shell hybrid microgels with single plate-like core and thermosensitive shell of cross-linked PNIPAm have been prepared. The synthetic route involves the synthesis and functionalization of silica coated gibbsite nanoparticles, and the polymerization of NIPAm in the presence of the vinyl groups functionalized GS cores. Imaging techniques such as TEM and SEM have been performed to study the size, shape and polydispersity of the hybrid microgel particles. Furthermore, cryo-TEM microscopy reveals the core-shell morphology of the hybrid microgels. Similar results have been obtained from cross-section analysis of the AFM image of the single hybrid microgel. The latter analysis shows clearly the incorporation of the solid core within the soft microgel. In order to investigate the volume

phase transition behavior of the hybrid microgels, DLS measurements have been used to determine the overall microgel dimensions as a function of temperature. The results indicate that the as-synthesized microgels exhibit a similar swelling-deswelling behavior as that of pure PNIPAm microgels. The analysis by DDLS shows that a rotational diffusion has been observed for the GS-MPS-PNIPAm microgels at 50 °C and the aspect ratio is around 0.7, indicating that the hybrid microgels in the collapsed state still have an anisotropic shape.

In the present study, we have demonstrated that different techniques can be combined to understand the structure and behavior of thermosensitive anisotropic hybrid systems. Moreover, considering the possibility for the further modification of NIPAm with copolymerization with various monomers, it has a remarkable potential for applications combining its thermosensitive properties and anisotropic morphology, for example in the domain of targeted drug delivery, or biological systems where morphological and interactive anisotropy plays a major role.

6. Synthesis of dispersible, monodisperse and mesoporous hollow carbon nanoplates with uniform hexagonal morphologies for supercapacitors

In Chapter 4, PDA serves as a reductant as well as a stabilizer for the generation of Au nanoparticles in situ. In this chapter, PDA is used as carbon precursor to prepare hollow carbon nanoplates (HCPs). These hollow carbon nanoplates can find immediate applications in electrochemistry and catalysis, here exemplified by their capacitance in symmetric supercapacitors. The work of this part aims at the synthesis and characterization of water dispersible hollow carbon nanoplates. Furthermore, the performance of hollow carbon nanoplates in symmetric supercapacitors has been investigated.

Hollow carbon materials, especially those with porous structures, have attracted great interest owing to their intrinsic properties, such as high specific area, high electric conductivity, chemical inertness, compartmentalized structure, and good mechanical strength, making them ideal candidates for energy storage, water treatment, biomedicine, catalyst support, and others.[252–255] Much work has been done to produce hollow carbon materials. Often, amorphous, spherical or tube-like morphology with one-dimensional nanostructure materials such as hollow carbon spheres or carbon nanotubes are obtained,[64,73,256,257] while rare has been reported on other hollow carbon materials, such as carbon nanoplates with graphitic framework structure.[74,75]

Generally, the morphological manipulation of carbon-based materials will vary the interfacial/mutual interaction, leading to new or improved functions.[10] The exploration of hollow and mesostructured carbon nanomaterials with regular morphologies would provide great opportunities to explore the full property spectrum of carbons. To date, two dimensional (2D) carbon materials with high aspect ratios, finite lateral sizes and porous structures have attracted increasing interest, making them desirable for potential applications in energy storage.[76,77,169,258] Carbon nanoplates are exotic carbon 2D nanostructures that have been studied in only limited examples due to their restricted accessability.[74,75] For instance, 2D porous carbon nanosheets and microporous carbon nanoplates have been recently reported to be used in supercapacitors, which could shorten the ion transport distance in their nanoscaled

dimension.[74,75] In comparison, to our best knowledge hollow carbon nanoplates with uniform hexagonal morphologies are unknown carbon nanostructures to be explored.

In this chapter, water dispersible hollow carbon nanoplates have been prepared by using PDA as carbon precursor and hexagonal-shaped gibbsite as template via a silica nanocasting method. Comprehensive characterizations including transmission electron microscopy (TEM), high resolution TEM (HR-TEM), Thermogravimetric analysis (TGA), X-ray diffraction (XRD), Raman spectroscopy, and nitrogen adsorption/desorption isotherms analysis have been performed. Subsequently, the as-obtained hollow carbon nanoplates have been applied as electrodes' materials in symmetric supercapacitors. The performance of hollow carbon nanoplates in symmetric supercapacitors based on PIL binder and commercial standard poly(vinylidene difluoride) (PVDF) has been investigated, respectively, and compared with each other.

6.1 Synthesis of hollow silica nanoplates with a polydopamine shell

Template-based approaches have been broadly used to fabricate hollow carbon materials. These approaches can be categorized into two basic types: The first involves the use of soft templates, consisting of block copolymer aggregates,[259–261] micelles,[262] and bubbles.[263] However, this approach not only requires strict control of the reaction parameters, but also provides relatively limited control over the size and morphology of the structure. Compared to the soft-template approach, the hard-template approach is more effective for controlling the size and overall morphology of the structure. Typically, hard template core such as silica nanoparticles,[264,265] metal oxides,[266] and polymer lattices[267] is first coated with a layer of carbon precursor. Followed by carbonization and removal of the template core, hollow carbon materials are obtained. It is well known that carbon precursors play an important role in the preparation and final physical and chemical properties of the resulting carbon framework. Generally, sucrose, phenol formaldehyde resin, and furfuryl alcohol have been widely used as carbon precursors due to their easy carbonization under inert atmosphere.[73] Unfortunately, none of them can realize the controllable shell thickness.

Dopamine, a biomolecule that contains considerable nitrogen atoms, can be well coated on the plate-like gibbsite surface with controllable thickness according to our previous work. Herein, to create hollow carbon nanoplates, dopamine and hollow silica nanoplate have been chosen as carbon precursor and template core, respectively. As is illustrated in Figure 6.1.1,

silica coated gibbsite particles (GS) are firstly prepared by a Stöber method. After etching the gibbsite cores by concentrated HCl, hollow silica nanoplates (HSP) can be obtained. Polydopamine (PDA), an excellent carbon source, is then self-polymerized on the surface of the hollow silica platelets with controllable thickness under ultrasonification.

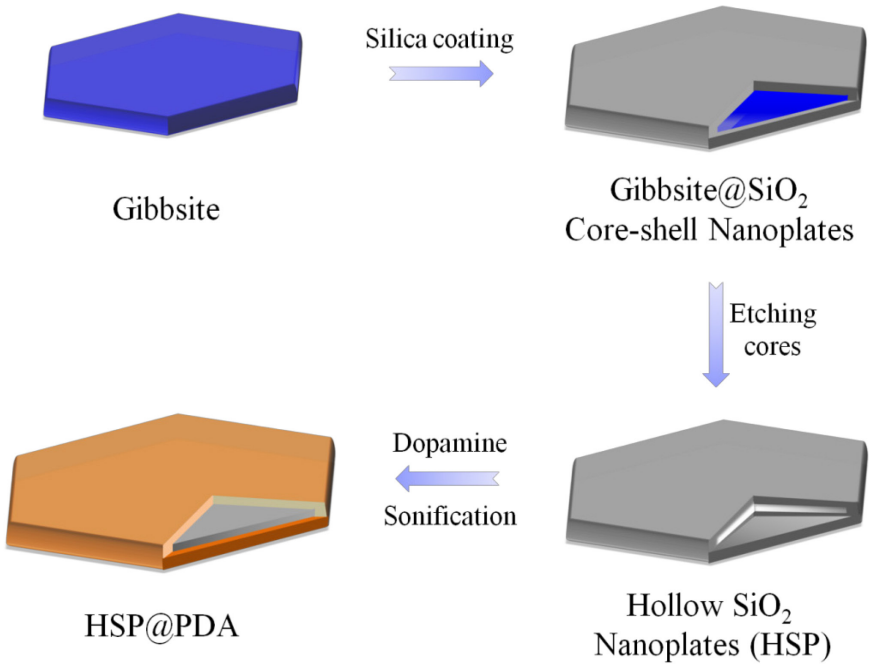

Figure 6.1.1 Synthesis of polydopamine coated nanoplates.

6.1.1 Synthesis of silica coated gibbsite

Gibbsite nanoplates with d = 198 nm prepared in Chapter 4 have been first coated with silica shell using the method described by Wijnhoven.[104] The gibbsite particles have been first treated with PVP, which stabilizes the gibbsite and improves silica growth onto the particle surface. Zeta-potential of the particles converts from 40.3 mV to –19.2 mV, indicating the successful deposition of PVP on the gibbsite surface. Figure 6.1.2a displays a TEM image of the silica-coated gibbsite particles. At some parts of the image, the concentration of the silica-coated gibbsite particles is quite high, showing particles are lying on top of each other. But they are still single particles, not aggregates. Figure 6.1.2b shows the same sample at higher magnification. The silica shell can be distinguished clearly from the TEM image, which is indicated with blue arrows. The whole particle is evenly coated with silica. The coating is very smooth and the thickness of the silica shell is around 8 nm. By measuring the surface area of over 200 individual particles, the average size of silica-coated gibbsite particles has been determined to be 215 ± 27 nm (Figure 6.1.2c). From the EDX spectrum of

the silica-coated gibbsite particles shown in Figure 6.1.2d, the signals of Si, Al, O and Cu can be observed, where Cu signal comes from the Cu foil, indicating the successful modification of silica shell on the gibbsite nanoparticles.

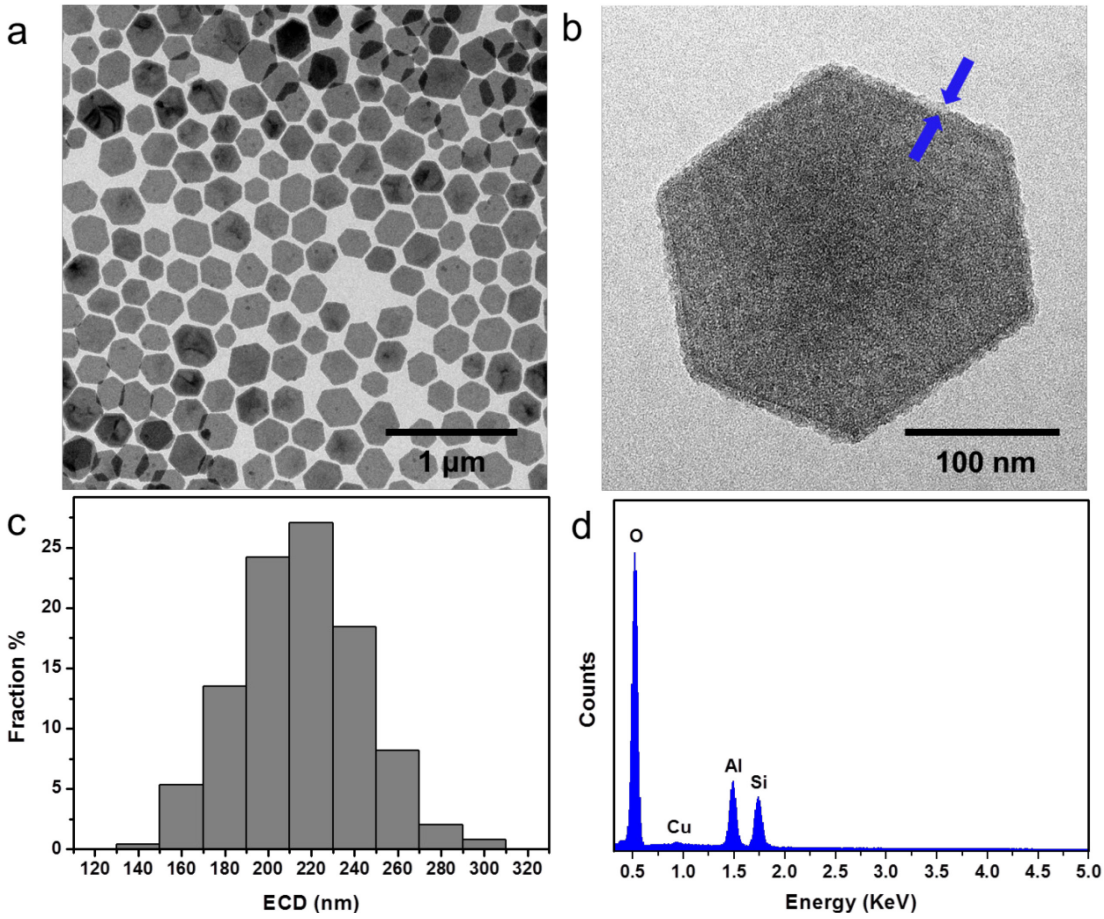

Figure 6.1.2 (a) TEM image of the silica-coated gibbsite particles. (b) TEM image of an enlarged part of a silica-coated gibbsite particle. The blue arrows point to the silica layer (~8 nm thick). (c) Scatter diagram of the equivalent circular diameter (ECD) of the silica-coated gibbsite particles as determined from transmission micrographs, average size 215 ± 27 nm. (d) EDX pattern of the silica-coated gibbsite particles. Cu signal derives from the Cu foil substrate.

There are several pitfalls with this synthesis. Firstly, PVP-coated gibbsite nanoplates should be redispersed in ethanol immediately after centrifugation to prevent PVP desorption from the gibbsite surface and thereby to prevent aggregation. Secondly, it is found that PVP-coated gibbsite particles dispersed in water instead of ethanol will aggregate after being transferred into the Stöber mixture. This indicates that desorption of PVP from the gibbsite surface is probably much faster in water than that in ethanol. Thirdly, once the PVP-coated gibbsite particles are transferred into the Stöber mixture, one should start the silica growth immediately to prevent aggregation. Moreover, it is found that ultrasonification of the mixture

for the first hour during the reaction can effectively prevent aggregation.

6.1.2 Etching gibbsite cores

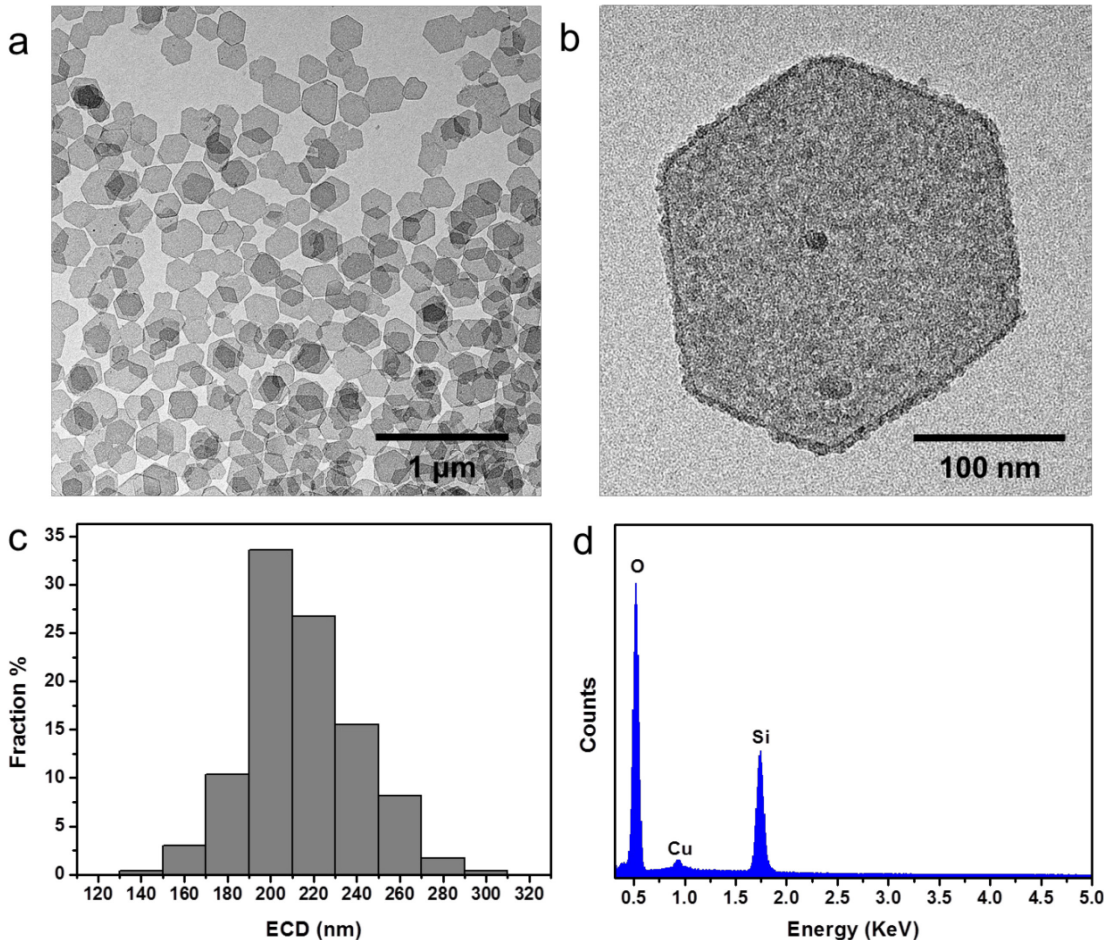

Figure 6.1.3 (a) TEM image of the hollow silica nanoplates after acid etching. (b) TEM image of an enlarged part of a hollow silica nanoplate. The particle is clearly empty inside. (c) Scatter diagram of ECD of the hollow silica nanoplates as determined from transmission micrographs, average size 213 ± 24 nm. (d) EDX pattern of the hollow silica nanoplates. Cu signal derives from the Cu foil substrate.

It is well known that gibbsite is soluble in strong acids, whereas silica not.[104] Thus, the acid-leaching technique is used to prepare hollow silica nanoplates. After acid etching, hollow silica nanoplates can be easily recognized from Figure 6.1.3b showing a light core with dark edge, whereas filled particles are homogeneous. Because the middle of the particles contains less material than the walls, more electrons go through the sample, leading to a lighter contrast on the image. The dark edge is approximately 8 nm thick, consistent with the thickness of the silica layer. This indicates that gibbsite core can be effectively removed by the etching procedure without destroying the integrity of the particles. The average size of the as-obtained hollow silica nanoplates (Figure 6.1.3c) is 213 ± 24 nm, which is similar as the

silica-coated gibbsite particles. To investigate the composition of the produced hollow silica nanoplates, EDX measurement has been conducted. As can be seen from Figure 6.1.3d, Si, O and Cu are the major elements in hollow silica nanoplates, where Cu signal derives from the Cu foil. The absence of Al signal proves the complete removal of the gibbsite core template.

6.1.3 Deposition of PDA

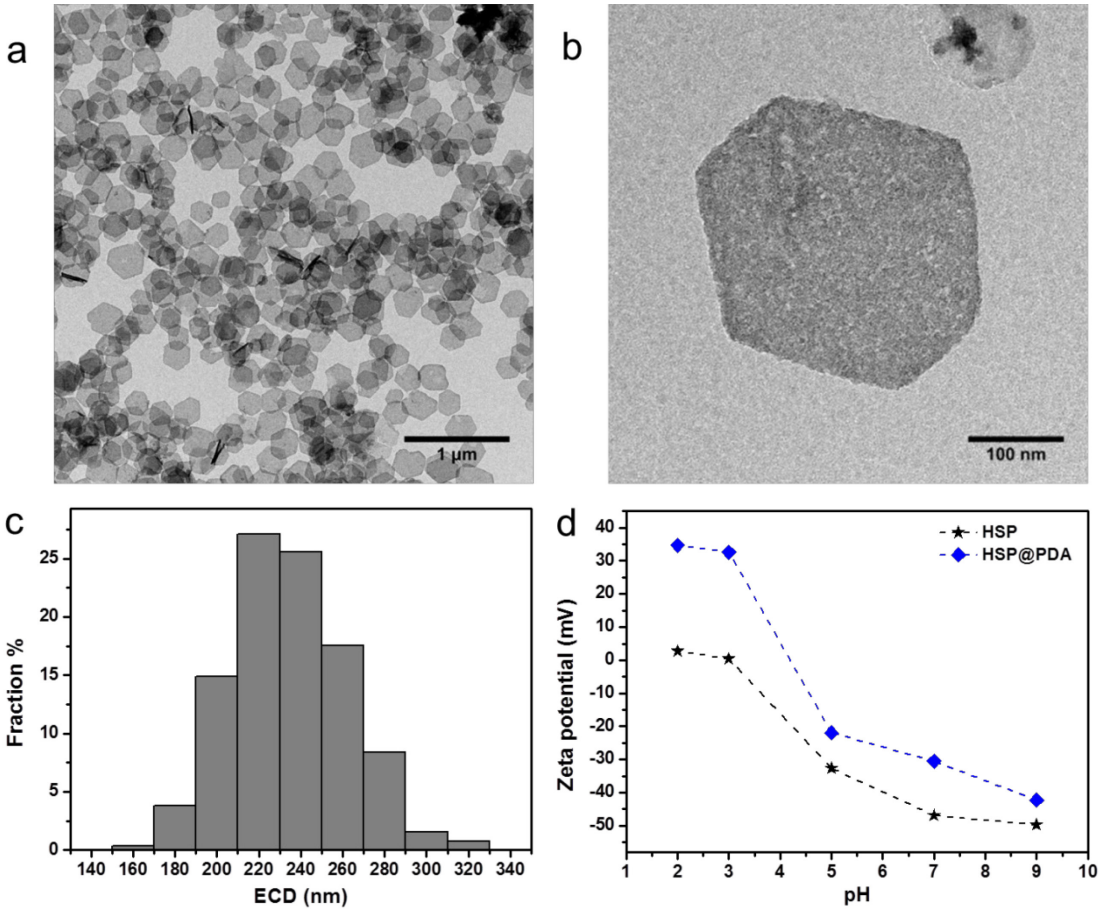

Figure 6.1.4 (a) TEM image of the HSP@PDA core-shell nanoparticles. (b) TEM image of an enlarged part of a HSP@PDA core-shell nanoparticle. (c) Scatter diagram of ECD of the hollow silica nanoplates as determined from transmission micrographs, average size 232 ± 27 nm. (d) Zeta potential of the obtained hollow silica nanoplates (HSP) and HSP@PDA core-shell nanoparticles in aqueous solution at different pH values.

HSP@PDA core-shell nanoparticles have been synthesized through the self-polymerization of dopamine on the surface of hollow silica nanoplates with controllable PDA thickness according to our previous method.[268] Figure 6.1.4a displays the typical TEM image of the HSP@PDA core-shell nanoparticles. No aggregates can be observed because of constant ultrasonification during the polymerization, which prevents the aggregation of hollow silica nanoplates. The hollow structure appears a homogeneous contrast (Figure 6.1.4b) due to the

PDA coating. The thickness of the PDA layer is calculated to be around 9 nm according to the average size of the hollow silica nanoplates (213 nm, Figure 6.1.3c) and the HSP@PDA core-shell nanoparticles (232 nm, Figure 6.1.4c). The successful PDA coating has been further confirmed by zeta-potential measurements. As shown in Figure 6.1.4d, the HSP@PDA core-shell nanoparticles exhibit zwitterionic property, and can be dispersed in aqueous solution when pH value is higher than 7 or lower than 3. As comparison, hollow silica nanoplates can be dispersed in aqueous solution only when the pH value is higher than 5.

In conclusion, anisotropic plate-like HSP@PDA core-shell nanoparticles have been successfully obtained. Silica-coated gibbiste particles with a silica shell of 8 nm have been firstly synthesized and characterized by TEM and EDX measurements. The gibbsite core can then be removed by acid etching. TEM and EDX characterizations of the resulted hollow silica nanoplates demonstrate the complete removal of gibbsite cores and the integrity of the hollow particles. Dopamine is then self-polymerized on the surface of the hollow silica nanoplates and forms a homogenous layer on it. The resulted well-defined HSP@PDA core-shell nanoparticles show zwitterionic property, which is demonstrated by zeta potential measurements.

6.2 Synthesis and characterization of hollow carbon nanoplates

Normally, all carbon nanostructure will inevitably conglutinate and non-dispersible bulk material forms during the high-temperature annealing. One method for overcoming this limitation was firstly reported Lu *et al.*[269] Discrete and dispersible hollow carbon spheres were obtained by using phenol and formaldehyde as carbon precursors via confined pyrolysis of silica-coated core-shell polymeric particles. Later, Soll *et al.* synthesized water dispersible carbon nanobubbles by using poly(ionic liquid) as carbon precursors via a silica nanocasting method.[270]

We present in this work the first report on the water dispersible hollow carbon nanoplates via a silica nanocasting method which is illustrated in Figure 6.2.1. The general synthetic routes to the hollow carbon nanoplates involve the formation of an inorganic outer silica shell that functions as a nanoreactor to provide a confined nanospace for high-temperature treatment. Each single HSP@PDA nanoparticle isolated in the silica hybrid is therefore converted to carbon during the calcination. Finally, discrete and dispersible hollow carbon nanoplates are

obtained after etching of silica.

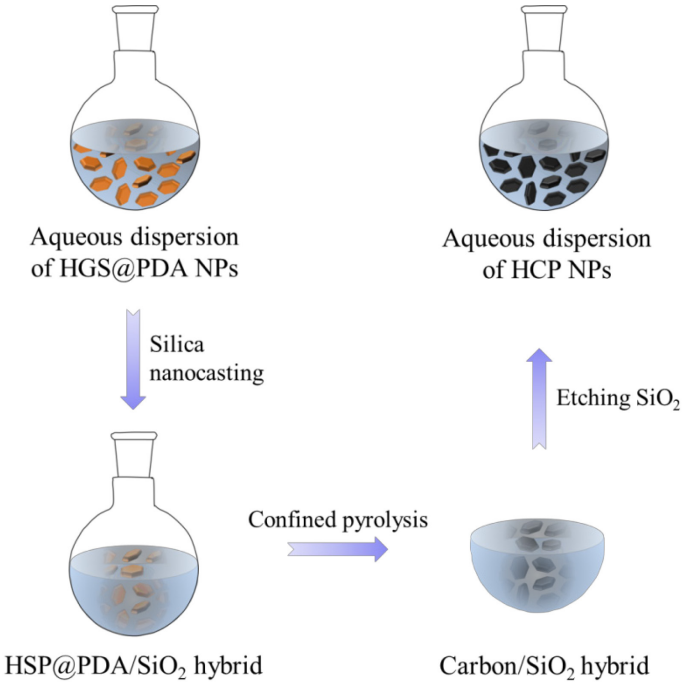

Figure 6.2.1 Synthetic route to water dispersible hollow carbon nanoplates by confined carbonization of HSP@PDA core-shell nanoparticles in a silica matrix.

To ensure a uniform silica coating, the dispersity and the surface charge of the HSP@PDA nanoparticles in aqueous solution are crucial. Considering that HSP@PDA nanoparticles are positively charged and stable when the pH value is 2, we therefore adjust the pH to approximately 2. Silica coating is realized by dropwise addition of tetraethyl orthosilicate (TEOS) into the aqueous dispersion of the HSP@PDA nanoparticles under vigorous stirring. Negatively charged hydrolyzed silica moieties (partially hydrolyzed TEOS or oligomers) react with positively charged HSP@PDA surface through the electrostatic interaction, which results in the successful surface coating with silica. After slow condensation, the mixture slowly solidifies and forms viscous gel-like network. By using this technique, individual HSP@PDA nanoparticle is initially coated with a silica layer on the outer surface, and eventually immobilized in a compact silica gel. TEM measurements confirm that HSP@PDA nanoparticles are well embedded in the silica gel and isolated. The dashed white lines in Figure 6.2.2a indicate the isolated HSP@PDA nanoparticles in the silica matrix. Figure 6.2.2b shows one of the HSP@PDA nanoparticles trapped in silica gel at higher magnification. The trapped core-shell nanostructure is clearly visible by TEM due to the different electron contrast between the silica and PDA. Hollow core, silica shell and PDA layer (~9 nm) can be observed and are indicated with a red arrow, a blue arrow and a black arrow, respectively.

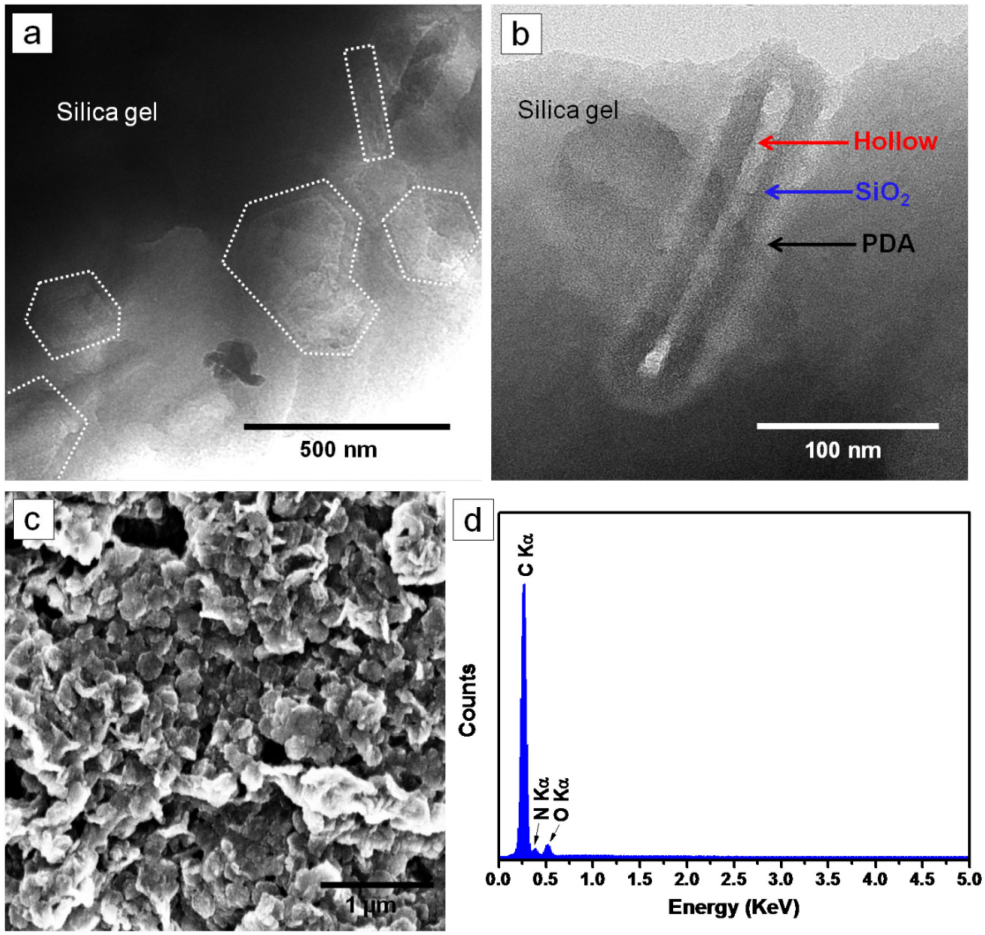

Figure 6.2.2 (a) TEM images of the HSP@PDA nanoparticles/silica hybrids before carbonization. The dashed white lines point to the isolated HSP@PDA nanoparticles in silica gel. (b) TEM image of the HSP@PDA nanoparticles/silica hybrids. The red arrow points to the hollow core. The blue arrow points to the silica layer. The black arrow points to the PDA layer. (c) SEM image of the hollow carbon nanoplates. (d) EDX spectrum of the hollow carbon nanoplates.

Subsequently, HSP@PDA nanoparticles trapped in the silica gel are converted into isolated carbon nanoplates after calcination at 800 °C under argon flow. Discrete and monodispersed hollow carbon nanoplates are obtained after elimination of the silica portion (core and outer shell). SEM image in Figure 6.2.2c shows that the obtained hollow carbon nanoplates preserve the structural integrity and hexagonal morphology. The hollow carbon nanoplates are either standing on their sides or lying flat. The EDX spectrum in Figure 6.2.2d shows that C, N and O are the major elements in the sample, indicating the complete removal of the silica.

The TEM image in Figure 6.2.3a clearly shows that the hollow carbon nanoplates are monodisperse and uniformly hexagonal, with diameter of approximately 231 nm (Figure 6.2.3b), which is consistent with the particle size of the HSP@PDA nanoparticles. Moreover,

no other amorphous clustered materials can be observed. As can be seen from Figure 6.2.3c and d, the obtained hollow carbon nanoplate has a hollow core of ~25 nm in height with a carbon shell of ~9 nm thick.

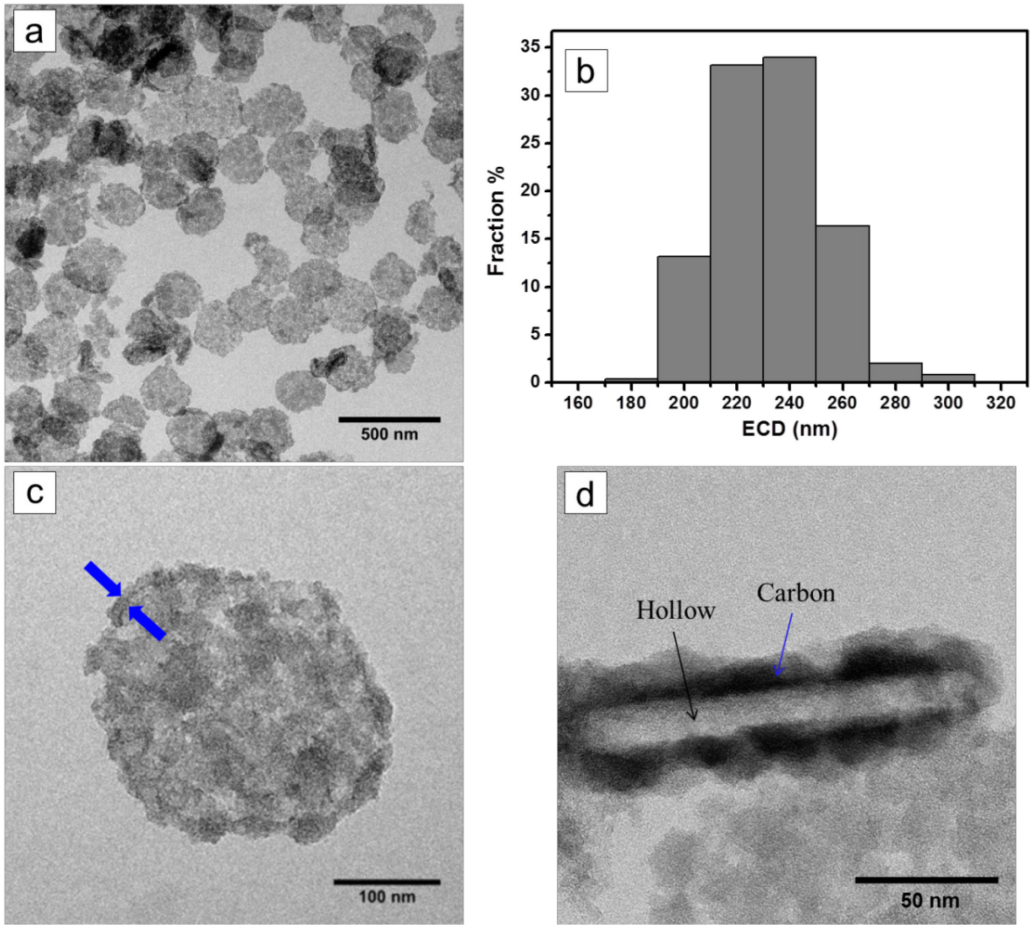

Figure 6.2.3 (a) TEM image of the hollow carbon nanoplates. (b) Scatter diagram of ECD of the hollow carbon nanoplates as determined from transmission micrographs, average size 231 ± 20 nm (c) TEM image of an enlarged part of a hollow carbon nanoplate. The blue arrows point to the carbon layer (~9 nm thick). (d) TEM image of a standing hollow carbon nanoplate. The blue and black arrows point to the carbon layer and hollow core, respectively.

As shown in Figure 6.2.4a, the as-synthesized hollow carbon nanoplates, when released from silica solid, are well-dispersed in water, with no sign of precipitation for days. Only after 1 week, the upper part of solution starts to become slightly less dark than the lower part. However, no sediment can be observed. Since no surfactant has been used to stabilize the hollow carbon nanoplates, the superior dispersability mainly results from the strong electrostatic repulsion between the spontaneously charged hollow carbon nanoplates.[270] This is proved by zeta-potential value of the hollow carbon nanoplates (–25 mV) under pH neutral conditions, which follows the rule of spontaneous polarization. In acidic or basic conditions,

hollow carbon nanoplates precipitate within 1 day, which excludes ion adsorption as the reason of the spontaneous stability. For further understanding the porous texture, N_2 adsorption-desorption isotherms of the hollow carbon nanoplates have been measured. The corresponding N_2 adsorption-desorption isotherms and pore size distribution are shown in Figure 6.2.4b. The N_2 sorption clearly demonstrates the mesoporosity of these hollow carbon nanoplates as they have a high nitrogen uptake. The BET specific surface area of the hollow carbon nanoplates is measured to be about 460 $m^2 \cdot g^{-1}$ with a pore volume of 0.45 $cm^3 \cdot g^{-1}$. The pore size distribution (the inset plot in Figure 6.2.4b), calculated from the desorption data in terms of the BJH model, is estimated to be ~3.8 nm. In addition, TGA analysis of the hollow carbon nanoplates shown in Figure 6.2.4c further indicates the complete removal of the inorganic parts (*i.e.*, Si and Al).

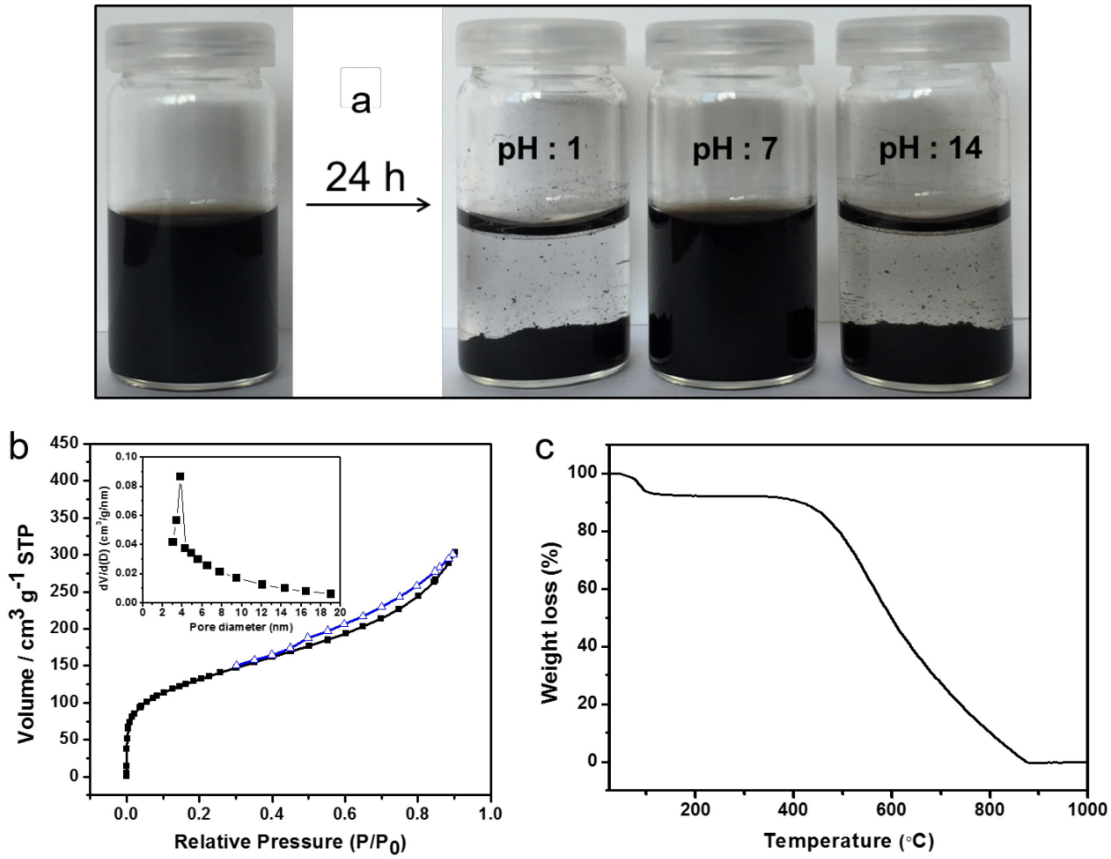

Figure 6.2.4 (a) Photographs of the hollow carbon nanoplates dispersed in aqueous dispersion at different pH conditions. (b) Nitrogen adsorption and desorption isotherm of the hollow carbon nanoplates. Inset: BJH pore-size distribution curve of the hollow carbon nanoplates, which was determined from the desorption branch of the isothermal. A centre peak at 3.8 nm (pore diameter) can be clearly observed. (c) TGA analysis of the hollow carbon nanoplates.

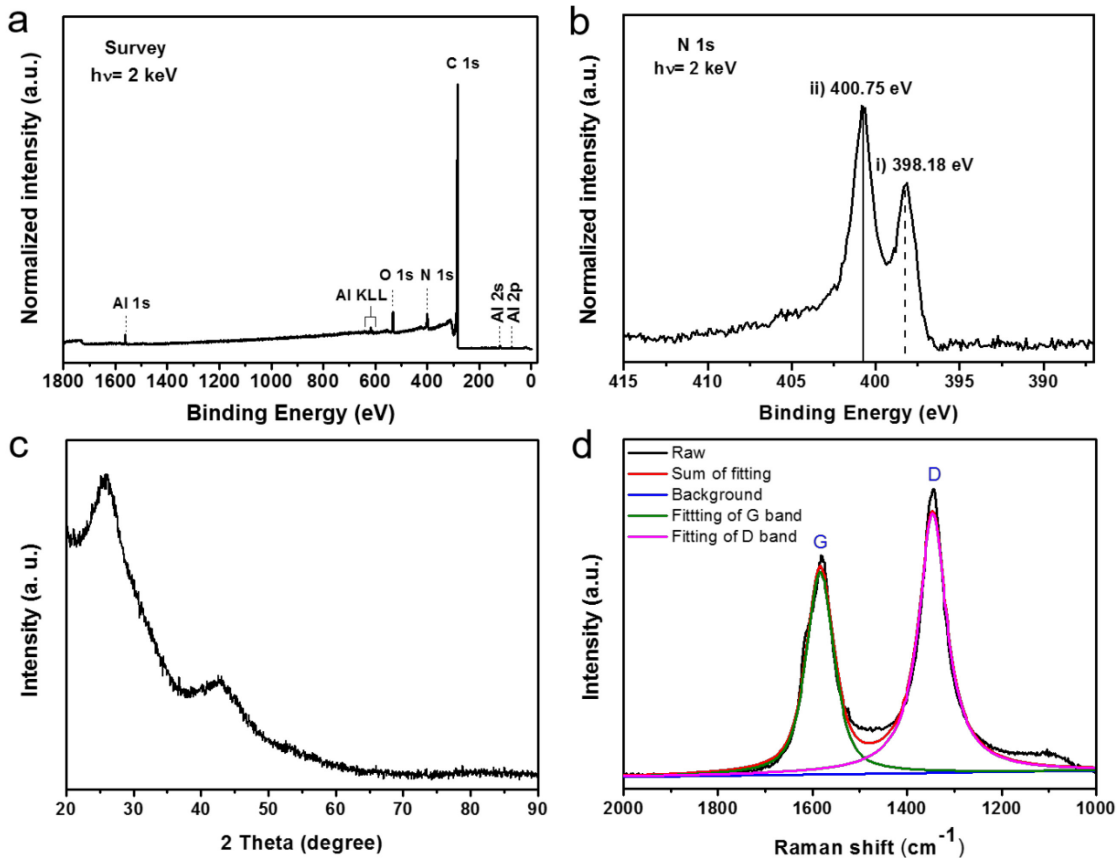

Figure 6.2.5 (a) HAXPES survey spectrum of the hollow carbon nanoplates. (b) HAXPES spectrum of the N 1s core level of the hollow carbon nanoplates. (c) XRD pattern of the hollow carbon nanoplates. (d) Raman spectrum of the hollow carbon nanoplates. The weak peak at ~1100 cm^{-1} derives from the glass substrate.

To investigate the surface composition and chemical states of the hollow carbon nanoplates, HAXPES measurements have been conducted for the hollow carbon nanoplates casted on Al foil. Figure 6.2.5a shows the HAXPES survey spectrum of this sample along with respective peak identification. The spectrum consists mainly of photoelectron lines derived from the hollow carbon nanoplates (*i.e.*, C, N and O). Al-related lines are derived from the Al foil support. Moreover, the absence of Si-related photoelectron lines (*i.e.,* Si 2p and 2s core levels at binding energy values ca. 99 and 151 eV, respectively) indicates that silica has been completely removed by etching. HAXPES detail spectra of the N 1s core level energy regions have also been measured. The high-resolution N 1s spectrum of the hollow carbon nanoplates, shown in Figure 6.2.5b displays two prominent peaks at binding energy: i) 398.18 ± 0.05 and ii) 400.75 ± 0.05 eV, which are assigned to pyridinic-N and graphitic-N, respectively.[271] The latter is more pronounced, indicating that nitrogen is dominantly incorporated into the graphitic structure. Similar results have been also reported by Soll *et al.* for the carbon nanobubbles system.[270] The elemental composition of the hollow carbon nanoplates has been

obtained by combustion elemental analysis. As listed in Table 6.2.1, the N/C ratio is 0.09, and the nitrogen content is as high as 7.2 wt%, which is quite beneficial to improve the polarity and wettability of the carbon surface as well as to enhance the electric conductivity.[272]

Table 6.2.1 Elemental composition information of the hollow carbon nanoplates.

C (wt%)	N (wt%)	H (wt%)	O (wt%)	N/C
79.42	7.16	1.67	11.75	0.090

XRD and Raman spectroscopy are used to investigate the crystalline structure of the hollow carbon nanoplates. Figure 6.2.5c shows the XRD pattern of the hollow carbon nanoplates. Two diffraction reflections at 2θ = 25° and 43° are observed. The reflection at 2θ = 25° is associated to the (002) of the graphitic carbon, and the broad (10) reflection at 2θ = 43° originates from the in-plane reflection of the graphitic carbon. In the Raman spectrum (Figure S7), two obvious bands appear at ~1345 and ~1575 cm^{-1}, which correspond to the D band and G band, respectively. The D band is recognized to be a disordered band, and the G band corresponds to the in plane stretching motion between sp^2 carbon atoms.[273] The D/G intensity ratio is ~1.5, which indicates that the hollow carbon nanoplates are partially graphitized.[273] This means they contain some graphitic domains in the amorphous phase, which is in good agreement with the HR-TEM measurements.

To further investigate details of the local structure, hollow carbon nanoplates have been characterized by high resolution TEM (HR-TEM). As shown in Figure 6.2.6a and b, onion-like stacking nanostructures with several tens of stacking layers can be clearly observed. The interlayer spacing of these nanostructures is around 0.35 nm, which is the typical distance between graphite layers (parts c and d in Figure 6.2.6). This is in agreement with literature report.[274] It is believed that a layered-stacking supramolecular structure of PDA is responsible for the formation of graphite-like nanostructure.[275] The HR-TEM results are consistent with Raman and XRD results, indicating that the obtained hollow carbon nanoplates are partially graphitic.

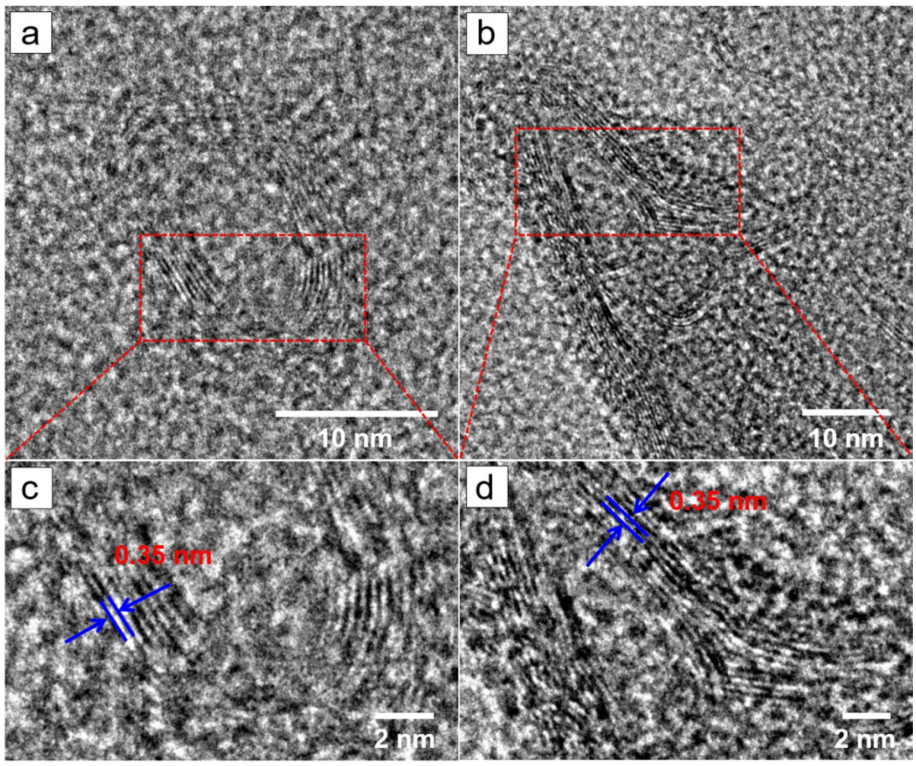

Figure 6.2.6 (a, b) HR-TEM images show the enlarged graphite-like domain in the hollow carbon nanoplates, which contains over 10 stacking layers. (c, d) HR-TEM images of the magnified part in (a and b). The interlayer distance is 0.35 nm.

In conclusion, we have successfully synthesized highly dispersible, monodisperse and mesoporous hollow carbon nanoplates with uniform hexagonal morphology by using dopamine as a carbon source and hexagonal gibbsite as template via a silica nanocasting method. To the best of our knowledge, this is the first report on monodisperse 2D hollow carbon nanoplates with mesoporous nanostructures. The as-obtained hollow carbon nanoplates show excellent colloidal stability and have a specific surface area (460 $m^2 \cdot g^{-1}$) and highly accessible mesopores (~3.8 nm). The nitrogen content of the hollow carbon nanoplates has been measured to be approximately 7.2 wt% by combustion elemental analysis. HR-TEM, XRD, and Raman measurements indicate that the obtained hollow carbon nanoplates are partially graphitic. Owing to the high nitrogen doping, superior dispersity and 2D mesoporous nanostructures, the hollow carbon nanoplates obtained by this approach not only hold great promise in many fields such as advanced energy storage materials, drug delivery carriers, adsorbents, and catalyst supports, but also may act as a model system for exploring the physical and chemical properties of carbon colloids.

6.3 Electrochemical properties of the hollow carbon nanoplates

Hollow carbon materials, especially those with porous structures, are the most promising candidates and have been widely investigated as the electrode material for energy storage systems owing to their outstanding physicochemical properties such as chemical inertness, rich abundance and tunable electrical conductivity.[276] Considering a combination of the unique plate-like hollow structure, the nano-sized dimension as well as high nitrogen doping, the as-synthesized hollow carbon nanoplates are expected to be a potential electrode material for electrochemical devices. In our study, the as-synthesized hollow carbon nanoplates have been tested as electrode materials for supercapacitors. Moreover, a recent study shows that the performance of supercapacitor might differ depending on the selected binder.[277] As one of the most commonly used binder in supercapacitor, poly-(vinylidene fluoride) (PVDF) still has some drawbacks such as the limited surface activity to bind eventually all electrode components as well as reduction of pore volume of the active materials.[278,279] Thus, the pursuit for more functional and efficient binders is therefore still an open race with high potential benefits. Recently, poly(ionic liquid) (PIL) based nanoparticles as a new generation binder material have been prepared and employed as a polymeric binder in lithium ion batteries, which show better performance than commercial standard PVDF.[280] However, to the best of our knowledge, no investigation has been performed to compare their performance in other electrochemical devices such as supercapacitors. In this section, the as-obtained hollow carbon nanoplates have been applied as electrodes' materials in symmetric supercapacitors. In addition, the performance of symmetric supercapacitors based on PIL binder and commercially available binder PVDF has been measured and compared.

6.3.1 Electrochemical properties of hollow carbon nanoplates by using PIL as binder

To examine the capacitive properties of the hollow carbon nanoplates, cycle voltammograms (CV) and galvanostatic charge−discharge evaluations have been performed in a two-electrode cell by using PIL as binder. Li_2SO_4 has been chosen as electrolytes, due to such advantages as higher electrochemical window, low cost, environmental friendly character, and low corrosive properties comparing with other aqueous electrolytes like H_2SO_4 and KOH.[281] The CV curves (Figure 6.3.1a) operating at different cell voltage exhibit a rectangular shape at voltage up to 1.4 V, suggesting a pure capacitive behavior. The anodic current increases proportionally as the cathodic current with the cell voltage extending from 0.8 to 1.4 V, indicating good reversibility of the charge storage process. However, when the cell voltage is increased to 1.6

V, a sharp current leap took place during the anodic scan, and its counterpart is not symmetric during the negative scan, these phenomena are corresponding to the irreversible oxidation of carbon in positive electrode or hydrogen evolution in negative electrode. When the voltage is higher than 1.4 V, hollow carbon nanoplates are no longer stable and will be electrochemically oxidized during electrochemical measurements. Thus, the stable voltage window is 0−1.4 V. Figure 6.3.1b shows the CV curves of the symmetric supercapacitor from 0 to 1.4 V at different scan rates of 10−300 mV/s, which exhibit a quasi-rectangular and symmetric shape. Even at a scan rate as high as 300 mV/s, the CV curve still shows a nearly rectangular shape, suggesting ideal capacitive behavior and desirable fast charging–discharging property for power devices.

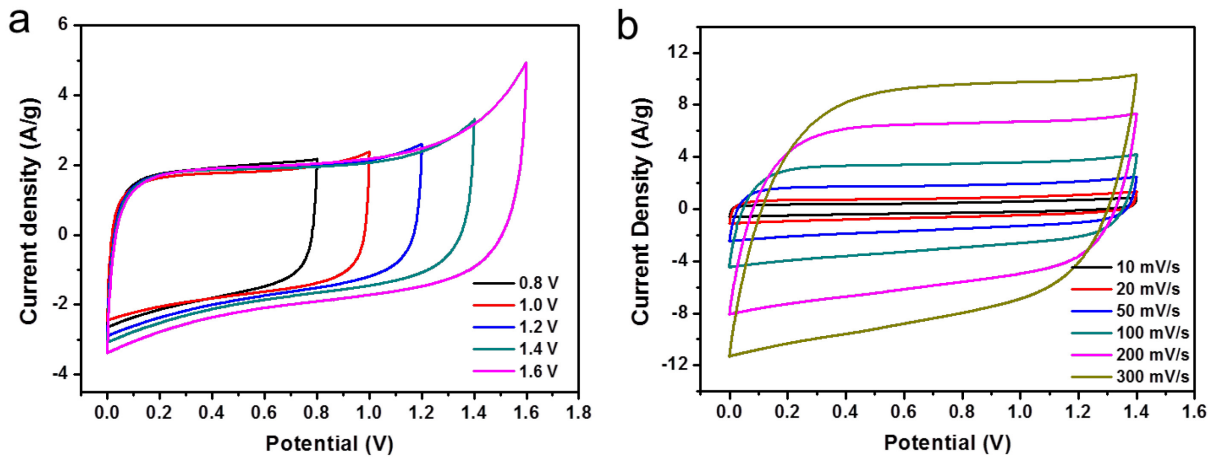

Figure 6.3.1 (a) CV curves for hollow carbon nanoplates based symmetric supercapacitors by using PIL as binder (50 mV/s, 1mol/L Li_2SO_4), and (b) CV curves at scan rates of 10−300 mV/s.

It is well accepted that galvanostatic charge/discharge examination is an established method for evaluating the supercapacitive performance. The galvanostatic charge–discharge curves from 0 to 1.4 V at current densities, as presented in Figure 6.3.2a, show the linear voltage–time relation, characteristic of an electrical double layer capacitance. Moreover, each charging curve is symmetric to its corresponding discharge counterpart, confirming a pure capacitive behavior. The relationships between the specific capacitance and different current densities of the ultrathin hollow carbon nanoplates are illustrated in Figure 6.3.2b. It is noted that the specific capacitance of hollow carbon nanoplates can achieve a maximum of 124 F/g at 0.25 A/g. The specific capacitance values obtained at 0.5, 1, 2.5, 4 and 5 A/g are 88, 84, 76, 70 and 67 F/g, respectively. Even at high current density (10 A/g), the specific capacitance still remains 56 F/g (about 45% retention), which indicates excellent high power capability.

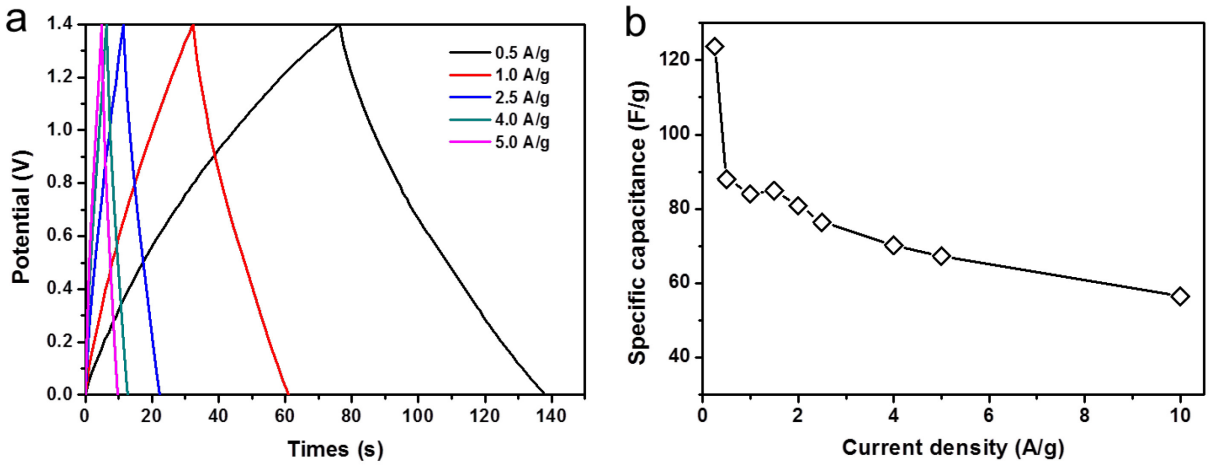

Figure 6.3.2 (a) Galvanostatic charge/discharge curves at current densities of 0.5−5 A/g of hollow carbon nanoplates based symmetric supercapacitors by using PIL as binder, and (b) the relationships between the specific capacitance and different current densities of hollow carbon nanoplates based symmetric supercapacitors.

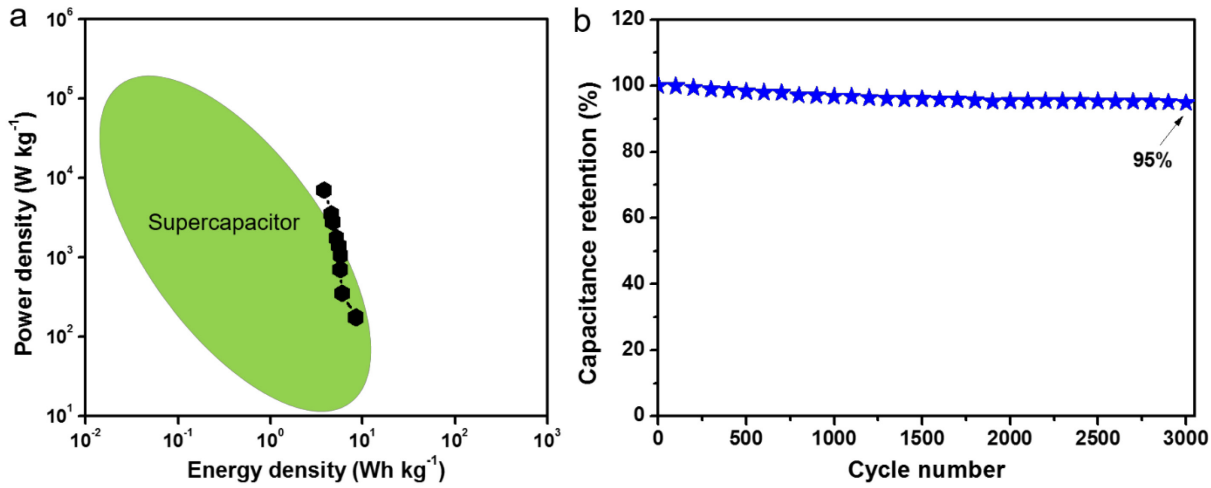

Figure 6.3.3 (a) Ragone plot of gravimetric energy density versus power density for the HCPs based symmetric supercapacitor by using PIL as binder. The green area indicates the Ragone plot for supercapacitors. (b) The cyclic performance of hollow carbon nanoplates based symmetric supercapacitors by using PIL as binder in the voltage window between 0 to 1.4 V at a current density of 2.5 A/g.

To evaluate the supercapacitor performance of the hollow carbon nanoplates based symmetric cell, the values of specific energy and specific power were plotted in a Ragone plot, as shown in Figure 6.3.3a. The maximum energy and power densities of this device are 8.4 Wh·kg^{-1} and 7000 W·kg^{-1}, respectively. To further demonstrate the advantages of the hollow carbon nanoplates for supercapacitor applications, the life cycle test was carried out using charge−discharge measurement at a constant current density of 2.5 A/g (the capacitance value at this current density is 76 F/g) up to 3000 cycles. As can be observed from Figure 6.3.3b,

these electrodes exhibited stable performance up to 3000 cycles with a negligible loss of only 5%, indicating that the as-synthesized hollow carbon nanoplates possess a superior electrochemical stability.

6.3.2 Electrochemical properties of hollow carbon nanoplates by using PVDF as binder

The capacitive properties of the hollow carbon nanoplates have been also investigated in a two-electrode cell by using commercial available PVDF as binder in Li_2SO_4 electrolyte. Cycle voltammograms have been firstly performed at scan rate of 50 mV/s. As shown in Figure 6.3.4a, the cyclic voltammograms operating at different cell voltage exhibit good rectangular shape at voltage up to 1.4 V. The same stability window can be observed for the symmetric supercapacitors by using PVDF as binder, confirming that the wide potential window obtained in Li_2SO_4 is inherent to the nature of the electrolyte. Moreover, the curve area of hollow carbon nanoplates by using PVDF as binder is smaller than that of PIL as binder at scan rate of 50 mV/s, suggesting that supercapacitors based on PIL as binder show better ion storage capability than that of PVDF. Figure 6.3.4b shows the CV curves of PVDF based supercapacitors from 0 to 1.4 V at different scan rates of 10−300 mV/s. It can be seen that the rectangular shape of CV curves of PVDF based supercapacitors is more distorted with increased scan rate than that of PIL based supercapacitors, which again imply that PIL based supercapacitors possess better capacitive behavior than PVDF based supercapacitors. Generally, the better accessibility of the ions to the electrochemically active surface, the better capacitive at high scan rate.

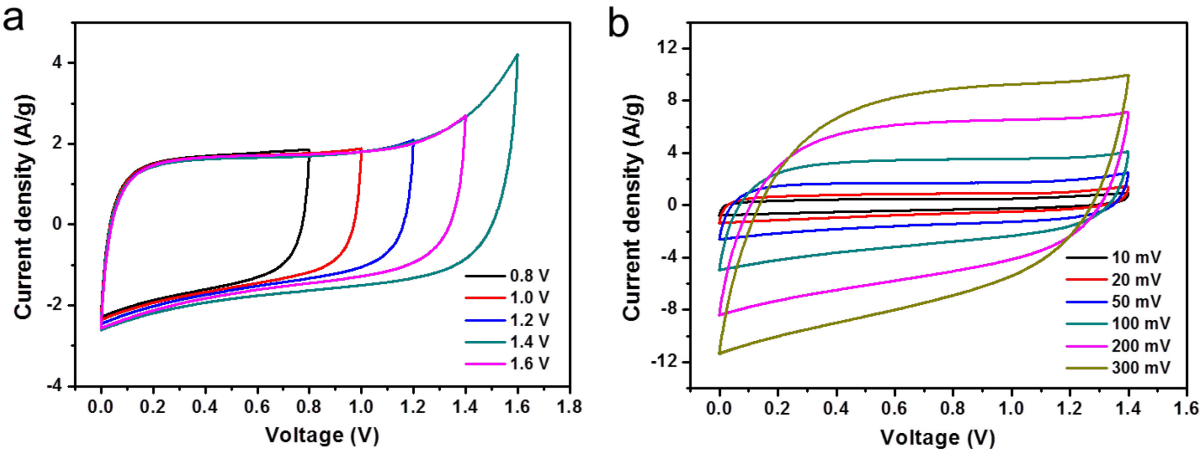

Figure 6.3.4 (a) Cyclic voltammetry curves for hollow carbon nanoplates based symmetric supercapacitors using PVDF as binder (50 mV/s, 1mol/L Li_2SO_4) and (b) CV curves at scan rates of 10−300 mV/s.

Figure 6.3.5a shows the charge/discharge curves of PVDF based supercapacitors at different current densities of 0.5−5 A/g. Similarly, the charging curves are symmetric to their corresponding discharge counterparts. The relationships between specific capacitance and charge/discharge current density for PVDF based supercapacitors are illustrated in Figure 6.3.5b. As can be observed, the specific capacitance of HCPs is only 103 F/g at 0.25 A/g for using PVDF as binder, lower than that for PIL. The specific capacitance values obtained at 0.5, 1, 2.5, 4, 5, and 10 A/g are 80, 74, 68, 63, and 59 F/g, respectively, which are also much lower than that of using PIL as binder. Thus, it is concluded that PIL is a promising candidate as binder for supercapacitors than the commercial available PVDF binder. This difference in capacitance may result from that the PVDF based electrodes cause a more pronounced reduction of pore volume as compared to PIL nanoparticles binder. In addition, PIL networks may form a homogeneous, comparably better conductive matrix than PVDF binder to enhance the charge flow and transfer. This test on one side verifies PIL nanoparticles as a top candidate to replace PVDF as binders for supercapacitors; on the other side it motivates us to understand the inherent mechanism of the unusual function of the PIL binder in the electrochemical environment.

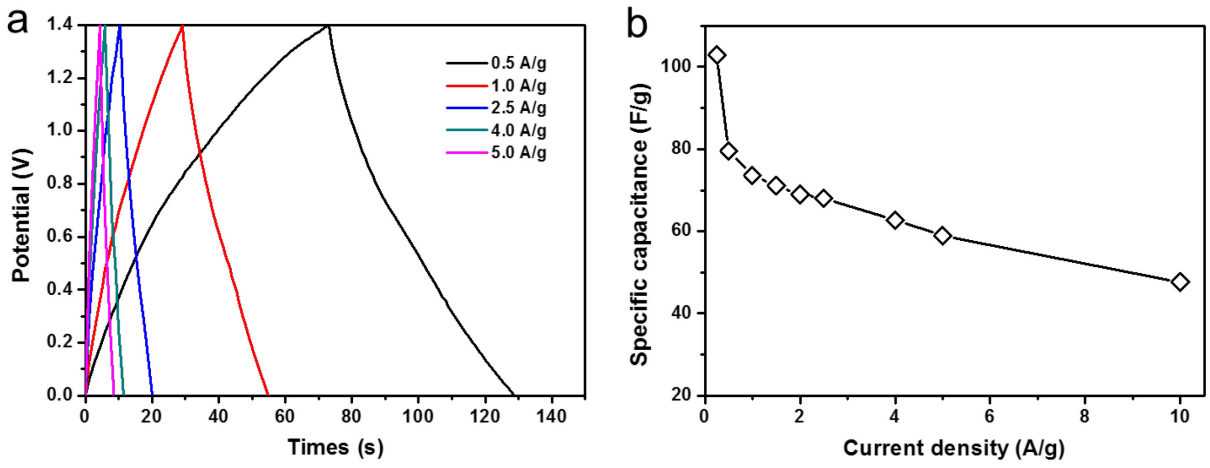

Figure 6.3.5 (a) Galvanostatic charge/discharge curves at current densities of 0.5−5 A/g of PVDF based electrodes, and (b) the relationships between the specific capacitance and different current densities of hollow carbon nanoplates based supercapacitors using PVDF as binder.

The cycle ability of hollow carbon nanoplates based electrodes using PVDF as binder has been also measured by galvanostatic charge–discharge studies at a current density of 2.5 A/g as shown in Figure 6.3.6. The hollow carbon nanoplates demonstrate excellent electrochemical stability that it still maintains about 97% capacitance of the initial value after continuous cycles of 3000 times.

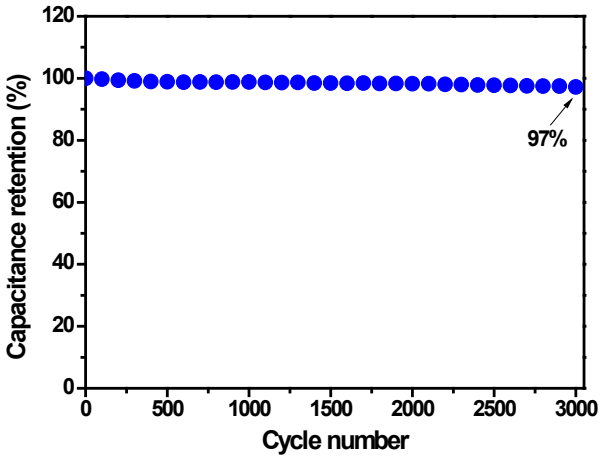

Figure 6.3.6 The cyclic performance of hollow carbon nanoplates based symmetric supercapacitor using PVDF as binder in the voltage window between 0 to 1.4 V at a current density of 2.5 A/g.

Additional comparison about the capacitance has been made for the hollow carbon nanoplates and other reported carbon materials as symmetric supercapacitor electrodes in neutral electrolyte (Table 6.3.1). In general, hollow carbon nanoplates show quite high capacitance, which is comparable with carbon materials with very high surface area, such as activated carbon xerogel,[282] commercial carbon,[283] and seaweed carbon[284]. Comparing with carbon materials with similar surface area, such as partially exfoliated and reduced graphite oxide (PE-RGO),[285] and ball-milled graphite,[286] the hollow carbon nanoplates show much higher catalytic activity. Such excellent electrochemical performance can be mainly attributed to the following several obvious advantages: (a) The nano-sized hollow carbon nanoplates can enhance the utilization of materials; (b) The hollow interiors can act as ion-buffering reservoirs which diminish the volume expansion during the repeated ionic adsorption and desorption process, resulting in an enhanced stability; (c) The 2D structure of hollow carbon nanoplates with mesoporous feature can allow a high rate of electrolyte infiltration and fast diffusion of the ions and electrons.

Table 6.3.1 Comparison of our symmetric supercapacitors data with reported carbon-based symmetric supercapacitors using neutral electrolytes.

Sample	Surface area (m^2/g)	Electrolyte	Voltage (V)	Current density (A/g)	Capatiance (F/g)	Ref.
Activated carbon xerogel	2876	Na_2SO_4	1.0	0.2	140	[282]
Commercial carbon	2250	Na_2SO_4	1.6	0.2	135	[283]
Seaweed carbon	1082	Na_2SO_4	1.6	0.2	123	[284]
Ball-milled graphite	422	Na_2SO_4	1.4	0.2	79	[286]
PE-RGO	395	Na_2SO_4	1.6	0.2	~82	[285]
HCPs (PIL)	460	Li_2SO_4	1.4	0.25	124	This work
HCPs (PVDF)					103	

In conclusion, the hollow carbon nanoplates have been tested as electrode materials in symmetric supercapacitor in neutral electrolyte. The present results have shown that the as-designed hollow carbon nanoplate is a very promising electrode material for high performance supercapacitors. In addition, it has been demonstrated that the PIL nanoparticle binder as a new generation binder material enhances dramatically the electrodes' performance, and delivers a higher specific capacity than PVDF in 1 M Li_2SO_4 aqueous solution. The present study not only proves the PIL binder to be a high-performance binder for supercapacitor electrodes, but also sheds light on the design of carbon nanomaterials with novel structures suitable for energy storage systems.

7. Summary and outlook

In the present work, novel synthetic approaches have been developed for the surface modification of gibbsite platelets with PDA and thermosensitive PNIPAm. Due to the new functionalities originated from the polymer shell and the plate-like morphology of the gibbsite core, polymer coated gibbsite platelets can be further applied in catalysis and energy storage system. The work presented here has been split into three main parts.

First, a dopamine-based approach for the encapsulation of platelet-like gibbsite to synthesize anisotropic gibbsite-polydopamine (G-PDA) core-shell nanoplates has been developed. Good control over the plate-like morphology and 100 % encapsulation efficiency has been achieved via this route. The anisotropic G-PDA core-shell nanoplates show excellent colloidal stability, leading to the formation of columnar crystal after centrifugation. Due to the reducing ability of the PDA shell, Au nanoparticles (NPs) have been generated in situ on the G-PDA particle surface without addition of any reductant or stabilizer. The size of the Au NPs can be controlled by changing the dosage of $HAuCl_4$ and the reaction time. The G-PDA-Au nanocomposites show high catalytic activity in the reduction of 4-nitrophenol and Rodamine B (RhB). Moreover, the substrate-immobilized G-PDA-Au nanocatalysts have been obtained by spin-coating the G-PDA-Au nanocatalysts onto the silicon substrate, which show excellent catalytic recyclability.

In the second part of the thesis, core-shell microgel with single plate-like core and PNIPAm shell with controllable thickness has been prepared via seeded emulsion polymerization. The synthetic route involves the synthesis and functionalization of gibbsite nanoplates with silica shell, followed with the polymerization of NIPAm in the presence of the functionalized silica cores. Imaging techniques *e.g.* SEM and TEM have been used to study the size, shape and polydispersity of the hybrid particles and the bare core particles. Cryo-TEM microscopy reveals the core-shell morphology of the composites. Similar results have been obtained from cross-section analysis of AFM images of single hybrid microgels. The latter analysis shows clearly the incorporation of the solid cores within the soft microgels. In addition, all the hybrid particles show similar swelling-deswelling behavior as that of pure PNIPAm microgels

as a function of temperature. The analysis by DDLS shows that a rotational diffusion has been observed for the GS-MPS-PNIPAm microgels at 50 °C and the aspect ratio is calculated to be around 0.7, indicating that the hybrid microgels in the collapsed state still have an anisotropic shape.

In the last part, highly dispersible, monodispersed and mesoporous nitrogen-doped hollow carbon nanoplates have been synthesized with uniform hexagonal morphologies by using dopamine as carbon source and hexagonal gibbsite nanoplates as template via a silica nanocasting technique. The as-synthesized hollow carbon nanoplates contain a moderate specific surface area (460 $m^2 \cdot g^{-1}$) with highly accessible mesopores of uniform size (~3.8 nm). The nitrogen content of the hollow carbon nanoplates is as high as 7.2 wt%. HR-TEM, XRD, and Raman measurements indicate that the obtained hollow carbon nanoplates have been partially graphitic. Owing to the high nitrogen doping, superior dispersity and 2D mesoporous nanostructures, the hollow carbon nanoplates obtained by this approach have been applied as electrode materials in supercapacitors using poly(ionic liquid) nanoparticles as binder, which show high capacitance and excellent electrochemical stability.

In conclusion, this thesis provides a comprehensive investigation on the surface modification of gibbsite platelets with functional polymers, which is of great importance for the further work on designing hybrid anisotropic nanomaterials with well-defined novel structures. Such systems will be suitable for a variety of practical applications *e.g.,* organic pollutant degradation and energy storage.

8. Experimental

8.1 Chemicals

Aluminum isopropoxide (AIP), aluminum sec-butoxide (ASB), hydrochloric acid, tris(hydroxymethyl) aminomethane (Tris), 3-hydroxytyramine hydrochloride (Dopamine), hydrogen tetrachloroaurate hydrate ($HAuCl_4 \cdot 4H_2O$), poly(acrylic acid sodium salt) (Mw~5,100), trisodium citrate dihydrate, hexadecyltrimethylammonium bromide (CTAB), ascorbic acid, 4-nitrophenol (Nip), Rhodamine B (RhB), sodium borohydride ($NaBH_4$), potassium chloride (KCl), polyvinylpyrrolidone (PVP), tetraethyl orthosilicate (TEOS), 3-(trimethoxysilyl) propyl methacrylate (MPS), N-isopropylacrylamide (NIPAm), N,N'-methylenebis (acrylamide) (BIS), azobisisobutyronitrile **(**AIBN**)**, ammonium hydrogen difluoride (NH_4HF_2), lithium sulfate monohydrate, poly(vinylidene fluoride) (PVDF), 1-methyl-2-pyrrolidinone (NMP) and ethanol were obtained from Sigma-Aldrich and used as received. Potassium persulfate (KPS) was purchased from Fluka. Millipore water used was purified by reverse osmosis (MilliRo; Millipore) and ion exchange (MilliRo; Millipore).

Polyvinylimidazolium nanoparticle (termed as PIL) binders were supported by Yuan from MPIKG.[27] Typically, 1,3,5-tribromomethyl benzene was reacted with excess of 1-vinylimidazole to produce Br^- containing monomer which consists of three vinylimidazolium bromide units. The following polymerization of this monomer was then conducted to form Br^- containing polymer, which are nanoparticles of three dimensionally interconnected networks. The final product PIL nanoparticle binder was obtained by anion exchange to replace Br^- by bis(trifiuoromethane)sulfonimide (TFSI).

8.2 Synthesis

8.2.1 G-PDA-Au nanocomposites

8.2.1.1 Synthesis of gibbsite nanoparticles

Gibbsite platelets were synthesized from aluminum alkoxides according to the method reported by Wierenga *et al.*[31] In a typical experiment, 0.08 mol/L ASB and 0.08 mol/L AIP were dissolved in 1.5 L of deionized water which was acidified by 0.09 mol/L HCl (37%). After mechanically stirring for 10 days, the turbid mixture was heated in three polypropylene

bottles in a water bath at 85 °C for 3 days. The dispersion was dialyzed against deionized water in regenerated cellulose tubes (MWCO 14 000) and the Millipore water was changed twice a day. Dialysis was stopped until its conductivity did not significantly increase anymore. Finally, the colloidal dispersion was centrifuged (1200 g, 20 h) to remove the small gibbsite particles before further characterization and use. The sediment was redispersed in water. The dispersion was stored in a polypropylene bottle with gibbsite concentration of 4.0 wt%.

8.2.1.2 G-PDA core-shell nanoparticles

Negatively charged poly(acrylic acid sodium salt) (PAA-Na) was first coated onto the surface of gibbsite nanoplates, which aims to stabilize the gibbsite nanoplates and induce the depositon of PDA onto the particle surface. 100 mg gibbsite was added to a solution of 10 g/L PAA-Na. The mixture was vigorously stirred for 24 hours. The dispersion was washed by Tris buffer for 3 times. PDA shell was deposited onto the PAA-Na modified gibbsite particles by the oxidative self-polymerization of dopamine. Briefly, 100 mg PAA-Na stabilized gibbsite particles were added to a 0.5 mg/mL dopamine solution (200 mL, pH 8.5, 10 mM Tris buffer) under constant ultrasonification at 37 kHz (Elmasonic P120H, Elma Schmidbauer GmbH, Germany) for 3 h. The white suspension turned into black during the self-polymerization of dopamine. To obtain a thicker PDA shell, the reaction time was extended to 6 h or 9 h. The final product was then washed several times with deionized water until the supernatant remained colorless.

8.2.1.3 In-situ deposition of Au nanoparticles onto G-PDA nanoparticles

The G-PDA-Au nanocomposites were synthesized by in situ deposition of Au nanoparticles on the surface of G-PDA particles. Different experimental conditions were explored to synthesize G-PDA-Au nanocomposites following the recipe displayed in Table 8.2.1. In a typical run, G-PDA particles were added to an ice-cold and freshly prepared $HAuCl_4$ aqueous solution. The mixture was ultrasonificated for different reaction times (0.5 min, 4 min, 8 min), followed by centrifugation and washing with deionized water for three times. The G-PDA-Au nanocomposites were dispersed in 10 mL water for further use. The loading amount of Au was measured by TGA analysis.

Table 8.2.1 Specified recipe for the synthesis of G-PDA-Au nanocomposites.

No.	G-PDA (mg)	PDA thickness (nm)	Volume (mL)	c_{HAuCl4} (mM)	Reaction time (min)	Sample name
1	10	14	65	0.25	8	G-PDA-Au-2
2	10	14	65	0.1	8	
3	10	14	65	0.05	8	
4	10	14	65	0.1	4	G-PDA-Au-1
5	10	14	65	0.1	0.5	G-PDA-Au-3
6	10	8	65	0.1	4	G-PDA-Au-4

8.2.1.4 Fabrication of the recyclable nanocatalysts

Due to the strong adhesion behavior of PDA, the recyclable nanocatalysts were prepared by spin coating 30 μL of 1 wt% G-PDA-Au particle dispersion on a clean silicon wafer at low speed (500 rpm).

8.2.1.5 Synthesis of CTAB-stabilized Au nanoparticles

Au nanoparticles with radius around 5 nm were synthesized according to the seeds growing method.[287] Typically, the seeds solution was firstly synthesized by adding 0.6 mL of ice-cold, freshly prepared 0.1 M $NaBH_4$ solution into a 20 mL aqueous solution containing 2.5×10^{-4} M $HAuCl_4$ and 2.5×10^{-4} M trisodium citrate solution. The mixture was stirred for 2 h at room temperature. Then 10 mL of growth solution was prepared by mixing 2.5 mL of 1×10^{-3} M $HAuCl_4$ and 7.5 mL of 0.11 M CTAB solution. Afterwards, 7.5 mL of growth solution was mixed with 0.05 mL of freshly prepared 0.1 M ascorbic acid solution. 2.5 mL of seed solution was added under stirring. After 10 min's stirring, the solution turned to wine red. The Au nanoparticles were washed by centrifugation twice before catalytic reaction.

8.2.1.6 Catalytic reactions

For the catalytic decomposition of Nip, the catalytic measurements were performed in a 3 mL quartz cell using a Lambda 650 spectrometer from Perkin-Elmer. Before reaction, the stock solutions were purged with nitrogen to remove O_2. A given amount of G-PDA-Au particles was added to a freshly prepared mixture of Nip (0.11 mM, 4.5 mL) and $NaBH_4$ (0.1 M, 0.5 mL) in a glass vessel. The mixture was added quickly to the quartz cell, and placed in the spectrometer. The extinction of Nip was subsequently monitored at a constant pH value of 10

at λ = 400 nm.

For the catalytic decomposition of RhB, a given amount of G-PDA-Au particles was added to the freshly prepared mixture of RhB solution (28 μM, 4.5 mL) with $NaBH_4$ solution (0.1 M, 0.5 mL) in a glass vessel. The mixture was added quickly to the quartz cell, and placed in the spectrometer. The extinction of RhB was subsequently monitored at a constant pH value of 10 at λ = 554 nm.

8.2.2 Synthesis of GS-MPS-PNIPAm core-shell particles

8.2.2.1 Synthesis of silica coated gibbsite nanoparticles

The gibbsite was first coated with a thin layer of polyvinylpyrrolidone (PVP, 40,000 g/mol), which stabilizes the gibbsite and improves silica growth onto the particle surface. Typically, 25 g PVP40 was dissolved in 250 mL deionized water. 12.5 mL of a 40 g/L gibbsite dispersion was added to this viscous mixture. After vigorously stirring for 24 hours, the dispersion was centrifuged over night at 500 g, and the supernatant, which still looks slightly opaque, was removed. The sediment was redispersed in 100 mL ethanol by shaking and/or stirring for a few hours. This gibbsite-PVP dispersion was used for coating with silica within a day to limit desorption of the PVP.

Gibbsite particles with silica coating were prepared according to a modified Stöber method.[104] In a typical run, a Stöber mixture mixture was prepared by transferring the PVP stabilized gibbsite into a flask while stirring vigorously. 317 mL ethanol and 23 mL ammonia (25 %) were added to adjust the gibbsite and ammonia concentrations to 1.2 g/L and 5.5% (*v*/*v*), respectively. A large part of the ethanol was added in the first step, so as to avoid aggregation upon the addition of ammonia due to a high ionic strength. While vigorously stirring, 1.6 mL TEOS was added under the liquid surface of the Stöber mixture. After 6 h's reaction, another portion of 1.1 mL TEOS was added to obtain a thicker silica shell. The reaction was completed after 16 h.

8.2.2.2 Functionalization of gibbsite-silica core-shell particles with vinyl groups

To functionalize the silica coated gibbsite nanoparticles (GS), 8.4 mL 3-(trimethoxysilyl) propyl methacrylate (MPS) mixed with 20 mL ethanol was slowly added to the alkaline nanoparticle dispersion within 5 h. The mixture was left to react for 1 day and then boiled for

2 h at 80 ºC to ensure covalent bonding. The as-prepared MPS modified GS nanoparticles (GS-MPS) were cleaned by centrifugation several times and redispersed in ethanol.

8.2.2.3 GS-MPS-PNIPAm composite particles

The thermosensitive core-shell particles were synthesized by attaching a shell of PNIPAm network cross-linked by BIS onto the surface of GS-MPS cores through the seeded emulsion polymerization.[242] Different ratio between core particles and NIPAm was used for the synthesis of composite microgels following the recipe displayed in Table 8.2.2. In a typical run, GS-MPS core particles in ethanol solution were dispersed in poly(vinylpyrrolidone) (MW 10000, PVP) (5 mL, 3 wt%) aqueous solution under stirring. After 15 min, NIPAm and N, N'-methylene-bisacrylamide (BIS) (10 mol% of NIPAm) mixture dissolved in water (1 mL) was added inside. The solution was pre-heated to 35 ºC under a nitrogen atmosphere and kept stirring for 15 min. Thereafter, the temperature was raised to 70 ºC and the polymerization started by the addition of initiator (2.4 mg KPS dissolved in 1 mL water). The emulsion became turbid after 10 min and the polymerization lasted for 4 h at 70 ºC. The white and turbid solution was then cooled to room temperature. The composite particles were cleaned by centrifugation and redispersion in water several times.

Table 8.2.2 Specified recipe for the synthesis of GS-MPS-PNIPAm composite particles.

Sample name	m(core) [mg]	m(NIPA) [mg]	m(BIS) [mg]	m(KPS) [mg]	m(H_2O) [g]
GS-MPS-PNIPAm-1	20.4	61.2	8.5	2.4	7
GS-MPS-PNIPAm-2	20.4	48.9	6.8	2.4	7
GS-MPS-PNIPAm-3	20.4	38.8	5.4	2.4	7

8.2.3 Hollow Carbon nanoplates

8.2.3.1 Synthesis of hollow silica nanoplates

Gibbsite particles with a thin silica shell were firstly synthesized. 1 g PVP modified gibbsite particles were dispersed in 794 mL of ethanol by ultrasonification. 46 mL of ammonia (25 %) were added to adjust ammonia concentrations to 5.5% (*v*/*v*). While vigorously stirring, 1.5 mL TEOS was added under the surface of the mixture. After 6 h's reaction, the products were

washed twice with ethanol and three times with deionized water, and then redispersed in concentrated HCl (37 %) to remove the gibbsite cores. After stirring for 5 days, the purified hollow silica nanoplates were washed with deionized water until the pH was neutral.

8.2.3.2 Coating of hollow silica nanoplates with a PDA shell

A PDA shell was deposited onto hollow silica nanoplates by the oxidative self-polymerization of dopamine. 0.5 mg/mL hollow silica nanoplates were exposed to a 0.5 mg/mL dopamine solution in air at pH 8.5 in 10 mM tris(hydroxymethyl) aminomethane (TRIS) buffer under constant ultrasonification for 3 h. Then the PDA coated hollow silica nanoplates (HSP@PDA) were separated from the dispersions by centrifugation and washed with deionized water. This process was repeated until the supernatant remained colorless.

8.2.3.3 Synthesis of HSP@PDA@silica gel

The silica nanocasting process was realized as followings. 3 mL of 0.1 M HCl was added to 30 mL of HSP@PDA nanoparticles dispersion (40 g/L) under vigorous stirring. After 10 min of stirring ultrasonification, 22.5 mL TEOS were added in portions during 30 min under the surface of the vigorously stirred solution. The mixtures were stirred at room temperature overnight. After removing ethanol by rotary evaporation, the mixture was freeze-dried.

8.2.3.4 Synthesis of hollow carbon nanoplates

Carbonization was carried out under argon flow at 800 °C for 2 h (heating rate: 2 °C/min). The pyrolyzed products were treated by an aqueous solution of 4 M NH_4HF_2 to remove the silica. The desired products were obtained after careful cleaning.

8.2.3.5 Electrochemical measurements

The electrochemical measurements were conducted in a symmetrical two electrode cell. The electrodes were prepared by mixing the 80 wt% of the carbon samples, with 10 wt% of acetylene black as conductive additive and 10 wt% of PVDF or PIL as binder in NMP to form a homogeneous slurry. Afterwards, the slurry was coated onto stainless steel foil (1.44 cm^2) and dried overnight in a vacuum oven at 60 °C to remove the solvent. The mass loading was typically 1 mg/cm^2. The capacitor was realized by sandwiching a porous glass microfiber membrane GF/A between two electrodes, using 1 M Li_2SO_4 aqueous solution as electrolytes.

All electrochemical measurements were carried out using a Biologic MPG-2 potentiostat/galvanostat. Cyclic voltammetry (CV) was performed between different potential windows and then at various scan rates in the potential window of 0.0–1.4 V. The specific capacitance (C_{sp}) is calculated from the slope of the charge-discharge curves using the following equations:[288]

$$C(F) = \frac{i}{\Delta V/\Delta t}$$

$$C_{sp}(F.g^{-1}) = \frac{4C}{m}$$

where i is the applied current in ampere (A), $\Delta V/\Delta t$ the slope of the discharge curve in seconds (s) and m the mass in gram (g) of both electrodes. C is the calculated capacitance in Farad (F).

The specific energy density E and power density P can be obtained according to the following equations:[74]

$$E(Wh \cdot kg^{-1}) = \frac{1}{2}\frac{C}{m}V^2\frac{1}{3.6}$$

$$P(\mathrm{W} \cdot kg^{-1}) = \frac{E}{t}$$

where V is the cell voltage after ohmic drop (V) and t is the discharge time (h).

8.3 Characterization

8.3.1 Imaging techniques

8.3.1.1 Transmission electron microscopy (TEM)

The morphology of the as-synthesized particles was characterized by TEM. Carbon-coated copper TEM grids (200 mesh, Science Services, Munich, Germany) were pretreated for 10 seconds with glow discharge. TEM specimens were prepared by dropping approximately 5 µL of a 0.05 wt% dispersion on a TEM copper grid and left in air to dry. The specimen was inserted into the sample holder (EM21010, JEOL GmbH, Eching, Germany) and transferred to a JEOL JEM-2100 with a LaB6cathode (JEOL GmbH, Eching, Germany). All images were recorded digitally by a bottom-mounted 4k CMOS camera system (TemCam-F416, TVIPS,

Gauting, Germany) at an acceleration voltage 200 kV, and proceeded with a digital imaging processing system (EM-Menu 4.0, TVIPS, Gauting, Germany).

Cryo-TEM was used to visualize the morphology of the microgel particles in situ. For the sample preparation, 5 µL of the sample dispersion (~0.5 wt%) was dropped on a lacey carbon-coated copper TEM grid (200 mesh, Science Services, Munich, Germany), where most of the liquid was removed with blotting paper, leaving a thin film stretched over the grid holes. The specimens were instantly shock vitrified by rapid immersion into liquid ethane at its freezing point and cooled to approximately 90 K by liquid nitrogen in a temperature controlled freezing unit (Zeiss Cryobox, Zeiss NTS GmbH, Oberkochen, Germany). The temperature was monitored and kept constant in the chamber during all the preparation steps. After freezing the sample, it was inserted into a cryo-transfer holder (CT3500, Gatan, Munich, Germany) and transferred to a Zeiss EM922 EFTEM. Measurements were carried out at temperatures around 90 K. The specimen was imaged at 200 kV using a JEOL JEM-2100 equipped with a bottom-mounted 4×4k CMOS camera (TemCam-F416, TVIPS). Saturation effects were avoided by keeping the intensity below 15000. The histograms of the micrographs were adjusted by using the free software package Image J.

8.3.1.2 Scanning electron microscopy (SEM) and energy-dispersive X-ray spectroscopy (EDX)

SEM and EDX measurements were performed on a LEO GEMINI 1530 scanning electron microscope equipped with a Thermo Fisher Scientic X-ray silicon drift detector. The electron high tension was set to 3 keV. The samples were prepared by dropping a few µL of diluted aqueous dispersions (0.01 wt%) on silicon surface and left in air to dry.

8.3.1.3 Atomic force microscopy (AFM)

The samples were prepared by drop-casting a few µL of aqueous dispersions on 1 cm^2 piece of silicon wafer. AFM investigations were performed on a multimode atomic force microscope (JPK instruments, Nanowizard II). Height profiles were recorded in tapping mode at room temperature and against air. Silicon nitride cantilevers (PNP TR tips) were used with a chromium-gold coating ($k \approx 0.08$ N/m, $f0 \approx 17$ kHz; Nanoworld Innovative technologies), and exhibited a pyramidal tip-shape with the maximum opening angle of 35°. Images were edited with NanoWizard IP Version 3.3a (JPK instruments).

8.3.2 Spectroscopic characterizations

8.3.2.1 UV-Vis spectroscopy

The UV-Vis spectra were measured by Lambda 650 spectrometer supplied by Perkin-Elmer. Thereby, the visible spectra between 315 and 900 nm is generated by a tungsten-halogen-lamp, whereas the UV-range originates from a deuterium lamp. The sample environment is thermo-regulated by a thermostat (Julabo F30-C). For each series of measurements, the absorption of distilled water is measured and subtracted from each measurement. For the measurement, the solutions were mixed and placed in a Spectrosil® quartz glass cuvette (190 - 2700 nm, Roth). Immediately the extinction was recorded by the program: PerkinElmer WinLab, with respect to the measurement time. The concentration of the educt arises from the extinction by the Lambert-Beer-law.

$$E(\lambda) = \lg \frac{I_0}{I} = \varepsilon(\lambda) \cdot c \cdot d$$

With $E(\lambda)$ is the extinction, I_0 is the Intensity of the incoming light, I is the intensity of the outgoing light, $\varepsilon(\lambda)$ is the extinctions coefficient, c is the concentration of the educt and d is the thickness of the cuvette.

8.3.2.2 Fourier transform infrared (FTIR) spectroscopy

IR spectra were recorded on KBr pellets on a Nicolet 5SXC FTIR Interferometer.

8.3.2.3 Raman spectroscopy

Raman spectrum was collected using a confocal Raman microscope (α300; WITec, Ulm, Germany) equipped with a 532 nm laser.

8.3.2.4 Hard x-ray photoelectron spectroscopy (HAXPES)

XPS is a surface sensitive technique for characterizing the chemical composition and oxidative state of an element via its binding energy. The samples were prepared by drop-casting a few µL of aqueous dispersions on 1 cm^2 piece of Al foil. HAXPES measurements were conducted at the High Kinetic Energy Spectrometer (HiKE) endstation located at the KMC-1 beamline of the BESSY II light source.[289,290] A 2 keV excitation energy and a VG SCIENTA R4000 electron analyzer were used for these measurements. For energy

calibration, a clean Au foil was measured and the binding energy (BE) of the Au $4f_{7/2}$ core level was set to 84.00 eV.[291]

8.3.3 Light scattering and Zeta-potential measurements

8.3.3.1 (Depolarized) dynamic light scattering to determine D_T and D_R

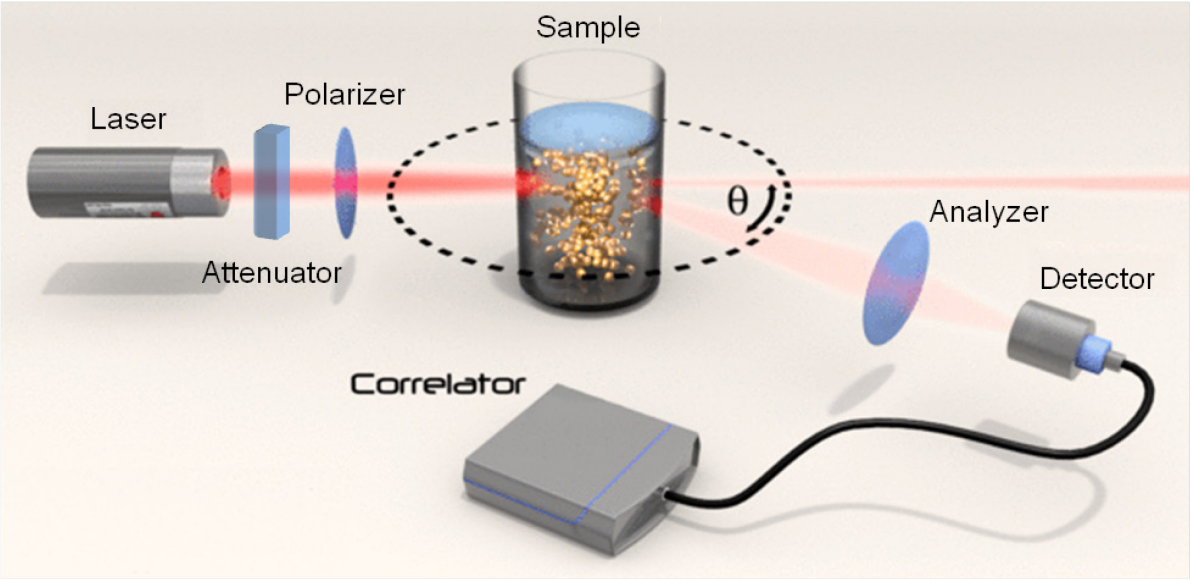

Figure 8.3.1 Schematic figure of the ALV-4000 compact goniometer system. Laser light passes an automated attenuator and a vertical polarizer. The light scatters at the colloidal dispersion and passes a horizontal analyzer (only in DDLS) to be detected at an avalanche photo diode (APD). The intensity fluctuations are measured over different scattering vectors by changing the scattering angle θ with a goniometer.

The light scattering experiments were performed on an ALV-4000 compact goniometer system equipped with a 35 mV He-Ne laser (λ = 632.8 nm). The schematic setup is shown in Figure 8.3.1. The laser passes an automatic attenuator and a vertical polarizer (Glan-Thompson prism, extinction ratio 10^4:1) before the light is scattered at the sample dispersion. In the sample cell, toluene is used as index matching substance and the temperature is controlled by a thermostat (Rotilabo, ± 0.1 ºC). For dynamic light scattering (DLS) measurements, no analyzer is used. For depolarized dynamic light scattering (DDLS) measurements, the analyzer (Glan-Thompson prism, extinction ratio 10^6:1) is set to 90° perpendicular to the polarizer. The signal is recorded with an avalanche photo diode (APD).

When light encounters small particles, it is scattered elastic in all directions. If coherent and monochromatic light is used, the scattered light of different particles interferes with each other, leading to intensity fluctuations, which are related to the Brownian motion of the

particles.[292] Analysis of the fluctuation of the scattered light yields the diffusion coefficients of the colloidal dispersion. In a DLS experiment, the intensity fluctuations are measured and correlated with each other. The translational diffusion coefficient (D^T) is obtained from $\Gamma = D^T \cdot q^2$. In DDLS, the autocorrelation function depends on D^T and the rotational diffusion coefficient (D^R) for anisotropic particles. The decay rate Γ is now given as: $\Gamma = D^T \cdot q^2 + 6D^R$. Upon plotting Γ versus q^2, the value of $6D^R$ can be obtained directly by extrapolation of $q^2 \rightarrow 0$ and D^T by the slope of the curve (Figure 8.3.2).

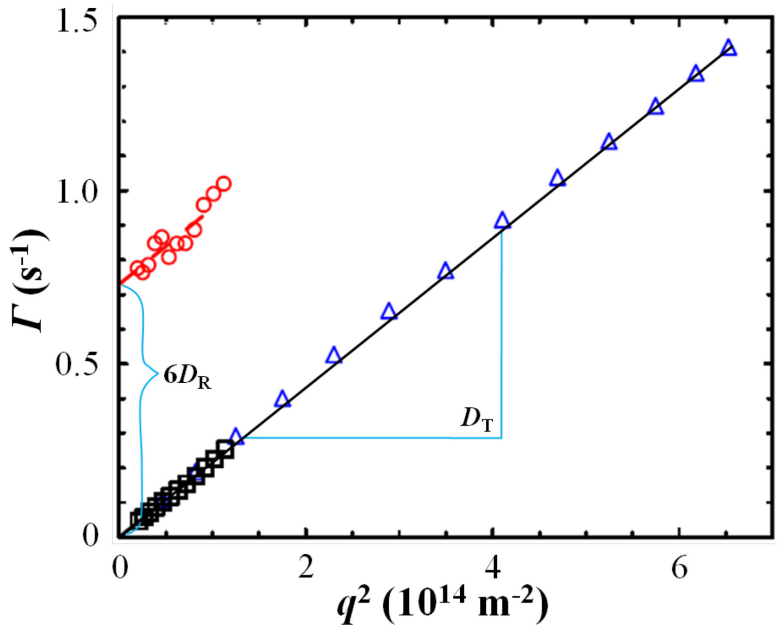

Figure 8.3.2 Exemplary fits of the relaxation rate versus q^2 to determine D^T and D^R from a DLS (blue open triangle) and DDLS (black open square for slow mode and red open circle for fast mode) experiment.

The samples were prepared in the dust-free fume hood. A 0.005 wt% dispersion of microgel particles was filtered with a 1.2 µm syringe filter to avoid aggregations or impurities. Afterwards, the dispersion was transferred into a dust free quartz glass cuvettes. All the DLS measurements were performed at scattering angles between 20° and 40° with steps of 1°, in steps of 10° in the angular range from 40° to 140°. For DDLS measurements, three runs per angle were set and averaged with an angular step of 1° for scattering angles between 20° and 40°. Prior to measurements, the dispersion was left for 20 min to attain the temperature equilibrium. The light scattering data were analyzed according to the cumulant analysis method.

8.3.3.2 Zeta-potential measurements

Zeta-potential measurements have been conducted with a Zetasizer (Nano-ZS) from Malvern Instruments. The cuvette that has been used (Malvern disposable folded capillary cell, DTS1070) was washed with ethanol and water, dedusted and filled with 1 ml of an approximately 0.01 wt% dispersion in 0.001 M KCl solution. The scattering angle has been fixed at 17° with a laser wavelength of 532 nm.

8.3.4 X-ray powder diffraction (XRD)

XRD analyzes the structure of a crystal via diffraction of an incident beam at the regularly ordered atom lattice. XRD studies of the samples (XRD, Bruker D8) were carried out by using a monochromatized X-ray beam with Cu Kα radiation with 0.05°/min scan rate. The diffraction pattern was scanned over the range 10 to 90 degree (2θ).

8.3.5 Thermogravimetric analysis (TGA)

TGA is a method to analyze physical and chemical properties of materials with constant heating rate. Processes like phase transitions, chemisorptions, desolvation, or decomposition can be monitored as a function of the temperature. Such processes can be followed by measuring the change in mass in respect to the temperature. A high precision balance and well controlled furnace are needed. TGA experiments were accomplished on a Netsch STA 409PC LUXX® under a continuous air stream. 10 mg of the dried samples were filled in the crucible which was then inserted in the chamber. The samples were heated to 1000 °C at a heating rate of 10 K min^{-1}, and then hold at this temperature for one hour. In case of the G-PDA-Au composite particles, the weight loss was attributed to the polymer and the dehydration of gibbsite particles. Pure carbon samples (HCPs) were tested and showed a weight loss of 100 %.

8.3.6 Nitrogen sorption

Quantachrome Autosorb-1 instrument was used for the measurement of nitrogen adsorption/desorption isotherms at 77 K. Before measurements, the sample was outgassed at 100 ˚C for 18 h under vacuum. The specific surface areas and pore size distribution of the sample were calculated using the Brunauer-Emmett-Teller (BET) equation and the Barrett-Joyner-Halenda (BJH) method, respectively.

8.3.7 Elemental analysis

Elemental analysis is a process where a sample of some material is analyzed for its elemental and sometimes isotopic composition. The contents of carbon, hydrogen and nitrogen in hollow carbon nanoplates were determined by combustion analysis using a Vario Micro device.

Bibliography

(1) Morones, J. R.; Elichiguerra, J. L.; Camacho, A.; Holt, K.; Kouri, J. B.; Ramirez, J. T.; Yacaman, M. J. The Bactericidal Effect of Silver Nanoparticles. *Nanotechnology* **2005**, *16*, 2346–2353.

(2) Rao, C. N. R.; Cheetham, a K. Science and Technology of Nanomaterials: Current Status and Future Prospects. *J. Mater. Chem.* **2010**, *11*, 2887–2894.

(3) Roduner, E. Size Matters: Why Nanomaterials Are Different. *Chem. Soc. Rev.* **2006**, *35*, 583–592.

(4) Jain, P. K.; Huang, X.; EL-Sayed, I. H.; El-Sayed, M. Noble Metals on the Nanoscale: Optical and Photothermal Properties and Some Applications in Imaging, Sensing, Biology, and Medicine. *Acc. Chem. Res.* **2008**, *14*, 1578–1586.

(5) Schwartzberg, A. M.; Zhang, J. Z. Novel Optical Properties and Emerging Applications of Metal Nanostructures. *J. Phys. Chem. C* **2008**, *112*, 10323–10337.

(6) Zhou, Z.-Y.; Tian, N.; Li, J.-T.; Broadwell, I.; Sun, S.-G. Nanomaterials of High Surface Energy with Exceptional Properties in Catalysis and Energy Storage. *Chem. Soc. Rev.* **2011**, *40*, 4167–4185.

(7) Teoh, W. Y.; Scott, J. A.; Amal, R. Progress in Heterogeneous Photocatalysis: From Classical Radical Chemistry to Engineering Nanomaterials and Solar Reactors. *J. Phys. Chem. Lett.* **2012**, *3*, 629–639.

(8) Jariwala, D.; Sangwan, V. K.; Lauhon, L. J.; Marks, T. J.; Hersam, M. C. Carbon Nanomaterials for Electronics, Optoelectronics, Photovoltaics, and Sensing. *Chem. Soc. Rev.* **2013**, *42*, 2824–2860.

(9) Yang, X.; Yang, M.; Pang, B.; Vara, M.; Xia, Y. Gold Nanomaterials at Work in Biomedicine. *Chem. Rev.* **2015**, *115*, 10410–10488.

(10) Sajanlal, P. R.; Sreeprasad, T. S.; Samal, A. K.; Pradeep, T. Anisotropic Nanomaterials: Structure, Growth, Assembly, and Functions. *Nano Rev.* **2011**, *2*, 4.

(11) Burda, C.; Chen, X.; Narayanan, R.; El-Sayed, M. A. Chemistry and Properties of Nanocrystals of Different Shapes. *Chem. Rev.* **2005**, *105*, 1025–1102.

(12) Ray, P. Size and Shape Dependent Second Order Nonlinear Optical Properties of Nanomaterials and Their Application in Biological and Chemical Sensing. *Chem. Rev.* **2010**, *110*, 5332–5365.

(13) Patzke, G. R.; Krumeich, F.; Nesper, R. Oxidic Nanotubes and Nanorods-Anisotropic Modules for a Future Nanotechnology. *Angew. Chem. Int. Ed.* **2002**, *41*, 2446–2461.

(14) Murphy, C. J.; Sau, T. K.; Gole, A. M.; Orendorff, C. J.; Gao, J.; Gou, L.; Hunyadi, S. E.; Li, T. Anisotropic Metal Nanoparticles: Synthesis, Assembly, and Optical Applications. *J. Phys. Chem. B* **2005**, *109*, 13857–13870.

(15) Marzán, L. M. L. (Non-Carbon) Anisotropic Nanomaterials. *J. Mater. Chem.* **2006**, *16*, 3891–3892.

(16) Kunz, D. A.; Schmid, J.; Feicht, P.; Erath, J.; Fery, A.; Breu, J. Clay-Based Nanocomposite Coating for Flexible Optoelectronics Applying Commercial Polymers. *ACS Nano* **2013**, *7*, 4275–4280.

(17) Pradhan, M.; Sarkar, S.; Sinha, A. K.; Basu, M.; Pal, T. Morphology Controlled Uranium Oxide Hydroxide Hydrate for Catalysis, Luminescence and SERS Studies. *CrystEngComm* **2011**, *13*, 2878–2889.

(18) Yen, Y. Y.; Wang, H. T.; Guo, W. J. Synergistic Effect of Aluminum Hydroxide and Nanoclay on Flame Retardancy and Mechanical Properties of EPDM Composites. *J. Appl. Polym. Sci.* **2013**, *130*, 2042–2048.

(19) Goldberg, S. Competitive Adsorption of Molybdenum in the Presence of Phosphorus or Sulfur on Gibbsite. *Soil Sci.* **2010**, *175*, 105–110.

(20) Huittinen, N.; Rabung, T.; Lützenkirchen, J.; Mitchell, S. C.; Bickmore, B. R.; Lehto, J.; Geckeis, H. Sorption of Cm(III) and Gd(III) onto Gibbsite, α-$Al(OH)_3$: A Batch and TRLFS Study. *J. Colloid Interface Sci.* **2009**, *332*, 158–164.

(21) van der Kooij, F. M.; Lekkerkerker, H. N. W. Formation of Nematic Liquid Crystals in Suspensions of Hard Colloidal Platelets. *J. Phys. Chem. B* **1998**, *102*, 7829–7832.

(22) van der Kooij, F. M.; Kassapidou, K.; Lekkerkerker, H. N. W. Liquid Crystal Phase Transitions in Suspensions of Polydisperse Plate-like Particles. *Nature* **2000**, *406*, 868–871.

(23) Saalfeld, H.; Wedde, M. Refinement of the Crystal Structure of a. *Zeitschrift für Krist.* **1974**, *139*, 129–135.

(24) Besserguenev, A. V.; Fogg, A. M.; Francis, R. J.; Price, S. J.; O'Hare, D. Synthesis and Structure of the Gibbsite Intercalation Compounds $[LiAl_2(OH)_6]X$ {X = Cl, Br, NO_3} and $[LiAl_2(OH)_6]Cl{\cdot}H_2O$ Using Synchrotron X-Ray and Neutron Powder Diffraction. *Chem. Mater.* **1997**, *9*, 241–247.

(25) Hind, A. R.; Bhargava, S. K.; Grocott, S. C. The Surface Chemistry of Bayer Process Solids: A Review. *Colloids Surfaces A Physicochem. Eng. Asp.* **1999**, *146*, 359–374.

(26) Sweegers, C.; Enckevort, W. J. P. Van; Meekes, H.; Bennema, P.; Hiralal, I. D. K.; Rijkeboer, A. The Impact of Twinning on the Morphology of γ-$Al(OH)_3$ Crystals. *J. Cryst. Growth* **1999**, *197*, 244–253.

(27) Sweegers, C.; De Coninck, H. C.; Meekes, H.; Van Enckevort, W. J. P.; Hiralal, I. D. K.; Rijkeboer, A. Morphology, Evolution and Other Characteristics of Gibbsite Crystals Grown from Pure and Impure Aqueous Sodium Aluminate Solutions. *J. Cryst. Growth* **2001**, *233*, 567–582.

(28) Liu, Y.; Ma, D.; Blackley, R. A.; Zhou, W.; Han, X.; Bao, X. Synthesis and Characterization of Gibbsite Nanostructures. *J. Phys. Chem. C* **2008**, *112*, 4124–4128.

(29) Phambu, N.; Humbert, B.; Burneau, A. Relation between the Infrared Spectra and the Lateral Specific Surface Areas of Gibbsite Samples. *Langmuir* **2000**, *16*, 6200–6207.

(30) Philipse, A. P.; Nechifor, A.-M.; Patmamanoharan, C. Isotropic and Birefringent Dispersions of Surface Modified Silica Rods with a Boehmite-Needle Core. *Langmuir* **1994**, *10*, 4451–4458.

(31) Wierenga, A. M.; Lenstra, T. A. J.; Philipse, A. P. Aqueous Dispersions of Colloidal Gibbsite Platelets: Synthesis, Characterisation and Intrinsic Viscosity Measurements Anieke. *Colloid Surf. A* **1998**, *134*, 359–371.

(32) Wijnhoven, J. E. G. J. Seeded Growth of Monodisperse Gibbsite Platelets to Adjustable Sizes. *J. Colloid Interface Sci.* **2005**, *292*, 403–409.

(33) Rosenqvist, J.; Persson, P.; Sjoberg, S. Protonation and Charging of Nanosized Gibbsite ($Al(OH)_3$) Particles in Aqueous Suspension Protonation and Charging of Nanosized Gibbsite (a-$Al(OH)_3$) Particles in Aqueous Suspension. *Langmuir* **2002**, *18*, 4598–4604.

(34) Van Beek, D. Der; Radstake, P. B.; Petukhov, A. V.; Lekkerkerker, H. N. W. Fast Formation of Opal-like Columnar Colloidal Crystals. *Langmuir* **2007**, *23*, 11343–11346.

(35) Veerman, J. A. C.; Frenkel, D. Phase Behavior of Disklike Hard-Core Mesogens. *Phys. Rev. A* **1992**, *45*, 5632.

(36) Kleshchanok, D.; Holmqvist, P.; Meijer, J. M.; Lekkerkerker, H. N. W. Lyotropic Smectic B Phase Formed in Suspensions of Charged Colloidal Platelets. *J. Am. Chem. Soc.* **2012**, *134*, 5985–5990.

(37) Mourad, M. C. D.; Byelov, D. V; Petukhov, A. V; de Winter, D. A. M.; Verkleij, A. J.; Lekkerkerker, H. N. W. Sol-Gel Transitions and Liquid Crystal Phase Transitions in Concentrated Aqueous Suspensions of Colloidal Gibbsite Platelets. *J. Phys. Chem. B* **2009**, *113*, 11604–11613.

(38) Mourad, M. C. D.; Petukhov, A. V.; Vroege, G. J.; Lekkerkerker, H. N. W. Lyotropic Hexagonal Columnar Liquid Crystals of Large Colloidal Gibbsite Platelets. *Langmuir* **2010**, *26*, 14182–14187.

(39) Rong, M. Z.; Zhang, M. Q.; Ruan, W. H. Surface Modification of Nanoscale Fillers for Improving Properties of Polymer Nanocomposites: A Review. *Mater. Sci. Technol.* **2006**, *22*, 787–796.

(40) Kango, S.; Kalia, S.; Celli, A.; Njuguna, J.; Habibi, Y.; Kumar, R. Surface Modification of Inorganic Nanoparticles for Development of Organic-Inorganic Nanocomposites-A Review. *Prog. Polym. Sci.* **2013**, *38*, 1232–1261.

(41) Faucheua, J.; Gauthiera, C.; Chazeaua, L.; Cavailléa, J.-Y.; Mellonb, V.; Lamib, E. B. Miniemulsion Polymerization for Synthesis of Structured Clay/polymer Nanocomposites: Short Review and Recent Advances. *Polymer* **2010**, *51*, 6–17.

(42) Lim, Y. T.; Park, O. O. Phase Morphology and Rheological Behavior of

Polymer/layered Silicate Nanocomposites. *Rheol. Acta* **2001**, *40*, 220–229.

(43) Blumstein, A. Polymerization of Adsorbed Monolayers. *J. Polym. Sci. Part A Polym. Chem.* **1965**, *3*, 2653–2664.

(44) Okada, A.; Usuki, A. Twenty Years of Polymer-Clay Nanocomposites. *Macromol. Mater. Eng.* **2006**, *291*, 1449–1476.

(45) Giannelis, E. P.; Krishnamoorti, R.; Manias, E. Polymer-Silicate Nanocomposites: Model Systems for Confined Polymers and Polymer Brushes. *Polymer* **1999**, 107–147.

(46) Biswas, M.; Ray, S. S. Recent Progress in Synthesis and Evaluation of Polymer-Montmorillonite Nanocomposites. *Adv. Polym. Sci.* **2001**, 167–221.

(47) Beyer, F. L.; Tan, N. C. B.; Dasgupta, A.; Galvin, M. E. Polymer-Layered Silicate Nanocomposites from Model Surfactants. *Chem. Mater.* **2002**, *14*, 2983–2988.

(48) Huang, X.; Brittain W., J. Synthesis and Characterization of PMMA Coated Magnetite Nanocomposites by Emulsion Polymerization. *Macromolecules* **2001**, *34*, 3255–3260.

(49) Zu Putlitz, B.; Landfester, K.; Fischer, H.; Antonietti, M. The Generation Of "armored Latexes" and Hollow Inorganic Shells Made of Clay Sheets by Templating Cationic Miniemulsions and Latexes. *Adv. Mater.* **2001**, *13*, 500–503.

(50) Cauvin, S.; Colver, P. J.; Bon, S. A. F. Pickering Stabilized Miniemulsion Polymerization: Preparation of Clay Armored Latexes. *Macromolecules* **2005**, *38*, 7887–7889.

(51) Herrera, N. N.; Letoffe, J.-M.; Putaux, J.-L.; David, L.; Bourgeat-Lami, E. Aqueous Dispersions of Silane-Functionalized Laponite Clay Platelets. A First Step toward the Elaboration of Water-Based Polymer/Clay Nanocomposites. *Langmuir* **2004**, *20*, 1564–1571.

(52) Voorn, D. J.; Ming, W.; Van Herk, A. M. Clay Platelets Encapsulated Inside Latex Particles. *Macromolecules* **2006**, *39*, 4654–4656.

(53) Bourgeat-Lami, E. Organic-Inorganic Nanostructured Colloids. *J. Nanosci. Nanotechnol.* **2002**, *2*, 1–24.

(54) Ali, S. I.; Heuts, J. P. A.; Hawkett, B. S.; van Herk, A. M. Polymer Encapsulated Gibbsite Nanoparticles: Efficient Preparation of Anisotropic Composite Latex Particles by RAFT-Based Starved Feed Emulsion Polymerization. *Langmuir* **2009**, *25*, 10523–10533.

(55) Voorn, D. J.; Ming, W.; Van Herk, A. M. Encapsulation of Platelets by Physical and Chemical Approaches. *Macromol. Symp.* **2006**, *245-246*, 584–590.

(56) Zhang, A.; Neumeyer, J. L.; Baldessarini, R. J. Recent Progress in Development of Dopamine Receptor Subtype-Selective Agents: Potential Therapeutics for Neurological and Psychiatric Disorders. *Chem. Rev.* **2007**, *107*, 274–302.

(57) Lee, H.; Dellatore, S. M.; Miller, W. M.; Messersmith, P. B. Mussel-Inspired Surface Chemistry for Multifunctional Coatings. *Science* **2007**, *318*, 426–430.

(58) Zhou, J.; Duan, B.; Fang, Z.; Song, J.; Wang, C.; Messersmith, P. B.; Duan, H. Interfacial Assembly of Mussel-Inspired Au@ag@Polydopamine Core-Shell Nanoparticles for Recyclable Nanocatalysts. *Adv. Mater.* **2014**, *26*, 701–705.

(59) Liu, R.; Mahurin, S. M.; Li, C.; Unocic, R. R.; Idrobo, J. C.; Gao, H.; Pennycook, S. J.; Dai, S. Dopamine as a Carbon Source: The Controlled Synthesis of Hollow Carbon Spheres and Yolk-Structured Carbon Nanocomposites. *Angew. Chem. Int. Ed.* **2011**, *50*, 6799–6802.

(60) Liu, Q.; Yu, B.; Ye, W.; Zhou, F. Highly Selective Uptake and Release of Charged Molecules by pH-Responsive Polydopamine Microcapsules. *Macromol. Biosci.* **2011**, *11*, 1227–1234.

(61) Zeng, T.; Zhang, X. Le; Niu, H. Y.; Ma, Y. R.; Li, W. H.; Cai, Y. Q. In Situ Growth of Gold Nanoparticles onto Polydopamine-Encapsulated Magnetic Microspheres for Catalytic Reduction of Nitrobenzene. *Appl. Catal. B Environ.* **2013**, *134-135*, 26–33.

(62) Jiang, H.; Sun, T.; Li, C.; Ma, J. Peapod-like Nickel@mesoporous Carbon Core-Shell Nanowires: A Novel Electrode Material for Supercapacitors. *RSC Adv.* **2011**, *1*, 954–957.

(63) Liu, X.-C.; Wang, G.-C.; Liang, R.-P.; Shi, L.; Qiu, J.-D. Environment-Friendly Facile Synthesis of Pt Nanoparticles Supported on Polydopamine Modified Carbon Materials. *J. Mater. Chem. A* **2013**, *1*, 3945.

(64) Jiang, H.; Zhao, T.; Li, C.; Ma, J. Functional Mesoporous Carbon Nanotubes and Their Integration in Situ with Metal Nanocrystals for Enhanced Electrochemical Performances. *Chem. Commun.* **2011**, *47*, 8590–8592.

(65) Guo, L.; Liu, Q.; Li, G.; Shi, J.; Liu, J.; Wang, T.; Jiang, G. A Mussel-Inspired Polydopamine Coating as a Versatile Platform for the in Situ Synthesis of Graphene-Based Nanocomposites. *Nanoscale* **2013**, *1*, 3945–3953.

(66) Fan, X.; Yu, C.; Yang, J.; Ling, Z.; Hu, C.; Zhang, M.; Qiu, J. A Layered-Nanospace-Confinement Strategy for the Synthesis of Two-Dimensional Porous Carbon Nanosheets for High-Rate Performance Supercapacitors. *Adv. Energy Mater.* **2015**, *5*, 1–7.

(67) Han, F.; Li, W. C.; Lei, C.; He, B.; Oshida, K.; Lu, A. H. Selective Formation of Carbon-Coated, Metastable Amorphous $ZnSnO_3$ Nanocubes Containing Mesopores for Use as High-Capacity Lithium-Ion Battery. *Small* **2014**, *10*, 2637–2644.

(68) Liu, Y.; Ai, K.; Lu, L. Polydopamine and Its Derivative Materials: Synthesis and Promising Applications in Energy, Environmental, and Biomedical Fields. *Chem. Rev.* **2014**, *114*, 5057–5115.

(69) Zhang, M.; He, X.; Chen, L.; Zhang, Y. Preparation of IDA-Cu Functionalized Core-Satellite Fe_3O_4/polydopamine/Au Magnetic Nanocomposites and Their Application for Depletion of Abundant Protein in Bovine Blood. *J. Mater. Chem.* **2010**, *20*, 10696–10704.

(70) Xie, Y.; Yan, B.; Xu, H.; Chen, J.; Liu, Q.; Deng, Y.; Zeng, H. Highly Regenerable Mussel-Inspired Fe_3O_4@Polydopamine-Ag Core-Shell Microspheres as Catalyst and Adsorbent for Methylene Blue Removal. *ACS Appl. Mater. Interfaces* **2014**, *6*, 8845–8852.

(71) Fei, B.; Qian, B.; Yang, Z.; Wang, R.; Liu, W. C.; Mak, C. L.; Xin, J. H. Coating Carbon Nanotubes by Spontaneous Oxidative Polymerization of Dopamine. *Carbon* **2008**, *46*, 1795–1797.

(72) Kong, J.; Ismail, S.; Shahabadi, S.; Lu, X. Integration of Inorganic Nanostructures with Polydopamine-Derived Carbon: Tunable Morphologies and Versatile Applications. *Nanoscale* **2016**, *8*, 1770–1788.

(73) Dai, Y.; Jiang, H.; Hu, Y.; Fu, Y.; Li, C. Controlled Synthesis of Ultrathin Hollow Mesoporous Carbon Nanospheres for Supercapacitor Applications. *Ind. Eng. Chem. Res.* **2014**, *53*, 3125–3130.

(74) Fan, X.; Yu, C.; Yang, J.; Ling, Z.; Hu, C.; Zhang, M.; Qiu, J. A Layered-Nanospace-Confinement Strategy for the Synthesis of Two-Dimensional Porous Carbon Nanosheets for High-Rate Performance Supercapacitors. *Adv. Energy Mater.* **2015**, *5*, 1401761.

(75) Yun, Y. S.; Cho, S. Y.; Shim, J.; Kim, B. H.; Chang, S. J.; Baek, S. J.; Huh, Y. S.; Tak, Y.; Park, Y. W.; Park, S.; *et al.* Microporous Carbon Nanoplates from Regenerated Silk Proteins for Supercapacitors. *Adv. Mater.* **2013**, *25*, 1993–1998.

(76) Wu, Y. H.; Yu, T.; Shen, Z. X. Two-Dimensional Carbon Nanostructures: Fundamental Properties, Synthesis, Characterization, and Potential Applications. *J. Appl. Phys.* **2010**, *108*, 071301.

(77) Peng, X.; Peng, L.; Wu, C.; Xie, Y. Two Dimensional Nanomaterials for Flexible Supercapacitors. *Chem. Soc. Rev.* **2014**, *43*, 3303–3323.

(78) Ward, M. A.; Georgiou, T. K. Thermoresponsive Polymers for Biomedical Applications. *Polymers* **2011**, *3*, 1215–1242.

(79) Gandhi, A.; Paul, A.; Sen, S. O.; Sen, K. K. Studies on Thermoresponsive Polymers: Phase Behavior, Drug Delivery and Biomedical Applications. *Asian J. Pharm. Sci.* **2015**, *10*, 99–107.

(80) Lyon, L. A.; Meng, Z.; Singh, N.; Sorrell, C. D.; St. John, A. Thermoresponsive Microgel-Based Materials. *Chem. Soc. Rev.* **2009**, *38*, 865.

(81) Ramos, J.; Imaz, A.; Forcada, J. Temperature-Sensitive Nanogels: poly(N-Vinylcaprolactam) versus poly(N-Isopropylacrylamide). *Polym. Chem.* **2012**, *3*, 852.

(82) Clarke, K. C.; Lyon, L. A. Modulation of the Deswelling Temperature of Thermoresponsive Microgel Films. *Langmuir* **2013**, *29*, 12852–12857.

(83) Nayak, S.; Gan, D.; Serpe, M. J.; Lyon, L. A. Hollow Thermoresponsive Microgels. *Small* **2005**, *1*, 416–421.

(84) Heskins, M.; Guillet, J. E. Solution Properties of Poly(N-Isopropylacrylamide). *J. Macromol. Sci.* **1968**, *2*, 1441–1455.

(85) Pelton, R. H.; Chibante, P. Preparation of Aqueous Latices with N-Isopropylacrylamide. *Colloids and Surfaces* **1986**, *20*, 247–256.

(86) Karg, M.; Pastoriza-Santo, I.; Liz-Marzán, L. M.; Hellweg, T. A Versatile Approach for the Preparation of Thermosensitive PNIPAM Core-Shell Microgels with Nanoparticle Cores. *ChemPhysChem* **2006**, *7*, 2298–2301.

(87) Lu, Y.; Ballauff, M. Thermosensitive Core-Shell Microgels: From Colloidal Model Systems to Nanoreactors. *Prog. Polym. Sci.* **2011**, *36*, 767–792.

(88) Wu, S.; Dzubiella, J.; Kaiser, J.; Drechsler, M.; Guo, X.; Ballauff, M.; Lu, Y. Thermosensitive Au PNIPA Yolk Shell Particles with Tunable Selectivity for Catalysis. *Angew. Chem. Int. Ed.* **2012**, *51*, 2229–2233.

(89) Chu, F.; Siebenbürger, M.; Polzer, F.; Stolze, C.; Kaiser, J.; Hoffmann, M.; Heptner, N.; Dzubiella, J.; Drechsler, M.; Lu, Y.; *et al.* Synthesis and Characterization of Monodisperse Thermosensitive Dumbbell-Shaped Microgels. *Macromol. Rapid Commun.* **2012**, *33*, 1042–1048.

(90) Dagallier, C.; Dietsch, H.; Schurtenberger, P.; Scheffold, F. Thermoresponsive Hybrid Microgel Particles with Intrinsic Optical and Magnetic Anisotropy. *Soft Matter* **2010**, *6*, 2174–2177.

(91) Städele, V.; Gasser, U.; Dietsch, H. Ellipsoidal Hybrid Magnetic Microgel Particles with Thermally Tunable Aspect Ratios. *Soft Matter* **2012**, *8*, 4427–4431.

(92) Crassous, J. J.; Dietsch, H.; Pfleiderer, P.; Malik, V.; Diaz, A.; Hirshi, L. A.; Drechsler, M.; Schurtenberger, P. Preparation and Characterization of Ellipsoidal-Shaped Thermosensitive Microgel Colloids with Tailored Aspect Ratios. *Soft Matter* **2012**, *8*, 3538–3548.

(93) Chesworth, W. The Stability of Gibbsite and Boehmite at the Surface of the Earth. *Clays Clay Miner.* **1972**, *20*, 369–374.

(94) Gitzen, W. H. Alumina as a Ceramic Material. In *The American Ceramic Society, Columbus, OH*; 1970.

(95) Wierenga, A. M.; Lenstra, T. A. J.; Philipse, A. P. Aqueous Dispersions of Colloidal Gibbsite Platelets: Synthesis, Characterisation and Intrinsic Viscosity Measurements. *Colloids Surfaces A Physicochem. Eng. Asp.* **1998**, *134*, 359–371.

(96) Olphen, H. van. Internal Mutual Flocculation in Clay Suspensions. *J. Colloid Sci.* **1964**, *19*, 313–322.

(97) van Blaaderen, A.; Wiltzius, P. Real-Space Structure of Colloidal Hard-Sphere Glasses. *Science* **1995**, *270*, 1177–1179.

(98) Grier, D. G.; Murray, C. A. The Microscopic Dynamics of Freezing in Supercooled Colloidal Fluids. *J. Chem. Phys* **1994**, *100*, 9088–9095.

(99) Hoover, W. G.; Ree, F. H. Melting Transition and Communal Entropy for Hard Spheres. *J. Chem. Phys.* **1968**, *49*, 3609–3617.

(100) Bolhuis, P.; Frenkel, D. Tracing the Phase Boundaries of Hard Spherocylinders. *J. Chem. Phys.* **1997**, *106*, 666–687.

(101) Stroobants, A.; Lekkerkerker, H. N. W. Evidence for One-, Two, and Three-Dimensional Order in a System of Hard Parallel Spherocylinders. *Phys. Rev. A* **1987**, *36*, 2929–2945.

(102) van der Kooij, F. M.; Kassapidou, K.; Lekkerkerker, H. N. W. Liquid Crystal Phase Transitions in Suspensions of Polydisperse Plate-like Particles. *Nature* **2000**, *406*, 868–871.

(103) Mourad, M. C. D.; Groeneveld, E.; De Lange, P. J.; Vonk, C.; Van Der Beek, D.; Lekkerkerker, H. N. W. Columnar Liquid Crystals of Gibbsite Platelets as Templates for the Generation of Ordered Silica Structures. *J. Mater. Chem.* **2008**, *18*, 3004–3010.

(104) Wijnhoven, J. E. G. J. Coating of Gibbsite Platelets with Silica. *Chem. Mater.* **2004**, *16*, 3821–3828.

(105) Wang, X.; Zhao, D.; Diaz, A.; Nava Medina, I. B.; Wang, H.; Cheng, Z. Thermo-Sensitive Discotic Colloidal Liquid Crystals. *Soft Matter* **2014**, *10*, 7692–7695.

(106) Liu, S.; Han, M. Y. Silica-Coated Metal Nanoparticles. *Chem. - An Asian J.* **2010**, *5*, 36–45.

(107) Wu, W.; He, Q.; Jiang, C. Magnetic Iron Oxide Nanoparticles: Synthesis and Surface Functionalization Strategies. *Nanoscale Res. Lett.* **2008**, *3*, 397–415.

(108) Mulvaney, P.; Liz-Marzán, L. M.; Giersig, M.; Ung, T. Silica Encapsulation of Quantum Dots and Metal Clusters. *J. Mater. Chem.* **2000**, *10*, 1259–1270.

(109) Graf, C.; Vossen, D. L. J.; Imhof, A.; van Blaaderen, A. A General Method to Coat Colloidal Particles with Silica. *Langmuir* **2003**, *19*, 6693–6700.

(110) Stöber, W.; Fink, A. Controlled Growth of Monodisperse Silica Spheres in the Micron Size Range. *J. Colloid Interface Sci.* **1968**, *26*, 62–69.

(111) Stuart, M. a C.; Huck, W. T. S.; Genzer, J.; Müller, M.; Ober, C.; Stamm, M.; Sukhorukov, G. B.; Szleifer, I.; Tsukruk, V. V; Urban, M.; *et al.* Emerging Applications of Stimuli-Responsive Polymer Materials. *Nat. Mater.* **2010**, *9*, 101–113.

(112) de Las Heras Alarcon, C.; Pennadam, S.; Alexander, C. Stimuli Responsive Polymers for Biomedical Applications. *Chem. Soc. Rev.* **2005**, *34*, 276–285.

(113) Guan, Y.; Zhang, Y. PNIPAM Microgels for Biomedical Applications: From Dispersed Particles to 3D Assemblies. *Soft Matter* **2011**, *7*, 6375.

(114) Li, Y.; Tanaka, T. Phase Transitions of Gels. *Annu. Rev. Mater. Sci.* **1992**, *22*, 243–277.

(115) Shibayama, M.; Tanaka, T. Volume Phase Transtition and Related Phenomena of Polymer Gels. *Adv. Polym. Sci.* **1993**, 1–62.

(116) Schild, H. G. Poly(N-Isopropylacrylamide): Experiment, Theory and Application. *Prog. Polym. Sci.* **1992**, *17*, 163–249.

(117) Li, G. L.; Möhwald, H.; Shchukin, D. G. Precipitation Polymerization for Fabrication of Complex Core-Shell Hybrid Particles and Hollow Structures. *Chem. Soc. Rev.* **2013**, *42*, 3628–3646.

(118) Lee, H.; Rho, J.; Messersmith, P. B. Facile Conjugation of Biomolecules onto Surfaces via Mussel Adhesive Protein Inspired Coatings. *Adv. Mater.* **2009**, *21*, 431–434.

(119) Bernsmann, F.; Ball, V.; Addiego, F.; Ponche, A.; Michel, M.; de Almeida Gracio, J. J.; Toniazzo, V.; Ruch, D. Dopamine-Melanin Film Deposition Depends on the Used Oxidant and Buffer Solution. *Langmuir* **2011**, *27*, 2819–2825.

(120) Wei, Q.; Zhang, F.; Li, J.; Li, B.; Zhao, C. Oxidant-Induced Dopamine Polymerization for Multifunctional Coatings. *Polym. Chem.* **2010**, *1*, 1430–1433.

(121) Yu, F.; Chen, S.; Chen, Y.; Li, H.; Yang, L.; Chen, Y.; Yin, Y. Experimental and Theoretical Analysis of Polymerization Reaction Process on the Polydopamine Membranes and Its Corrosion Protection Properties for 304 Stainless Steel. *J. Mol. Struct.* **2010**, *982*, 152–161.

(122) Zangmeister, R. A.; Morris, T. A.; Tarlov, M. J. Characterization of Polydopamine Thin Films Deposited at Short Times by Autoxidation of Dopamine. *Langmuir* **2013**, *29*, 8619–8628.

(123) Luczak, T. Preparation and Characterization of the Dopamine Film Electrochemically Deposited on a Gold Template and Its Applications for Dopamine Sensing in Aqueous Solution. *Electrochim. Acta* **2008**, *53*, 5725–5731.

(124) Gidanian, S.; Farmer, P. J. Redox Behavior of Melanins: Direct Electrochemistry of Dihydroxyindole-Melanin and Its Cu and Zn Adducts. *J. Inorg. Biochem.* **2002**, *89*, 54–60.

(125) D'Ischia, M.; Napolitano, A.; Pezzella, A.; Meredith, P.; Sarna, T. Chemical and Structural Diversity in Eumelanins: Unexplored Bio-Optoelectronic Materials. *Angew. Chem. Int. Ed.* **2009**, *48*, 3914–3921.

(126) Zhu, L.; Lu, Y.; Wang, Y.; Zhang, L.; Wang, W. Preparation and Characterization of Dopamine-Decorated Hydrophilic Carbon Black. *Appl. Surf. Sci.* **2012**, *258*, 5387–5393.

(127) Dreyer, D. R.; Miller, D. J.; Freeman, B. D.; Paul, D. R. Elucidating the Structure of Poly (Dopamine). *Langmuir* **2012**, *28*, 6428–6435.

(128) Ball, V.; Frari, D. Del; Toniazzo, V.; Ruch, D. Kinetics of Polydopamine Film Deposition as a Function of pH and Dopamine Concentration: Insights in the Polydopamine Deposition Mechanism. *J. Colloid Interface Sci.* **2012**, *386*, 366–372.

(129) Shin, Y. M.; Jun1, I.; Lim, Y.-M.; Rhim, T.; Shin, H. Bio-inspired Immobilization of Cell-Adhesive Ligands on Electrospun Nanofibrous Patches for Cell Delivery. *Macromol. Mater. Eng.* **2013**, *298*, 555–564.

(130) Ju, K.; Lee, Y.; Lee, S.; Park, S. B.; Lee, J. Bioinspired Polymerization of Dopamine to Generate Melanin-Like Nanoparticles Having an Excellent Free-Radical-Scavenging Property. *Biomacromolecules* **2011**, *12*, 625–632.

(131) Hong, S.; Lee, J. S.; Ryu, J.; Lee, S. H.; Lee, D. Y.; Kim, D.; Park, C. B.; Lee, H. Bio-Inspired Strategy for on-Surface Synthesis of Silver Nanoparticles for Metal/organic Hybrid Nanomaterials and LDI-MS Substrates. *Nanotechnology* **2011**, *22*, 494020.

(132) Zhang, M.; Zhang, X.; He, X.; Zhang, Y. Preparation and Characterization of Polydopamine-Coated Silver Core/Shell Nanocables. *Chem. Lett.* **2010**, *39*, 552–553.

(133) Black, K. C. L.; Liu, Z.; Messersmith, P. B. Catechol Redox Induced Formation of Metal Core-Polymer Shell Nanoparticles. *Chem. Mater.* **2011**, *23*, 1130–1135.

(134) Guo, L.; Liu, Q.; Li, G.; Shi, J.; Liu, J.; Wang, T.; Jiang, G. A Mussel-Inspired Polydopamine Coating as a Versatile Platform for the in Situ Synthesis of Graphene-Based Nanocomposites. *Nanoscale* **2012**, *4*, 5864–5867.

(135) Henglein, A. Small-Particle Research: Physicochemical Properties of Extremely Small Colloidal Metal and Semiconductor Particles. *Chem. Rev.* **1989**, *89*, 1861–1873.

(136) Ferrando, R.; Jellinek, J.; Johnston, R. L. Nanoalloys: From Theory to Applications of Alloy Clusters and Nanoparticles. *Chem. Rev.* **2008**, *108*, 845–910.

(137) Taarning, E.; Madsen, A. T.; Marchetti, J. M.; Egeblad, K.; Christensen, C. H. Oxidation of Glycerol and Propanediols in Methanol over Heterogeneous Gold Catalysts. *Green Chem.* **2008**, *10*, 408–414.

(138) Wittstock, A.; Zielasek, V.; Biener, J.; Friend, C. M.; Bäumer, M. Nanoporous Gold Catalysts for Selective Methanol at Low Temperature. *Science* **2010**, *327*, 319–322.

(139) Hayashi, T.; Inagaki, T.; Itayama, N.; Baba, H. Selective Oxidation of Alcohol over Supported Gold Catalysts: Methyl Glycolate Formation from Ethylene Glycol and Methanol. *Catal. Today* **2006**, *117*, 210–213.

(140) Dorda, G.; Pepper, M.; Karlhede, A.; Kivelson, S. a; Rezayi, E. H.; Macdonald, a H.; Tutuc, E.; Papadakis, S. J.; Shayegan, M.; Saku, T.; *et al.* Chemoselective Hydrogenation of. *Science* **2006**, *313*, 332–334.

(141) Bailie, J. E.; Hutchings, G. J. Promotion by Sulfur of Gold Catalysts for Crotyl Alcohol Formation from Crotonaldehyde Hydrogenation. *Chem. Commun.* **1999**, 2151–2152.

(142) Sinha, a K.; Seelan, S.; Tsubota, S.; Haruta, M. Catalysis by Gold Nanoparticles: Epoxidation of Propene. *Top. Catal.* **2004**, *29*, 95–102.

(143) Willis, N. G.; Guzman, J. Influence of the Support during Homocoupling of Phenylboronic Acid Catalyzed by Supported Gold. *Appl. Catal. A Gen.* **2008**, *339*,

68–75.

(144) Kaiser, J.; Szczerba, W.; Riesemeier, H.; Reinholz, U.; Radtke, M.; Albrecht, M.; Lu, Y.; Ballauff, M. The Structure of AuPd Nanoalloys Anchored on Spherical Polyelectrolyte Brushes Determined by X-Ray Absorption Spectroscopy. *Faraday Discuss.* **2013**, *162*, 45–55.

(145) Wunder, S.; Polzer, F.; Lu, Y.; Mei, Y.; Ballauff, M. Kinetic Analysis of Catalytic Reduction of 4-Nitrophenol by Metallic Nanoparticles Immobilized in Spherical Polyelectrolyte Brushes. *J. Phys. Chem. C* **2010**, *114*, 8814–8820.

(146) Hervés, P.; Pérez-Lorenzo, M.; Liz-Marzán, L. M.; Dzubiella, J.; Lu, Y.; Ballauff, M. Catalysis by Metallic Nanoparticles in Aqueous Solution: Model Reactions. *Chem. Soc. Rev.* **2012**, *41*, 5577–5587.

(147) Zhou, X.; Xu, W.; Liu, G.; Panda, D.; Chen, P. Size Dependent Catalytic Activity and Dynamics of Gold Nanoparticles at the Single-Molecule Level. *J. Am. Chem. Soc.* **2010**, *132*, 138–146.

(148) Panigrahi, S.; Basu, S.; Praharaj, S.; Pande, S.; Jana, S.; Pal, A.; Ghosh, S.; Pal, T. Sythesis and Size-Selective Catalysis by Supported Gold Nanoparticles: Study on Heterogeneoue and Homogeneous Catalytic Process. *J. Phys. Chem. C* **2007**, *111*, 4596–4605.

(149) Mei, Y.; Lu, Y.; Polzer, F.; Ballauff, M.; Drechsler, M. Catalytic Activity of Palladium Nanoparticles Encapsulated in Spherical Polyelectrolyte Brushes and Core-Shell Microgels. *Chem. Mater.* **2007**, *19*, 1062–1069.

(150) Mei, Y.; Sharma, G.; Lu, Y.; Ballauff, M.; Drechsler, M.; Irrgang, T.; Kempe, R. High Catalytic Activity of Platinum Nanoparticles Immobilized on Spherical Polyelectrolyte Brushes. *Langmuir* **2005**, *21*, 12229–12234.

(151) Wunder, S.; Lu, Y.; Albrecht, M.; Ballauff, M. Catalytic Activity of Faceted Gold Nanoparticles Studied by a Model Reaction: Evidence for Substrate-Induced Surface Restructuring. *ACS Catal.* **2011**, *1*, 908–916.

(152) Gu, S.; Wunder, S.; Lu, Y.; Ballauff, M.; Fenger, R.; Rademann, K.; Jaquet, B.; Zaccone, A. Kinetic Analysis of the Catalytic Reduction of 4-Nitrophenol by Metallic Nanoparticles. *J. Phys. Chem. C* **2014**, *118*, 18618–18625.

(153) Corma, A.; Concepcion, P.; Serna, P. A Different Reaction Pathway for the Reduction of Aromatic Nitro Compounds on Gold Catalysts. *Angew. Chem. Int. Ed.* **2007**, *119*, 7404–7407.

(154) Gu, S.; Lu, Y.; Kaiser, J.; Albrecht, M.; Ballauff, M. Kinetic Analysis of the Reduction of 4-Nitrophenol Catalyzed by Au/Pd Nanoalloys Immobilized in Spherical Polyelectrolyte Brushes. *Phys. Chem. Chem. Phys.* **2015**, *17*, 28137–28143.

(155) Wang, J.; Xin, H. L.; Wang, D. Recent Progress on Mesoporous Carbon Materials for Advanced Energy Conversion and Storage. *Part. Part. Syst. Charact.* **2014**, *31*, 515–539.

(156) Yang, Z.; Ren, J.; Zhang, Z.; Chen, X.; Guan, G.; Qiu, L.; Zhang, Y.; Peng, H. Recent Advancement of Nanostructured Carbon for Energy Applications. *Chem. Rev.* **2015**, *115*, 5159–5223.

(157) Xie, K.; Wei, B. Materials and Structures for Stretchable Energy Storage and Conversion Devices. *Adv. Mater.* **2014**, *26*, 3592–3617.

(158) Ji, X.; Nazar, L. F. Advances in Li-S Batteries. *J. Mater. Chem.* **2010**, *20*, 9821–9826.

(159) Wu, S.; Xu, R.; Lu, M.; Ge, R.; Iocozzia, J.; Han, C.; Jiang, B.; Lin, Z. Graphene-Containing Nanomaterials for Lithium-Ion Batteries. *Adv. Energy Mater.* **2015**, *5*, 1500400.

(160) Yan, J.; Wang, Q.; Wei, T.; Fan, Z. Recent Advances in Design and Fabrication of Electrochemical Supercapacitors with High Energy Densities. *Adv. Energy Mater.* **2014**, *4*, 1300816.

(161) González, A.; Goikolea, E.; Andoni, J.; Mysyk, R. Review on Supercapacitors: Technologies and Materials. *Renew. Sustain. energy Rev.* **2016**, *58*, 1189–1206.

(162) Simon, P.; Gogotsi, Y. Capacitive Energy Storage in Nanostructured Carbon-Electrolyte Systems. *Acc. Chem. Res.* **2013**, *46*, 1094–1103.

(163) Helmholtz, H. Ueber Einige Gesetze Der Vertheilung Elektrischer Ströme in Körperlichen Leitern Mit Anwendung Auf Die Thierisch-Elektrischen Versuche. *Ann. Phys.* **1853**, *165*, 211–233.

(164) Béguin, F.; Presser, V.; Balducci, A.; Frackowiak, E. Carbons and Electrolytes for Advanced Supercapacitors. *Adv. Mater.* **2014**, *26*, 2219–2251.

(165) Gouy, M. Sur La Constitution de La Charge Électrique À La Surface D'un Électrolyte. *J. Phys. Théorique Appliquée* **1910**, *9*, 457–468.

(166) Li, X.; Wei, B. Supercapacitors Based on Nanostructured Carbon. *Nano Energy* **2013**, *2*, 159–173.

(167) Liu, C.; Li, F.; Lai-Peng, M.; Cheng, H.-M. Advanced Materials for Energy Storage. *Adv. Mater.* **2010**, *22*, E28–E62.

(168) Wang, D. W.; Li, F.; Liu, M.; Lu, G. Q.; Cheng, H. M. Mesopore-Aspect-Ratio Dependence of Ion Transport in Rodtype Ordered Mesoporous Carbon. *J. Phys. Chem. C* **2008**, *112*, 9950–9955.

(169) Wang, H.; Xu, Z.; Kohandehghan, A.; Li, Z.; Cui, K.; Tan, X.; Stephenson, T. J.; King'Ondu, C. K.; Holt, C. M. B.; Olsen, B. C.; *et al.* Interconnected Carbon Nanosheets Derived from Hemp for Ultrafast Supercapacitors with High Energy. *ACS Nano* **2013**, *7*, 5131–5141.

(170) Ruiz, V.; Blanco, C.; Raymundo-Piñero, E.; Khomenko, V.; Béguin, F.; Santamaría, R. Effects of Thermal Treatment of Activated Carbon on the Electrochemical Behavior in Supercapacitors. *Electrochim. Acta* **2007**, *52*, 4969–4973.

(171) Khomenko, V.; Raymundo-Piñero, E.; Frackowiak, E.; Béguin, F. High-Voltage

Asymmetric Supercapacitors Operating in Aqueous Electrolyte. *Appl. Phys. A Mater. Sci. Process.* **2006**, *82*, 567–573.

(172) Gao, Q.; Demarconnay, L.; Raymundo-Piñero, E.; Béguin, F. Exploring the Large Voltage Range of Carbon/carbon Supercapacitors in Aqueous Lithium Sulfate Electrolyte. *Energy Environ. Sci.* **2012**, *5*, 9611–9617.

(173) Fic, K.; Lota, G.; Meller, M.; Frackowiak, E. Novel Insight into Neutral Medium as Electrolyte for High-Voltage Supercapacitors. *Energy Environ. Sci.* **2012**, *5*, 5842–5850.

(174) Buining, P. A.; Pathmamanoharan, C.; Jansen, J. B. H.; Lekkerkerker, H. N. W. Preparation of Colloidal Boehmite Needles by Hydrothermal Treatment of Aluminum Alkoxide Precursors. *J. Am. Ceram. Soc.* **1991**, *74*, 1303–1307.

(175) Montagna, W.; Prota, G.; Kenney, J. A. Black Skin: Structure and Function. In *Academic Press Inc*; 1993; pp. 21–54.

(176) Yu, B.; Liu, J.; Liu, S.; Zhou, F. Pdop Layer Exhibiting Zwitterionicity: A Simple Electrochemical Interface for Governing Ion Permeability. *Chem. Commun.* **2010**, *46*, 5900–5902.

(177) Oster, B. Y. G. Two-Phase Formation in Solutions of Tobacco Mosaic Virus and the Problem of Long-Range Forces. *J. Gen. Physiol.* **1950**, *33*, 445–473.

(178) Maeda, Y.; Hachisu, S. Structure of Schiller Layers in β-FeOOH Sols: Observation by Scanning Electron Microscope. *Colloids and Surfaces* **1983**, *7*, 357–360.

(179) Vroege, G. J.; Thies-Weesie, D. M. E.; Petukhov, A. V.; Lemaire, B. J.; Davidson, P. Smectic Liquid-Crystalline Order in Suspensions of Highly Polydisperse Goethite Nanorods. *Adv. Mater.* **2006**, *18*, 2565–2568.

(180) Zocher, H. Spontaneous Structure Formation in Sols; a New Kind of Anisotropic Liquid Media. *Zeitschrift für Anorg. und Allg. Chemie* **1925**, *147*, 91–110.

(181) Furasawa, K.; Hachisu, S. J. Interparticle Distance in Schiller Layers of Tungstic Acid Sol. *J. Colloid Interface Sci.* **1968**, *28*, 167–168.

(182) Gabriel, J. C.; Camerel, F.; Lemaire, B. J.; Desvaux, H.; Davidson, P.; Batail, P. Swollen Liquid-Crystalline Lamellar Phase Based on Extended Solid-like Sheets. *Nature* **2001**, *413*, 504–508.

(183) van der Beek, D.; Lekkerkerker, H. N. W. Liquid Crystal Phases of Charged Colloidal Platelets. *Langmuir* **2004**, *20*, 8582–8586.

(184) Mourad, M. C. D.; Wijnhoven, J. E. G. J.; Van't Zand, D. D.; van der Beek, D.; Lekkerkerker, H. N. W. Gelation versus Liquid Crystal Phase Transitions in Suspensions of Plate-like Particles. *Philos. Trans. Ser. A* **2006**, *364*, 2807–2816.

(185) Wijnhoven, J. E. G. J.; Van't Zand, D. D.; Van Der Beek, D.; Lekkerkerker, H. N. W. Sedimentation and Phase Transitions of Colloidal Gibbsite Platelets. *Langmuir* **2005**, *21*, 10422–10427.

(186) Petukhov, A. V.; Van Der Beek, D.; Dullens, R. P. A.; Dolbnya, I. P.; Vroege, G. J.; Lekkerkerker, H. N. W. Observation of a Hexatic Columnar Liquid Crystal of Polydisperse Colloidal Disks. *Phys. Rev. Lett.* **2005**, *95*, 077801.

(187) Van Der Beek, D.; Petukhov, A. V.; Oversteegen, S. M.; Vroege, G. J.; Lekkerkerker, H. N. W. Evidence of the Hexagonal Columnar Liquid-Crystal Phase of Hard Colloidal Platelets by High-Resolution SAXS. *Eur. Phys. J. E* **2005**, *16*, 253–258.

(188) Fan, Z.; Zhang, H. Crystal Phase-Controlled Synthesis, Properties and Applications of Noble Metal Nanomaterials. *Chem. Soc. Rev.* **2016**, *45*, 63–82.

(189) Corma, A.; Garcia, H. Supported Gold Nanoparticles as Catalysts for Organic Reactions. *Chem. Soc. Rev.* **2008**, *37*, 2096–2126.

(190) Peng, X.; Pan, Q.; Rempel, G. L. Bimetallic Dendrimer-Encapsulated Nanoparticles as Catalysts: A Review of the Research Advances. *Chem. Soc. Rev.* **2008**, *37*, 1619–1628.

(191) Myers, V. S.; Weir, M. G.; Carino, E. V.; Yancey, D. F.; Pande, S.; Crooks, R. M. Dendrimer-Encapsulated Nanoparticles: New Synthetic and Characterization Methods and Catalytic Applications. *Chem. Sci.* **2011**, *2*, 1632–1646.

(192) Eastoe, J.; Hollamby, M. J.; Hudson, L. Recent Advances in Nanoparticle Synthesis with Reversed Micelles. *Adv. Colloid Interface Sci.* **2006**, *128*, 5–15.

(193) Esumi, K.; Isono, R.; Yoshimura, T. Preparation of PAMAM-and PPI-Metal (Silver, Platinum, and Palladium) Nanocomposites and Their Catalytic Activities for Reduction of 4-Nitrophenol. *Langmuir* **2004**, *20*, 237–243.

(194) Tsunoyama, H.; Sakurai, H.; Negishi, Y.; Tsukuda, T. Size-Specific Catalytic Activity of Polymer-Stabilized Gold Nanoclusters for\rAerobic Alcohol Oxidation in Water. *J. Am. Chem. Soc.* **2005**, *127*, 9374–9375.

(195) Lu, Y.; Proch, S.; Schrinner, M.; Drechsler, M.; Kempe, R.; Ballauff, M. Thermosensitive Core-Shell Microgel as A “nanoreactor” for Catalytic Active Metal Nanoparticles. *J. Mater. Chem.* **2009**, *19*, 3955–3961.

(196) Jiang, L.; Gao, L. Modified Carbon Nanotubes: An Effective Way to Selective Attachment of Gold Nanoparticles. *Carbon* **2003**, *41*, 2923–2929.

(197) Johnson, S. R.; Evans, S. D.; Brydson, R. Influence of a Terminal Functionality on the Physical Properties of Surfactant-Stabilized Gold Nanoparticles. *Langmuir* **1998**, *14*, 6639–6647.

(198) Kidambi, S.; Bruening, M. L. Multilayered Polyelectrolyte Films Containing Palladium Nanoparticles: Synthesis, Characterization, and Application in Selective Hydrogenation. *Chem. Mater.* **2005**, *17*, 301–307.

(199) Lu, Y.; Wittemann, A.; Ballauff, M. Supramolecular Structures Generated by Spherical Polyelectrolyte Brushes and Their Application in Catalysis. *Macromol. Rapid Commun.* **2009**, *30*, 806–815.

(200) Black, K. C. L.; Liu, Z. Q.; Messersmith, P. B. Catechol Redox Induced Formation of

Metal Core-Polymer Shell Nanoparticles. *Chem. Mater.* **2011**, *23*, 1130–1135.

(201) Haruta, M. Size- and Support-Dependency in the Catalysis of Gold. *Catal. Today* **1997**, *36*, 153–166.

(202) Corma, A.; Serna, P. Chemoselective Hydrogenation of Nitro Compounds with Supported Gold Catalysts. *Science* **2006**, *313*, 332–334.

(203) Lu, Y.; Yuan, J.; Polzer, F.; Drechsler, M.; Preussner, J. In Situ Growth of Catalytic Active Au-Pt Bimetallic Nanorods in Thermoresponsive Core-Shell Microgels. *ACS Nano* **2010**, *4*, 7078–7086.

(204) Lu, Y.; Hoffmann, M.; Yelamanchili, R. S.; Terrenoire, A.; Schrinner, M.; Drechsler, M.; Möller, M. W.; Breu, J.; Ballauff, M. Weil-Defined Crystalline TiO_2 Nanoparticles Generated and Immobilized on a Colloidal Nanoreactor. *Macromol. Chem. Phys.* **2009**, *210*, 377–386.

(205) Lu, Y.; Lunkenbein, T.; Preussner, J.; Proch, S.; Breu, J.; Kempe, R.; Ballauff, M. Composites of Metal Nanoparticles and TiO_2 Immobilized in Spherical Polyelectrolyte Brushes. *Langmuir* **2010**, *26*, 4176–4183.

(206) Jia, H.; Schmitz, D.; Ott, A.; Pich, A.; Lu, Y. Cyclodextrin Modified Microgels As "nanoreactor" for the Generation of Au Nanoparticles with Enhanced Catalytic Activity. *J. Mater. Chem. A* **2015**, *3*, 6187–6195.

(207) Gu, S.; Kaiser, J.; Marzun, G.; Ott, A.; Lu, Y.; Ballauff, M.; Zaccone, A.; Barcikowski, S.; Wagener, P. Ligand-Free Gold Nanoparticles as a Reference Material for Kinetic Modelling of Catalytic Reduction of 4-Nitrophenol. *Catal. Letters* **2015**, *145*, 1105–1112.

(208) Ciganda, R.; Li, N.; Deraedt, C.; Gatard, S.; Zhao, P.; Salmon, L.; Herná Ndez, R.; Ruiz, J.; Astruc, D. Gold Nanoparticles as Electron Reservoir Redox Catalysts for 4-Nitrophenol Reduction: A Strong Stereoelectronic Ligand Influence. *Chem. Commun.* **2014**, *50*, 10126–10129.

(209) Zhang, Y.; Liu, S.; Lu, W.; Wang, L.; Tian, J.; Sun, X. In Situ Green Synthesis of Au Nanostructures on Graphene Oxide and Their Application for Catalytic Reduction of 4-Nitrophenol. *Catal. Sci. Technol.* **2011**, *1*, 1142–1144.

(210) Lu, W.; Ning, R.; Qin, X.; Zhang, Y.; Chang, G.; Liu, S.; Luo, Y.; Sun, X. Synthesis of Au Nanoparticles Decorated Graphene Oxide Nanosheets: Noncovalent Functionalization by TWEEN 20 in Situ Reduction of Aqueous Chloroaurate Ions for Hydrazine Detection and Catalytic Reduction of 4-Nitrophenol. *J. Hazard. Mater.* **2011**, *197*, 320–326.

(211) Yamamoto, H.; Yano, H.; Kouchi, H.; Obora, Y.; Arakawa, R.; Kawasaki, H. N,N-Dimethylformamide-Stabilized Gold Nanoclusters as a Catalyst for the Reduction of 4-Nitrophenol. *Nanoscale* **2012**, *4*, 4148–4154.

(212) Zhou, J.; Duan, B.; Fang, Z.; Song, J.; Wang, C.; Messersmith, P. B.; Duan, H. Interfacial Assembly of Mussel-Inspired Au@Ag@polydopamine Core-Shell

Nanoparticles for Recyclable Nanocatalysts. *Adv. Mater.* **2014**, *26*, 701–705.

(213) Xuan, S.; Wang, Y.-X. J.; Yu, J. C.; Leung, K. C.-F. Preparation, Characterization, and Catalytic Activity of Core/Shell Fe_3O_4@Polyaniline@Au Nanocomposites. *Langmuir* **2009**, *25*, 11835–11843.

(214) Mao, Y.; Jiang, W.; Xuan, S.; Fang, Q.; Leung, K. C.-F.; Ong, B. S.; Wang, S.; Gong, X. Rod-like *β*-FeOOH@poly(dopamine)-Au-Poly(dopamine) Nanocatalysts with Improved Recyclable Activities. *Dalt. Trans.* **2015**, *44*, 9538–9544.

(215) Ge, J.; Zhang, Q.; Zhang, T.; Yin, Y. Core-Satellite Nanocomposite Catalysts Protected by a Porous Silica Shell: Controllable Reactivity, High Stability, and Magnetic Recyclability. *Angew. Chem. Int. Ed.* **2008**, *47*, 8924–8928.

(216) Ye, Q.; Zhou, F.; Liu, W. Bioinspired Catecholic Chemistry for Surface Modification. *Chem. Soc. Rev.* **2011**, *40*, 4244–4258.

(217) Liu, Y.; Ai, K.; Lu, L. Polydopamine and Its Derivative Materials: Synthesis and Promising Applications in Energy, Environmental, and Biomedical Fields. *Chem. Rev.* **2014**, *114*, 5057–5115.

(218) Solomon, M. J.; Spicer, P. T. Microstructural Regimes of Colloidal Rod Suspensions, Gels,and Glasses. *Soft Matter* **2010**, *6*, 1391–1400.

(219) Radu, M.; Pfleiderer, P.; Schilling, T. Solid-Solid Phase Transition in Hard Ellipsoids Solid-Solid Phase Transition in Hard Ellipsoids. *J. Chem. Phys.* **2009**, *131*, 164513.

(220) Marechal, M.; Dijkstra, M. Colloidal Hard Dumbbells under Gravity: Structure and Crystallization. *Soft Matter* **2011**, *7*, 1397–1408.

(221) Pelton, R. Temperature-Sensitive Aqueous Microgels. *Adv. Colloid Interface Sci.* **2000**, *85*, 1–33.

(222) Richtering, W. Responsive Emulsions Stabilized by Stimuli-Sensitive Microgels: Emulsions with Special Non-Pickering Properties. *Langmuir* **2012**, *28*, 17218–17229.

(223) Nayak, S.; Lyon, L. A. Soft Nanotechnology with Soft Nanoparticles. *Angew. Chem. Int. Ed.* **2005**, *44*, 7686–7708.

(224) Shi, S.; Wang, Q.; Wang, T.; Ren, S.; Gao, Y.; Wang, N. Thermo, pH, and Light-Responsive Poly(N-Isopropylacrylamide-Co-Methacrylic Acid) − Au Hybrid Microgels Prepared by the in Situ Reduction Method Based on Au-Thiol Chemistry. *J. Phys. Chem. B* **2014**, *118*, 7177–7186.

(225) Karg, M.; Pastoriza-santos, I.; Rodriguez-gonza, B.; Von Klitzing, R.; Wellert, S.; Hellweg, T. Temperature, pH, and Ionic Strength Induced Changes of the Swelling Behavior of PNIPAM-Poly (Allylacetic Acid) Copolymer Microgels. *Langmuir* **2008**, *24*, 6300–6306.

(226) Chu, F. F.; Polzer, F.; Severin, N.; Lu, Y.; Ott, A.; Rabe, J. P.; Ballauff, M. Thermosensitive Hollow Janus Dumbbells. *Colloid Polym. Sci.* **2014**, *292*, 1785–1793.

(227) Clarke, K. C.; Dunham, S. N.; Lyon, L. A. Core/Shell Microgels Decouple the pH and

Temperature Responsivities of Microgel Films. *Chem. Mater.* **2015**, *27*, 1391–1396.

(228) Crassous, J. J.; Rochette, C. N.; Wittemann, A.; Schrinner, M.; Ballauff, M. Quantitative Analysis of Polymer Colloids by Cryo-Transmission Electron Microscopy. *Langmuir* **2009**, *25*, 7862–7871.

(229) Senff, H.; Richtering, W.; Weiss, A.; Ballauff, M. Rheology of a Temperature Sensitive Core-Shell Latex. *Langmuir* **1999**, *15*, 102–106.

(230) Lu, Y.; Mei, Y.; Ballauff, M.; Drechsler, M. Thermosensitive Core-Shell Particles as Carrier Systems for Metallic Nanoparticles. *J. Phys. Chem. B* **2006**, *110*, 3930–3937.

(231) Wu, S.; Dzubiella, J.; Kaiser, J.; Drechsler, M.; Guo, X.; Ballauff, M.; Lu, Y. Thermosensitive Au-PNIPA Yolk-Shell Nanoparticles with Tunable Selectivity for Catalysis. *Angew. Chem. Int. Ed.* **2012**, *51*, 2229–2233.

(232) Contreras-Cáceres, R.; Pacifico, J.; Pastoriza-Santos, I.; Pérez-Juste, J.; Fernández-Barbero, A.; Liz-Marzán, L. M. Au@PNIPAM Thermosensitive Nanostructures: Control over Shell Cross-Linking, Overall Dimensions, and Core Growth. *Adv. Funct. Mater.* **2009**, *19*, 3070–3076.

(233) Dagallier, C.; Cardinaux, F.; Dietsch, H.; Scheffold, F. Magnetic Orientation of Soft Particles in a Jammed Solid. *Soft Matter* **2012**, *8*, 4067–4071.

(234) Philipse, A. P.; Nechifor, A.-M.; Patmamanoharan, C. Isotropic and Birefringent Dispersions of Surface Modified Silica Rods with a Boehmite-Needle Core. *Langmuir* **1994**, *10*, 4451–4458.

(235) Liz-Marzán, L. M.; Giersig, M.; Mulvaney, P. Synthesis of Nanosized Gold-Silica Core-Shell Particles. *Langmuir* **1996**, *12*, 4329–4335.

(236) van Blaaderen, A.; Kentgens, A. P. M. Particle Morphology and Chemical Microstructure of Colloidal Silica Spheres Made from Alkoxysilanes. *J. Non. Cryst. Solids* **1992**, *149*, 161–178.

(237) Yan, L.; Wang, Z.; Yan, J.; Han, L.; Zhou, Q.; You, Y. Selectively Grafting Polymer from the Interior And/or Exterior Surfaces of Bioreducible and Temperature-Responsive Nanocapsules. *Polym. Chem.* **2013**, *4*, 1243–1249.

(238) Crassous, J. J.; Siebenbürger, M.; Ballauff, M.; Drechsler, M.; Henrich, O.; Fuchs, M. Thermosensitive Core-Shell Particles as Model Systems for Studying the Flow Behavior of Concentrated Colloidal Dispersions. *J. Chem. Phys.* **2006**, *125*, 204906.

(239) Makino, K.; Yamamoto, S.; Fujimoto, K.; Kawaguchi, H.; Ohshima, H. Surface Structure of Latex Particles Covered with Temperature-Sensitive Hydrogel Layers. *J. Colloid Interface Sci.* **1994**, *166*, 251–258.

(240) Duracher, D.; Sauzedde, F.; Elaïssari, A.; Pichot, C.; Nabzar, L. Cationic Amino-Containing N-Isopropyl-Acrylamide-Styrene Copolymer Particles: 2-Surface and Colloidal Characteristics. *Colloid Polym. Sci.* **1998**, *276*, 920–929.

(241) Nabzar, L.; Duracher, D.; Elaı, A.; Chauveteau, G.; Pichot, C. Electrokinetic Properties

and Colloidal Stability of N-Isopropylacrylamide-Styrene Copolymer Particles Bearing Different Shell Structures. *Langmuir* **1998**, *14*, 5062–5069.

(242) Dingenouts, N.; Norhausen, C.; Ballauff, M. Observation of the Volume Transition in Thermosensitive Core-Shell Latex Particles by Small-Angle X-Ray Scattering. *Macromolecules* **1998**, *31*, 8912–8917.

(243) Crassous, J. J.; Ballauff, M.; Drechsler, M.; Schmidt, U.; Talmon, Y. Imaging the Volume Transition in Thermosensitive Core-Shell Particles by Cryo-Transmission Electron Microscopy. *Langmuir* **2006**, *22*, 2403–2406.

(244) Tsuji, S.; Kawaguchi, H. Self-Assembly of Poly (N-Isopropylacrylamide)-Carrying Microspheres into Two-Dimensional Colloidal Arrays. *Langmuir* **2005**, *21*, 2434–2437.

(245) Contreras-Cáceres, R.; Sánchez-Iglesias, A.; Karg, M.; Pastoriza-Santos, I.; Pérez-Juste, J.; Pacifico, J.; Hellweg, T.; Fernández-Barbero, A.; Liz-Marzán, L. M. Encapsulation and Growth of Gold Nanoparticles in Thermoresponsive Microgels. *Adv. Mater.* **2008**, *20*, 1666–1670.

(246) Karg, M.; Wellert, S.; Prevost, S.; Schweins, R.; Dewhurst, C.; Liz-Marzán, L. M.; Hellweg, T. Well Defined Hybrid PNIPAM Core-Shell Microgels: Size Variation of the Silica Nanoparticle Core. *Colloid Polym. Sci.* **2011**, *289*, 699–709.

(247) Tirado, M. M.; Martínez, C. L.; de la Torre, J. G. Comparison of Theories for the Translational and Rotational Diffusion Coefficients of Rod-like Macromolecules. Application to Short DNA Fragments Comparison of Theories for the Translational and Rotational Diffusion Coefficients of Rod-like Macromolecules. *J. Chem. Phys.* **1984**, *81*, 2047–2052.

(248) Degiorgio, V.; Piazza, R.; Corti, M.; Stavanst, J. Dynamic Light Scattering Study of Concentrated Dispersions of Anisotropic Spherical Colloids. *J. Chem. Soc., Faraday Trans.* **1991**, *87*, 431–434.

(249) Hoffmann, M.; Lu, Y.; Schrinner, M.; Ballauff, M. Dumbbell-Shaped Polyelectrolyte Brushes Studied by Depolarized Dynamic Light Scattering. *J. Phys. Chem. B* **2008**, *112*, 14843–14850.

(250) Berne, B.; Pecora, R. *Dynamic Light Scattering*; John Wiley, New York, 1985.

(251) Perrin, F. Soïde Immergé (2). *J. Phys. Radium* **1936**, *7*, 1–11.

(252) Zhao, Q.; Fellinger, T. P.; Antonietti, M.; Yuan, J. Y. A Novel Polymeric Precursor for Micro/mesoporous Nitrogen-Doped Carbons. *J. Mater. Chem. A* **2013**, *1*, 5113–5120.

(253) Zhang, L. H.; Sun, Q.; Liu, D. H.; Lu, A. H. Magnetic Hollow Carbon Nanospheres for Removal of Chromium Ions. *J. Mater. Chem. A* **2013**, *1*, 9477–9483.

(254) Wang, H.; Sun, Y.; Yi, J.; Fu, J.; Di, J.; del Carmen Alonso, A.; Zhou, S. Fluorescent Porous Carbon Nanocapsules for Two-Photon Imaging, NIR/pH Dual-Responsive Drug Carrier, and Photothermal Therapy. *Biomaterials* **2015**, *53*, 117–126.

(255) Liu, J.; Wickramaratne, N. P.; Qiao, S. Z.; Jaroniec, M. Molecular-Based Design and Emerging Applications of Nanoporous Carbon Spheres. *Nat. Mater.* **2015**, *14*, 763–774.

(256) Zhao, Q.; Fellinger, T. P.; Antonietti, M.; Yuan, J. Y. Nitrogen-Doped Carbon Capsules via Poly (Ionic Liquid)-Based Layer-by-Layer Assembly. *Macromol. Rapid Commun.* **2012**, *33*, 1149–1153.

(257) Liu, R.; Mahurin, S. M.; Li, C.; Unocic, R. R.; Idrobo, J. C.; Gao, H.; Pennycook, S. J.; Dai, S. Dopamine as a Carbon Source: The Controlled Synthesis of Hollow Carbon Spheres and Yolk-Structured Carbon Nanocomposites. *Angew. Chem. Int. Ed.* **2011**, *50*, 6799–6802.

(258) Zhu, Y.; Zhu, Y.; Murali, S.; Stoller, M. D.; Ganesh, K. J.; Cai, W.; Ferreira, P. J.; Pirkle, A.; Wallace, R. M.; Cychosz, K. A.; *et al.* Carbon-Based Supercapacitors Produced by Activation of Graphene. *Science* **2011**, *332*, 1537–1541.

(259) Deng, Y.; Cai, Y.; Sun, Z.; Gu, D.; Wei, J.; Li, W.; Guo, X.; Jianping, Y.; Zhao, D. Controlled Synthesis and Functionalization of Ordered Large-Pore Mesoporous Carbons. *Adv. Funct. Mater.* **2010**, *20*, 3658–3665.

(260) Gu, D.; Bongard, H.; Deng, Y.; Feng, D.; Wu, Z.; Zhao, D.; Fang, Y.; Mao, J.; Tu, B.; Schüth, F.; *et al.* An Aqueous Emulsion Route to Synthesize Mesoporous Carbon Vesicles and Their Nanocomposites. *Adv. Mater.* **2010**, *22*, 833–837.

(261) Florent, M.; Xue, C.; Zhao, D.; Goldfarb, D. Formation Mechanism of Cubic Mesoporous Carbon Monolith Synthesized by Evaporation-Induced Self-Assembly. *Chem. Mater.* **2012**, *24*, 383–392.

(262) Wen, Z.; Wang, Q.; Zhang, Q.; Li, J. Hollow Carbon Spheres with Wide Size Distribution as Anode Catalyst Support for Direct Methanol Fuel Cells. *Electrochem. commun.* **2007**, *9*, 1867–1872.

(263) Sun, X.; Li, Y. Hollow Carbonaceous Capsules from Glucose Solution. *Colloid Interface Sci.* **2005**, *291*, 7–12.

(264) Titirici, M.; Thomas, A.; Antonietti, M. Replication and Coating of Silica Templates by Hydrothermal Carbonization. *Adv. Funct. Mater.* **2007**, *17*, 1010–1018.

(265) Tang, J.; Liu, J.; Salunkhe, R. R.; Wang, T.; Yamauchi, Y. Nitrogen-Doped Hollow Carbon Spheres with Large Mesoporous Shells Engineered from Diblock. *Chem. Commun.* **2016**, *52*, 505–508.

(266) Strubel, P.; Thieme, S.; Biemelt, T.; Helmer, A.; Oschatz, M.; Brückner, J.; Althues, H.; Kaskel, S. ZnO Hard Templating for Synthesis of Hierarchical Porous Carbons with Tailored Porosity and High Performance in Lithium-Sulfur Battery. *Adv. Funct. Mater.* **2015**, *25*, 287–297.

(267) Balgis, R.; Ogi, T.; Arif, A. F.; Anilkumar, G. M.; Mori, T.; Okuyama, K. Morphology Control of Hierarchical Porous Carbon Particles from Phenolic Resin and Polystyrene Latex Template via Aerosol Process. *Carbon* **2015**, *84*, 281–289.

(268) Cao, J.; Mei, S.; Jia, H.; Ott, A.; Ballauff, M.; Lu, Y. In Situ Synthesis of Catalytic Active Au Nanoparticles onto Gibbsite-Polydopamine Core-Shell Nanoplates. *Langmuir* **2015**, *31*, 9483–9491.

(269) Lu, A. H.; Sun, T.; Li, W. C.; Sun, Q.; Han, F.; Liu, D. H.; Guo, Y. Synthesis of Discrete and Dispersible Hollow Carbon Nanospheres with High Uniformity by Using Confined Nanospace Pyrolysis. *Angew. Chem.* **2011**, *123*, 11969–11972.

(270) Soll, S.; Fellinger, T. P.; Wang, X.; Zhao, Q.; Antonietti, M.; Yuan, J. Water Dispersible, Highly Graphitic and Nitrogen-Doped Carbon Nanobubbles. *Small* **2013**, *9*, 4135–4141.

(271) Ai, K.; Liu, Y.; Ruan, C.; Lu, L.; Lu, G. Sp^2 C-Dominant N-Doped Carbon Sub-Micrometer Spheres with a Tunable Size: A Versatile Platform for Highly Efficient Oxygen-Reduction Catalysts. *Adv. Mater.* **2013**, *25*, 998–1003.

(272) Liang, J.; Du, X.; Gibson, C.; Du, X. W.; Qiao, S. Z. N-Doped Graphene Natively Grown on Hierarchical Ordered Porous Carbon for Enhanced Oxygen Reduction. *Adv. Mater.* **2013**, *25*, 6226–6231.

(273) Ferrari, A. C. Raman Spectroscopy of Graphene and Graphite: Disorder, Electron-Phonon Coupling, Doping and Nonadiabatic Effects. *Solid State Commun.* **2007**, *143*, 47–57.

(274) Zheng, W.; Fan, H.; Wang, L.; Jin, Z. Oxidative Self-Polymerization of Dopamine in an Acidic Environment. *Langmuir* **2015**, *31*, 11671–11677.

(275) Yu, X.; Fan, H.; Liu, Y.; Shi, Z.; Jin, Z. Characterization of Carbonized Polydopamine Nanoparticles Suggests Ordered Supramolecular Structure of Polydopamine. *Langmuir* **2014**, *30*, 5497–5505.

(276) Xu, F.; Tang, Z.; Huang, S.; Chen, L.; Liang, Y.; Mai, W.; Zhong, H.; Fu, R.; Wu, D. Facile Synthesis of Ultrahigh-Surface-Area Hollow Carbon Nanospheres for Enhanced Adsorption and Energy Storage. *Nat. Commun.* **2015**, *6*, 7221.

(277) Abbas, Q.; Pajak, D.; Frackowiak, E.; Béguin, F. Effect of Binder on the Performance of Carbon/carbon Symmetric Capacitors in Salt Aqueous Electrolyte. *Electrochim. Acta* **2014**, *140*, 132–138.

(278) Maleki, H. Thermal Stability Studies of Li-Ion Cells and Components. *J. Electrochem. Soc.* **1999**, *146*, 3224–3229.

(279) Du Pasquier, A.; Disma, F.; Bowmer, T.; Goszds, A. S.; Amatucci, G.; Tarascon, J.-M. Differential Scanning Calorimetry Study of the Reactivity of Carbon Anodes in Plastic Li-Ion Batteries. *J. Electrochem. Soc.* **1998**, *145*, 472–477.

(280) Yuan, J.; Prescher, S.; Sakaushi, K.; Antonietti, M. Novel Polyvinylimidazolium Nanoparticles as High-Performance Binders for Lithium-Ion Batteries. *J. Mater. Chem. A* **2015**, *3*, 7229–7234.

(281) Sun, X.; Zhang, X.; Zhang, H.; Zhang, D.; Ma, Y. A Comparative Study of Activated Carbon-Based Symmetric Supercapacitors in Li_2SO_4 and KOH Aqueous Electrolytes. *J.*

Solid State Electrochem. **2012**, *16*, 2597–2603.

(282) Calvo, E. G.; Lufrano, F.; Staiti, P.; Brigandì, A.; Arenillas, A.; Menéndez, J. A. Optimizing the Electrochemical Performance of Aqueous Symmetric Supercapacitors Based on an Activated Carbon Xerogel. *J. Power Sources* **2013**, *241*, 776–782.

(283) Demarconnay, L.; Raymundo-Piñero, E.; Béguin, F. A Symmetric Carbon/carbon Supercapacitor Operating at 1.6 V by Using a Neutral Aqueous Solution. *Electrochem. commun.* **2010**, *12*, 1275–1278.

(284) Bichat, M. P.; Raymundo-Piñero, E.; Béguin, F. High Voltage Supercapacitor Built with Seaweed Carbons in Neutral Aqueous Electrolyte. *Carbon* **2010**, *48*, 4351–4361.

(285) Shivakumara, S.; Kishore, B.; Penki, T. R.; Munichandraiah, N. Symmetric Supercapacitor Based on Partially Exfoliated and Reduced Graphite Oxide in Neutral Aqueous Electrolyte. *Solid State Commun.* **2014**, *199*, 26–32.

(286) Wang, Y.; Cao, J.; Zhou, Y.; Ouyang, J.-H.; Jia, D.; Guo, L. Ball-Milled Graphite as an Electrode Material for High Voltage Supercapacitor in Neutral Aqueous Electrolyte. *J. Electrochem. Soc.* **2012**, *159*, A579–A583.

(287) Jana, N. R.; Gearheart, L.; Murphy, C. J. Seeding Growth for Size Control of 5 - 40 Nm Diameter Gold Nanoparticles. *Langmuir* **2001**, *17*, 6782–6786.

(288) Jafta, C. J.; Nkosi, F.; Roux, L. le; Mathe, M. K.; Kebede, M.; Makgopa, K.; Song, Y.; Tong, D.; Oyama, M.; Manyala, N.; *et al.* Manganese Oxide/graphene Oxide Composites for High-Energy Aqueous Asymmetric Electrochemical Capacitors. *Electrochim. Acta* **2013**, *110*, 228–233.

(289) Gorgoi, M.; Svensson, S.; Schäfers, F.; Öhrwall, G.; Mertin, M.; Bressler, P.; Karis, O.; Siegbahn, H.; Sandell, A.; Rensmo, H.; *et al.* The High Kinetic Energy Photoelectron Spectroscopy Facility at BESSY Progress and First Results. *Nucl. Instruments Methods Phys. Res. Sect. A* **2009**, *601*, 48–53.

(290) Schaefers, F.; Mertin, M.; Gorgoi, M. KMC-1: A High Resolution and High Flux Soft X-Ray Beamline at BESSY. *Rev. Sci. Instrum.* **2007**, *78*, 123102.

(291) Moulder, J. F.; Stickle, W. F.; Sobol, P. E. Handbook of X-Ray Photoelectron Spectroscopy, 1992nd Ed. In *Perkin-Elmer, Physical Electronics Division*; 1992.

(292) Russel, W. B.; Saville, D. A.; Schowalter, W. R. *Colloidal Dispersions*; 1992.

List of Figures

Figure 1.1.1 Various kinds of nanomaterials. (A) 0D spheres and clusters. (B) 1D nanofibers, wires, and rods. (C) 2D films, plates, and networks. (D) 3D nanomaterials. Reprinted with permission from ref.[10] Copyright 2011 *Nano Reviews*..... 1

Figure 1.1.2 (a) Structure of gibbsite (γ-$Al(OH)_3$). (b) TEM micrograph of gibbsite particles. (c, d) Iridescent columnar phase grown in a gravitational field. Sample that has been standing for 2 and 4 years, respectively. (e) Iridescent columnar phase grown at 900 g using a centrifuge. Reprinted with permission from ref.[24,34] Copyright 1997 and 2007 *American Chemical Society*. 3

Figure 1.2.1 (a) Chemical structure of the dopamine molecule. (b) A schematic illustration of thin film deposition of PDA by dip-coating an object in an alkaline dopamine solution. (c) Thickness evolution of PDA coating on Si as measured by AFM of patterned surfaces. Reprinted with permission from ref.[57] Copyright 2007 *Science*. 5

Figure 1.2.2 (a and b) TEM images of PDA derived hollow carbon nanopheres. Reprinted with permission from ref.[59,73] Copyright 2011 *WILEY-VCH* and Copyright 2011 *American Chemical Society.* TEM images of PDA derived (c) core-shell carbon nanowires and (d) hollow carbon nanotubes, Reprinted with permission from ref.[62,64] Copyright 2011 *Royal Society of Chemistry*. TEM images of PDA derived (e) carbon nanosheets and (f) carbon nanoplates. Reprinted with permission from ref.[74,75] Copyright 2013 and 2015 *WILEY-VCH*. 7

Figure 1.2.3 TEM images of spherical core-shell PNIPAm particles with (a) Au, (b) Au@SiO_2, (c) SiO_2, and (d) PS cores. Reprinted with permission from ref.[87,88] Copyright 2011 *ELSEVIER* and Copyright 2011 *WILEY-VCH*. 8

Figure 1.2.4 TEM images of (a) dumbbell-shaped core-shell PNIPAm particles. Reprinted with permission from ref.[89] Copyright 2011 *WILEY-VCH*. TEM images of ellipsoidal core-shell PNIPAm particles with (b) hematite, (c) maghemite, and (d) PS cores. Reprinted with permission from ref.[90–92] Copyright 2010 and 2012 *Royal society of Chemistry*. 9

Figure 3.1.1 Schematic drawing of a hexagonally shaped gibbsite platelet. The platelet has a surface area *A* and thickness *L*. As a measure for the diameter *D* of the platelet, the diameter of

an equivalent circle is calculated as $D = 2A/\pi$.[95] 13

Figure 3.1.2 Schematic representations of various (liquid crystal) phases for plate-like particles. While each of these phases exhibits long-range orientational order, they differ by the positional correlations between the particles. In the nematic phase long-range positional order is absent. The columnar phase has a two-dimensional lattice of columns, which are constituted of liquid-like stacks of particles..... 14

Figure 3.1.3 Phase diagram of the gibbsite suspensions. The relative volume of the nematic and columnar phase are depicted after phase separation as a function of the platelet volume fraction ϕ. Results apply to σ_D = 17% (triangles) and σ_D = 25% (circles), respectively. The dotted lines indicate the boundaries of the coexistence regions of the suspension with σ_D = 17%. Results from computer simulation for monodisperse hard disks, extrapolate to the current aspect ratio $\langle D \rangle / \langle L \rangle$ of roughly 13, are included for comparison. Reprinted with permission from ref.[102] Copyright 2000 *Nature*..... 15

Figure 3.2.1 "Eumelanin" model of the formation mechanism of PDA. Reprinted with permission from ref.[119] Copyright 2011 *American Chemical Society*..... 18

Figure 3.2.2 Proposed formation mechanism of PDA. In this model, PDA is proposed to be comprised of intra- and interchain noncovalent interactions including hydrogen bonding, π-stacking, and charge transfer. Reprinted with permission from ref.[127] Copyright 2012 *American Chemical Society*. 19

Figure 3.2.3 In-situ deposition of metal nanoparticles on PDA layer. 20

Figure 3.3.1 (a) Absorption spectrum of Nip by sodium borohydride. The main peak of nitrophenolate ions at 400 nm is decreasing with reaction time (blue arrow), while a second peak at 300 nm of Amp is slowly increasing. The two isosbestic points at 280 and 314 nm can be observed. (b) Typical time dependence of the absorption of 4-nitrophenolate ions at 400 nm. The blue portion of the line displays the linear section, from which k_{app} is taken. The induction period t_0 is marked with the black arrow. Reprinted with permission from ref.[145] Copyright 2010 *American Chemical Society*. 21

Figure 3.3.2 Proposed mechanism for the reduction of Nip by metallic nanoparticles: in Step A, Nip is first reduced to the 4-nitrosophenol, which is converted to the stable intermediate Hx

quickly. Hx is then reduced to the final product Amp in Step B, which is the rate-determining step. All reactions take place at the surface of the particles. There is an adsorption/desorption equilibrium for all compounds in all steps. Reprinted with permission from ref.[154] Copyright 2015 *Royal Society of Chemistry*. 22

Figure 3.4.1 Models of the electrical double layer at a positively charged surface: (a) the Helmholtz model, (b) the Gouy–Chapman model, and (c) the Stern model, showing the electrical double-layer formed at a positively charged electrode in an aqueous electrolyte. The electrical potential, Φ, decreases when transitioning from the electrode, Φ_e, to the bulk electrolyte infinite away from the electrode surface, Φ_s. The Stern plane marks the distance of closest approach of the ions to the charged surface. Note the absence of charges/ions in the Stern layer. The diffuse layer starts in the range of 10 – 100 nm from the electrode surface. Reprinted with permission from ref.[164] Copyright 2014 *Wiley-VCH*. 24

Figure 3.4.2 (a) charged and discharged states of a symmetric electrical double layer capacitor. Reprinted with permission from ref.[166] Copyright 2013 *Elservier*. 25

Scheme 1 Synthesis of gibbsite-polydopamine-Au core-shell nanoplates. 29

Figure 4.1.1 (a) TEM image of the colloidal gibbsite platelets. (b) Scatter diagram of the equivalent circular diameter (ECD) of the platelet surface as determined from transmission micrographs with average size of 198 ± 25 nm. 30

Figure 4.1.2 (a) XRD patterns of the gibbsite platelets. (b) TGA (black) and DTA (blue) curve of the gibbsite platelets. 31

Figure 4.1.3 TEM images of the G-PDA core-shell particles prepared under different reaction times: 3 h (a, b), 6 h (c, d), 9 h (e, f), respectively. 32

Figure 4.1.4 TEM images of G-PDA core-shell particles synthesized without constant sonification. 33

Figure 4.1.5 (a) G-PDA core-shell nanoplates dispersed in water, (b) Centrifugation (3 h, 300 g) of the G-PDA particles leads to the formation of columnar phases in water as is observed from iridescence. 34

Figure 4.2.1 TEM images of the G-PDA-Au composite particles prepared with different

concentration of $HAuCl_4$, and its corresponding size distribution curve of Au nanoparticles deposited on G-PDA. (a, b, c) 0.25 mM, (d, e, f) 0.1 mM, and (g, h, i) 0.05 mM after ultrasonification for 8 min. 36

Figure 4.2.2 TEM images of the as-prepared G-PDA-Au nanoparticles under different ultrasonification times, and its corresponding size distribution curve of Au nanoparticles deposited on G-PDA. (a, b and c) 4 min, (d, e and f) 0.5 min in 0.1 mM $HAuCl_4$ solution. ... 38

Figure 4.2.3 XRD patterns of the gibbsite and the G-PDA-Au nanoparticles. 39

Figure 4.3.1 Typical time dependence of the absorption of 4-nitrophenolate ions at 400 nm. Inset: UV-Vis absorption spectra of Nip during the catalytic reaction using G-PDA-Au-1 particles as catalyst. 40

Figure 4.3.2 (a) The dependence of $\ln(C_t/C_0)$ on the reaction time for the reactions catalyzed by 0.013 m^2/L, 0.022 m^2/L, 0.031 m^2/L, and 0.040 m^2/L G-PDA-Au-1 particles, respectively. (b) Rate constant k_{app} as a function of surface area S of Au nanoparticles on G-PDA-Au-1 particles normalized to the unit volume of the system. 41

Figure 4.3.3 Rate constant k_{app} as a function of surface area S of Au nanoparticles on G-PDA-Au nanocomposites normalized to the unit volume of the system. 43

Figure 4.3.4 (a) TEM image of G-PDA-Au-4 nanocomposites under ultrasonification for 4 min in 0.1 mM $HAuCl_4$ aqueous solution and (b) its particle size distribution curves of Au nanoparticles on the G-PDA particles. 44

Figure 4.3.5 (a) UV-Vis absorption spectra of RhB during the reduction catalyzed by G-PDA-Au-1 nanocomposites at room temperature. (b) Typical time dependence of the absorption of RhB at 554 nm. 45

Figure 4.3.6 Rate constant k_{app} as a function of the surface area S of Au nanoparticles on G-PDA-Au-1 normalized to the unit volume of the system. 45

Figure 4.3.7 (a) The TEM image of CTAB-stabilized Au nanoparticles and its size distribution curve. (b) Rate constant k_{app} as a function of the surface area S of CTAB-stabilized Au nanoparticles normalized to the unit volume of the system. 46

Figure 4.3.8 SEM images of the G-PDA-Au particles monolayers on silicon substrate (a)

before and (b) after catalysis. 47

Figure 4.3.9 Conversion efficiency for the reduction of RhB using G-PDA-Au composite particles as catalyst in 90 min reaction in 5 consecutive reaction cycles. 48

Figure 5.1.1 Schematic presentation of the synthesis and functionalization of silica coated gibbsite platelets. 50

Figure 5.1.2 (a) TEM image of GS nanoparticles synthesized by using 4% v/v ammonia. Numerous silica particles are nucleated in the solution. (b) TEM image of the standing GS nanoparticles. The blue arrows point to the silica layer (~16 nm). 51

Figure 5.1.3 (a) TEM image of GS nanoparticles synthesized by using 7% v/v ammonia. (b) TEM image of the standing GS nanoparticles. The white arrow points to two aggregated gibbsite platelets covered and joined with silica. The blue arrows point to the silica layer (~25 nm). 52

Figure 5.1.4 (a) TEM image of gibbsite particles coated with silica. No secondary silica particles or aggregates are produced by using 5.5% v/v of ammonia. The red arrows point to the standing particles. (b) Scatter diagram of the equivalent circular diameter (ECD) of the GS particle as determined from transmission micrographs, average size is 245 ± 46 nm. 53

Figure 5.1.5 EDX spectrum of GS nanoparticles. Cu signal derives from the Cu foil substrate. 53

Figure 5.1.6 (a) TEM image of MPS modified GS particles. No aggregates can be found after MPS modification. (b) TEM image of a single GS-MPS particle at higher magnification. The white arrows point to the silica layer (~25 nm). 54

Figure 5.1.7 FT-IR spectra of GS and GS-MPS particles. 54

Figure 5.2.1 Schematic presentation of the synthesis of thermo-responsive hybrid microgels. 55

Figure 5.2.2 TEM images of the GS-MPS-PNIPAm trilayer microgels synthesized with different NIPAm monomer concentrations (a, b) 0.077 M, (c, d) 0.062 M, and (e, f) 0.049 M, during polymerization. 57

Figure 5.2.3 Hydrodynamic radius of the GS-MPS-PNIPAm particles as a function of temperature. GS-MPS-PNIPAm-1, GS-MPS-PNIPAm-2, and GS-MPS-PNIPAm-3 are the hybrid microgel particles prepared with different NIPAm monomer concentrations (black square) 0.077 M, (red circle) 0.062 M, and (blue triangle) 0.049 M, respectively. And hydrodynamic radius of the GS-MPS core particles (green star) as a function of temperature. 58

Figure 5.2.4 SEM images of the GS-MPS-PNIPAm trilayer microgels dried on a silicon substrate..... 58

Figure 5.2.5 (a) Cryo-TEM micrographs of the thermosensitive GS-MPS-PNIPAm core-shell particles synthesized with 0.062 M NIPAm monomer in aqueous solution at room temperature. The samples were maintained at 20 ºC. (b) The dark core consists of GS-MPS, and the corona of PNIPAm cross-linked with BIS is indicated by dash line..... 59

Figure 5.2.6 a) AFM height image of the GS-MPS-PNIPAm microgels synthesized with 0.062 M NIPAm monomer. b) the corresponding cross-section profile taken along the black line in a. 60

Figure 5.2.7 (a) The correlation functions of the GS-MPS-PNIPAm microgels that are measured at the scattering angle of 20° (blue solid line) and 30° (red dashed line) under the temperature of 50 °C. (b) The relaxation rate Γ is plotted as a function of the square of the scattering vector (q^2). The solid lines are linear fits to the data. 61

Figure 6.1.1 Synthesis of polydopamine coated nanoplates. 67

Figure 6.1.2 (a) TEM image of the silica-coated gibbsite particles. (b) TEM image of an enlarged part of a silica-coated gibbsite particle. The blue arrows point to the silica layer (~8 nm thick). (c) Scatter diagram of the equivalent circular diameter (ECD) of the silica-coated gibbsite particles as determined from transmission micrographs, average size 215 ± 27 nm. (d) EDX pattern of the silica-coated gibbsite particles. Cu signal derives from the Cu foil substrate..... 68

Figure 6.1.3 (a) TEM image of the hollow silica nanoplates after acid etching. (b) TEM image of an enlarged part of a hollow silica nanoplate. The particle is clearly empty inside. (c) Scatter diagram of ECD of the hollow silica nanoplates as determined from transmission

micrographs, average size 213 ± 24 nm. (d) EDX pattern of the hollow silica nanoplates. Cu signal derives from the Cu foil substrate. 69

Figure 6.1.4 (a) TEM image of the HSP@PDA core-shell nanoparticles. (b) TEM image of an enlarged part of a HSP@PDA core-shell nanoparticle. (c) Scatter diagram of ECD of the hollow silica nanoplates as determined from transmission micrographs, average size 232 ± 27 nm. (d) Zeta potential of the obtained hollow silica nanoplates (HSP) and HSP@PDA core-shell nanoparticles in aqueous solution at different pH values. 70

Figure 6.2.1 Synthetic route to water dispersible hollow carbon nanoplates by confined carbonization of HSP@PDA core-shell nanoparticles in a silica matrix. 72

Figure 6.2.2 (a) TEM images of the HSP@PDA nanoparticles/silica hybrids before carbonization. The dashed white lines point to the isolated HSP@PDA nanoparticles in silica gel. (b) TEM image of the HSP@PDA nanoparticles/silica hybrids. The red arrow points to the hollow core. The blue arrow points to the silica layer. The black arrow points to the PDA layer. (c) SEM image of the hollow carbon nanoplates. (d) EDX spectrum of the hollow carbon nanoplates. 73

Figure 6.2.3 (a) TEM image of the hollow carbon nanoplates. (b) Scatter diagram of ECD of the hollow carbon nanoplates as determined from transmission micrographs, average size 231 ± 20 nm (c) TEM image of an enlarged part of a hollow carbon nanoplate. The blue arrows point to the carbon layer (~9 nm thick). (d) TEM image of a standing hollow carbon nanoplate. The blue and black arrows point to the carbon layer and hollow core, respectively. 74

Figure 6.2.4 (a) Photographs of the hollow carbon nanoplates dispersed in aqueous dispersion at different pH conditions. (b) Nitrogen adsorption and desorption isotherm of the hollow carbon nanoplates. Inset: BJH pore-size distribution curve of the hollow carbon nanoplates, which was determined from the desorption branch of the isothermal. A centre peak at 3.8 nm (pore diameter) can be clearly observed. (c) TGA analysis of the hollow carbon nanoplates. 75

Figure 6.2.5 (a) HAXPES survey spectrum of the hollow carbon nanoplates. (b) HAXPES spectrum of the N 1s core level of the hollow carbon nanoplates. (c) XRD pattern of the hollow carbon nanoplates. (d) Raman spectrum of the hollow carbon nanoplates. The weak peak at ~1100 cm^{-1} derives from the glass substrate. 76

Figure 6.2.6 (a, b) HR-TEM images show the enlarged graphite-like domain in the hollow

carbon nanoplates, which contains over 10 stacking layers. (c, d) HR-TEM images of the magnified part in (a and b). The interlayer distance is 0.35 nm. 78

Figure 6.3.1 (a) CV curves for hollow carbon nanoplates based symmetric supercapacitors by using PIL as binder (50 mV/s, 1mol/L Li_2SO_4), and (b) CV curves at scan rates of 10−300 mV/s. 80

Figure 6.3.2 (a) Galvanostatic charge/discharge curves at current densities of 0.5−5 A/g of hollow carbon nanoplates based symmetric supercapacitors by using PIL as binder, and (b) the relationships between the specific capacitance and different current densities of hollow carbon nanoplates based symmetric supercapacitors. 81

Figure 6.3.3 (a) Ragone plot of gravimetric energy density versus power density for the HCPs based symmetric supercapacitor by using PIL as binder. The green area indicates the Ragone plot for supercapacitors. (b) The cyclic performance of hollow carbon nanoplates based symmetric supercapacitors by using PIL as binder in the voltage window between 0 to 1.4 V at a current density of 2.5 A/g. 81

Figure 6.3.4 (a) Cyclic voltammetry curves for hollow carbon nanoplates based symmetric supercapacitors using PVDF as binder (50 mV/s, 1mol/L Li_2SO_4) and (b) CV curves at scan rates of 10−300 mV/s. 82

Figure 6.3.5 (a) Galvanostatic charge/discharge curves at current densities of 0.5−5 A/g of PVDF based electrodes, and (b) the relationships between the specific capacitance and different current densities of hollow carbon nanoplates based supercapacitors using PVDF as binder. 83

Figure 6.3.6 The cyclic performance of hollow carbon nanoplates based symmetric supercapacitor using PVDF as binder in the voltage window between 0 to 1.4 V at a current density of 2.5 A/g. 84

Figure 8.3.1 Schematic figure of the ALV-4000 compact goniometer system. Laser light passes an automated attenuator and a vertical polarizer. The light scatters at the colloidal dispersion and passes a horizontal analyzer (only in DDLS) to be detected at an avalanche photo diode (APD). The intensity fluctuations are measured over different scattering vectors by changing the scattering angle θ with a goniometer. 98

Figure 8.3.2 Exemplary fits of the relaxation rate versus q^2 to determine D^T and D^R from a DLS (blue open triangle) and DDLS (black open square for slow mode and red open circle for fast mode) experiment. 99

List of Tables

Table 4.2.1 Au nanoparticles with various sizes synthesized under different reaction conditions. 38

Table 4.3.1 Catalytic activity of the different reported catalyst systems based on Au nanoparticles for the reduction reaction of Nip. 42

Table 4.3.2 Catalytic activity of G-PDA-Au nanocomposites prepared under different reaction conditions for the reduction reaction of Nip. 43

Table 5.2.1 Translational diffusion coefficients D^T measured from both DLS and DDLS experiments and rotational coefficients D^R measured from DDLS experiments of the GS-MPS-PNIPAm microgels at 50 °C. 62

Table 6.2.1 Elemental composition information of the hollow carbon nanoplates. 77

Table 6.3.1 Comparison of our symmetric supercapacitors data with reported carbon-based symmetric supercapacitors using neutral electrolytes. 85

Table 8.2.1 Specified recipe for the synthesis of G-PDA-Au nanocomposites. 91

Table 8.2.2 Specified recipe for the synthesis of GS-MPS-PNIPAm composite particles..... 93

List of Publications

1. **Cao, J.**; Mei, S. L.; Jia, H.; Ott, A.; Ballauff, M.; Lu, Y. In Situ Synthesis of Catalytic Active Au Nanoparticles onto Gibbsite–Polydopamine Core-Shell Nanoplates. *Langmuir* **2015**, *31*(34), 9483–9491.

2. Mei, S. L.; **Cao, J.**; Lu, Y. Controllable Assembly of Two Types of Metal Nanoparticles onto Block Copolymer Nanospheres with Ordered Spatial Distribution. *J. Mater. Chem. A* **2015**, *3*(7), 3382–3389.

3. **Cao, J.**; Jafta, C. J.; Gong, J.; Ran, Q. D.; Lin, X. Z.; Félix, R.; Wilks, R. G.; Bär, M.; Yuan, J. Y.; Ballauff, M.; Lu, Y. Synthesis of Dispersible Mesoporous Nitrogen-Doped Hollow Carbon Nanoplates with Uniform Hexagonal Morphologies for Supercapacitors. *ACS Appl. Mater. Interfaces* **2016**, DOI: 10.1021/acsami.6b08946.

4. **Cao, J.**; Günther, A.; Kochovski, Z.; Gu, S. S.; Ran, Q. D.; Ballauff, M.; Lu, Y. Thermo-Responsive Core-Shell Hybrid Microgels Based on Anisotropic Plate-like Nanoparticles. (*In preparation*) **2016**.

Presentations at Conferences and Meetings

15th Conference of the International Association of Colloid and Interface Scientists, 24-29.05.2015, Mainz, Germany, oral presentation: Formation of Au nanoparticles in the presence of gibbsite-polydopamine core-shell nanoplates.

Abbreviations

Symbols

$\boldsymbol{\phi}$ volume fraction

$\boldsymbol{\sigma}$ standard deviation

$\boldsymbol{\lambda}$ wavelength

$\boldsymbol{T}$ temperature

$\boldsymbol{R_h}$ hydrodynamic radius

$\boldsymbol{\theta}$ scattering angle

$\boldsymbol{\Gamma}$ decay rate

$\boldsymbol{D^T}$ translational diffusion coefficient

$\boldsymbol{D^R}$ rotational diffusion coefficient

$\boldsymbol{q^2}$ scattering vector

$\boldsymbol{S}$ surface area of nanoparticles

$\boldsymbol{t_0}$ induction period

$\boldsymbol{k_{app}}$ apparent rate constant

$\boldsymbol{k_1}$ surface normalized rate constant

$\boldsymbol{K_{Nip}}$ Langmuir adsorption constant of 4-nitrophenol

$\boldsymbol{K_{Hx}}$ Langmuir adsorption constant of 4-hydroxylaminophenol

$\boldsymbol{K_{BH4}}$ Langmuir adsorption constant of sodium borohydride

$\boldsymbol{n}$ Langmuir–Freundlich exponent.

ε_r dielectric constant of the electrolyte solvent

ε_0 dielectric constant of vacuum

d effective thickness of the electrical double layer

Φ electrical potential

C_{DL} total capacitance of the electrode

C_H capacitance from Helmholtz layer

C_D capacitance from the diffuse layer

I current density

Δt discharge time

M total mass of active materials

V the operating voltage

C_{sp} specific capacitance

E specific energy density

P specific power density

R_s equivalent series resistance

τ ion diffusion time constant

D ion transport coefficient

L ion diffusion length

Chemicals

AIBN azobisisobutyronitrile

AIP aluminum isopropoxide

Amp 4-aminophenol

APTES (3-aminopropyl)trimethoxysilane

ASB aluminum sec-butoxide

BIS N, N'-methylenebis (acrylamide)

CTAB hexadecyltrimethylammonium bromide

Dopamine 3-hydroxytyramine hydrochloride

Fe_3O_4 iron oxide

$HAuCl_4 \cdot 4H_2O$ hydrogen tetrachloroaurate hydrate

HCl hydrochloric acid

H_2SO_4 sulfuric acid

Hx 4-hydroxylaminophenol

KCl potassium chloride

KPS potassium persulfate

Li_2SO_4 lithium sulfate monohydrate

MPS 3-(trimethoxysilyl)propyl methacrylate

$NaBH_4$ sodium borohydride

Na_2SO_4 sodium sulfate

NH_4HF_2 ammonium hydrogen difluoride

NH_4OH ammonium hydroxide

$Ni(OH)_2$ nickel hydroxide

Nip 4-nitrophenol

NIPAm N-isopropylacrylamide

NMP 1-methyl-2-pyrrolidinone

PAA-Na poly(acrylic acid sodium salt)

PBMA poly(n-butyl methacrylate)

PDA polydopamine

PIL poly (ionic liquid)

PMMA poly(methyl methacrylate)

PNIPAm poly(*N*-isopropylacrylamide)

PS polystyrene

PVDF poly(vinylidene fluoride)

PVP polyvinylpyrrolidone

RhB Rhodamine B

SiO_2 silica

TEOS tetraethyl orthosilicate

TiO_2 titanium dioxide

Tris tris(hydroxymethyl) aminomethane

ZnO zinc oxide

Other abbrevations

AFM atomic force microscopy

Ag silver

Au gold

BET the Brunauer-Emmett-Teller equation

BJH the Barrett-Joyner-Halenda method

CV cyclic voltammetry

Cryo-TEM cryogenic temperature transmission electron microscopy

DDLS depolarized dynamic light scattering

DLS dynamic light scattering

ECD equivalent circular diameter

EDX energy-dispersive X-ray spectroscopy

EDLC electrical double layer capacitors

ESR equivalent series resistance

FTIR Fourier transform infrared spectroscopy

GS silica coated gibbsite

HAXPES Hard x-ray photoelectron spectroscopy

HCPs hollow carbon nanoplates

HMCNs hollow mesoporous carbon nanospheres

HSP hollow silica nanoplates

iep isoelectric point

LCST lower critical solution temperature

NMR nuclear magnetic resonance

Pd palladium

Pt platinum

RAFT radical addition fragmentation chain transfer

SEM scanning electron microscopy

Si silicon

TEM transmission electron microscopy

TGA thermogravimetric analysis

UV-Vis ultraviolet to visible

XRD X-ray diffraction

Acknowledgement

At this point I want to express my gratitude to all the people in and out of the institute, who helped me to complete this work.

Firstly, I would like to express my sincere gratitude to my supervisor Prof. Dr. Matthias Ballauff for the opportunity to work in his group, for the fascinating topic, for advice, motivation, immense knowledge and scientific guidance.

Furthermore, I would like to thank Prof. Dr. Yan Lu for the help and discussions whether in questions about the synthesis of the nanoparticles or UV-measurements especially at the beginning of this work. Her kind guidance helped me in all the time of my researches and writing of papers and this thesis. I could not have imagined having a better supervisor for my Ph.D. study.

Special thanks to Dr. Andreas Ott, Sasa Gu and Qidi Ran for the TEM measurements, and Dr. Zdravko Kochovski for the cryo-TEM measurements. I thank He Jia, Fuxian Wang, Dr. Guanchao Yin and Martin Kärgell for the SEM and EDX measurements. Thanks also to Dr. Xianzhong Lin and Yang Liu for the XRD measurements. I am grateful to Dr. Jiang Gong, Weiyi Zhang and Dr. Jiayin Yuan from Max Planck Institute of Colloids and Interfaces for the Raman, FTIR and elemental analysis measurements. Moreover, I would like to thank Dr. Roberto Félix, Dr. Regan G. Wilks and Prof. Dr. Marcus Bär for the HAXPES characterizations and data analysis.

For the DLS and DDLS measurements, I appreciate all the useful guidance and help from Dr. Fangfang Chu and Dr. Annegret Günther. Especially to Dr. Annegret Günther, who offered helpful introductions and patiently taught me how to conduct the measurements and analyze the data. Also, I would like to thank Dr. Rafael Roa Chamorro and Prof. Dr. Joachim Dzubiella for the cooperation with all the theoretical simulations and useful discussions.

For the electrochemical part, I would like to thank Dr. Yan Yang and Dr. Charl J. Jafta for teaching me the majority of the experimental techniques necessary for my research on supercapacitors. Especially to Dr. Charl J. Jafta, who gave me the kind introduction to the electrochemical instruments and software, as well as taught me how to assemble the coin cells and to do the performance measurements of the supercapacitors.

In the following, I would like to thank all the former and current colleagues, Dr. Frank Polzer, Dr. Stefanie Wunder, Dr. Fangfang Chu, Dr. Weihua Wang, Dr. Charl J. Jafta, Dr. Yan Yang, Dr. Andreas Ott, He Jia, Shilin Mei, Sasa Gu, Qidi Ran, Shun Yu and Martin Kärgell. They were always there in the time of need and never gave second thought to lend help whenever required. They are great friends, and I believe that it is the camaraderie between us that has made the Lu's group successful and strong.

I greatly appreciate the financial support from China Scholarship Council (CSC) during the past three and a half years.

Last, but by no means the least, I would like to thank my family: my parents and to my sister and my girlfriend Dr. Fang Ren for supporting me spiritually during the Ph.D. period and my life in general. Without them I would forget myself and lose my own. I will keep going!

Selbstständigkeitserklärung

Hiermit erkläre ich die vorliegende Arbeit selbst verfasst und nur unter Zuhilfenahme der angegebenen Hilfsmittel angefertigt zu haben.

Ferner erkläre ich, dass ich nicht anderweitig mit oder ohne Erfolg versucht habe, eine Dissertation einzureichen oder mich einer Doktorprüfung zu unterziehen.

Berlin, den 10.10.2016

Jie CAO